AEROSPACE NUCLEAR SAFETY

RESEARCH REPORT

RE-ENTRY FLIGHT DEMONSTRATION NUMBER ONE (RFD-1): PREFLIGHT DISASSEMBLY ANALYSIS AND OBSERVED DISASSEMBLY OF THE SIMULATED SNAP-10A REACTOR

Department 7410

SC-RR-64-515
TID-4500 (32nd Edition)
AEROSPACE SAFETY

SANDIA CORPORATION

PRIME CONTRACTOR TO THE UNITED STATES ATOMIC ENERGY COMMISSION
ALBUQUERQUE, NEW MEXICO
LIVERMORE, CALIFORNIA

TID-4500 (32nd Edition)
AEROSPACE SAFETY

SC-RR-64-515

RE-ENTRY FLIGHT DEMONSTRATION NUMBER ONE (RFD-1): PREFLIGHT DISASSEMBLY ANALYSIS AND OBSERVED DISASSEMBLY OF THE SIMULATED SNAP-10A REACTOR

Prepared By

R. D. Klett, 7412

T. M. Hysinger, 7412

M. M. Robertson, 1122

Reviewed By

R. D. Klett, 7412

H. E. Hansen, 7411

A. J. Clark, Jr., 7412

A. E. Bentz, 7413

Approved By

V. E. Blake, 7410

Don B. Shuster, 7400

ABSTRACT

This report describes the SNAP-10A Simulated Test Reactor, the test philosophy of Re-entry Flight Demonstration Number One, the analytical analysis of reactor disassembly, and the results of the flight test. The preflight analytical analysis included wind-tunnel tests, computer studies of the trajectory and of stagnation-point heating to determine local heating rates expected during the flight, and a computer analysis of reactor burnup. The computer studies were repeated after the flight test, using the actual atmospheric density and the observed trajectory. The results of the analytical studies are compared with the actual disassembly, as determined by optical, spectrographic, and telemetered data from the flight. Since there was good correlation between the analytical and the flight-test data, the disassembly of a simulated test reactor was predicted, assuming the flight unit had reentered on an orbital-decay trajectory at a zero-degree angle of attack.

September 1964

ACKNOWLEDGMENT

Sandia Corporation Department 7410, Aerospace Nuclear Safety Department, gratefully acknowledges the outstanding support of the following Sandia Corporation organizations, without whose help the RFD-1 flight and the subsequent analyses could not have been performed:

Organization Number	Organization Name	Organization Number	Organization Name
1110	Materials & Process Department I	3300	Medical
1120	Materials & Process Department II	3400	Technical Information & Publications
1320	Electromechanical Development Department I	4200	Development Shops
1330	Electromechanical Development Department II	4300	Purchasing
1420	Electronic Systems Department	4410	Design Definition Department
1430	Electronic Components Department	4500	Plant Engineering & Maintenance
1440	Reliability Department	5410	Nuclear Burst Physics Department
1530	Systems Engineering Department	7210	Test Projects Department
1540	Engineering Analysis and Equipment Design Dept.	7220	Test Range Department
2640	Engineering & Research Support Department	7240	Test Support Department
3210	Safety Engineering Department	7250	Nuclear Test Department
3240	Security Standards & Operations Department	7320	Environmental Research & Operations Department
		7330	Planning & Functional Test Department
		7420	Aero- & Thermodynamics Department
		7430	Upper Atmosphere Projects Department
		7620	Programming Department

In addition to the encouragement and support given by the Division of Reactor Development of the AEC, Sandia Corporation gratefully acknowledges the support of Atomics International, the National Aeronautics and Space Administration, the United States Air Force, the United States Coast Guard, and the United States Navy in the performance of the flight program. Other organizations contributing to this program are acknowledged by specific references throughout the text.

Issued by Sandia Corporation,
a prime contractor to the
United States Atomic Energy Commission

Printed in USA. Price $2.50. Available from the Office of Technical Services, Department of Commerce, Washington 25, D. C.

FOREWORD

In the application of nuclear energy to space vehicles, safety features are designed into the power supplies to preclude significant radiation hazards to the earth's population during orbital-decay re-entries, or in the event of aborted missions. Sandia Corporation, a prime nuclear-weapon contractor to the AEC, was authorized by the AEC Division of Reactor Development to act as the prime contractor for the independent safety evaluation of aerospace nuclear power systems. The Aerospace Nuclear Safety Program at Sandia includes research and development studies, ground testing, flight testing, system analysis, and independent safety assessment.

Re-entry Flight Demonstration Number One (RFD-1) was the first re-entry flight test to be conducted under this program since its inception in March 1962. The SNAP-10A reactor (Systems for Nuclear Auxiliary Power), designed and constructed by Atomics International (AI), was selected for RFD-1 because of its proposed early use as a nuclear auxiliary power supply for earth satellites. An inert version of the SNAP-10A was flown on RFD-1 to determine the effectiveness of the safety design. The simulated reactor was mounted on a re-entry vehicle (RV) which was placed into the required trajectory by a four-stage Scout booster launched from the National Aeronautics and Space Administration (NASA) Wallops Station, Wallops Island, Virginia.

Sandia carried out its assignment in the Aerospace Nuclear Safety Program by performing the following tasks:

1. Design of the flight-test experiment and the configuration of the simulated test reactor (STR), in cooperation with AI.
2. Study of the capabilities of the Scout launch vehicle, and recommendation of a trajectory which would assure that the desired information would be obtained.
3. Design of the re-entry vehicle and telemetry (TM) system, and coordination of interface problems with AI, NASA, and Ling-Temco-Vought Corporation.
4. Theoretical predictions of flight-test outcomes.
5. Preparation of documents on support requirements for the Atlantic Missile Range (AMR) and the NASA Wallops and Bermuda stations.
6. Provision of complementary downrange instrumentation for collection of TM and optical data.
7. Management of flight-implementation activities.
8. Data reduction and analysis.
9. Comparison of flight-test results with theoretical calculations.

The following Sandia Corporation reports, together with the present volume, comprise the final documentation of RFD-1:

Report No.	Title
SC-RR-64-501	Re-entry Flight Demonstration Number One (RFD-1): Final Flight-Test Plan
SC-RR-64-502	Re-entry Flight Demonstration Number One (RFD-1): Data Book
SC-RR-64-510	Re-entry Flight Demonstration Number One (RFD-1): Comparison of the Preflight and Observed Trajectories
SC-RR-64-511	Re-entry Flight Demonstration Number One (RFD-1): Design, Development, and Performance of the Re-entry Vehicle
SC-RR-64-516	Re-entry Flight Demonstration Number One (RFD-1): Optical Data and Fuel-Element Experiment
SC-RR-64-517	Re-entry Flight Demonstration Number One (RFD-1): Atmospheric Sciences Support

TABLE OF CONTENTS

LIST OF TABLES

LIST OF TABLES (cont)

LIST OF ILLUSTRATIONS

LIST OF ILLUSTRATIONS (cont)

LIST OF ILLUSTRATIONS (cont)

LIST OF ILLUSTRATIONS (cont)

RE-ENTRY FLIGHT DEMONSTRATION NUMBER ONE (RFD-1):
PREFLIGHT DISASSEMBLY ANALYSIS AND OBSERVED
DISASSEMBLY OF THE SIMULATED SNAP-10A REACTOR

SECTION I -- INTRODUCTION

SNAP-10A (Figure 1) is a 30-kw thermal nuclear reactor which provides the heat source for the thermoelectric energy-conversion system of the SNAP-10A Auxiliary Power Unit (APU). The SNAP-10A APU (Figure 2) delivers 500 watts of electrical power. Heat produced by the reactor is transferred to the converter by a liquid-metal coolant system. The coolant is circulated by a DC conduction pump. The integrated converter-radiator consists of an array of thermoelectric modules mounted on a series of tubes through which the liquid-metal coolant is pumped. Electricity is generated in the converter as a result of the heat flow through the modules; heat flows from the circulating coolant on the hot side to the radiating surfaces on the cold side, and is there expelled to outer space by radiation.

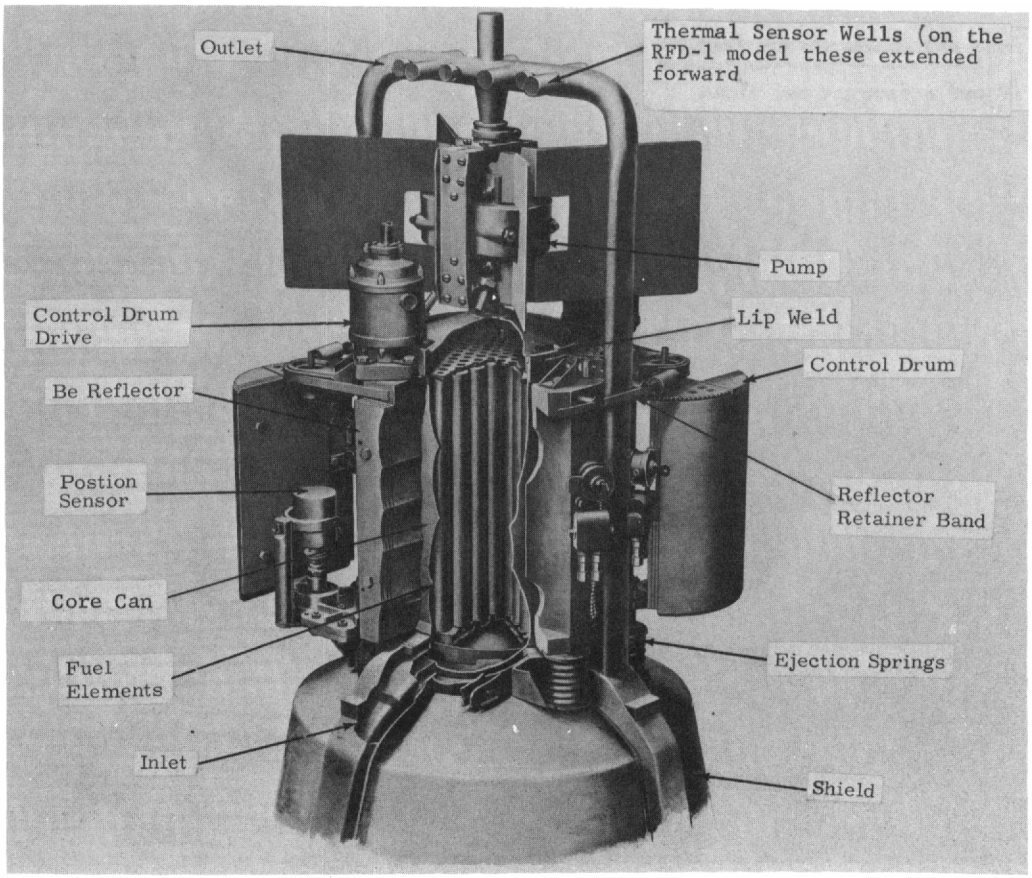

Figure 1. SNAP-10A reactor

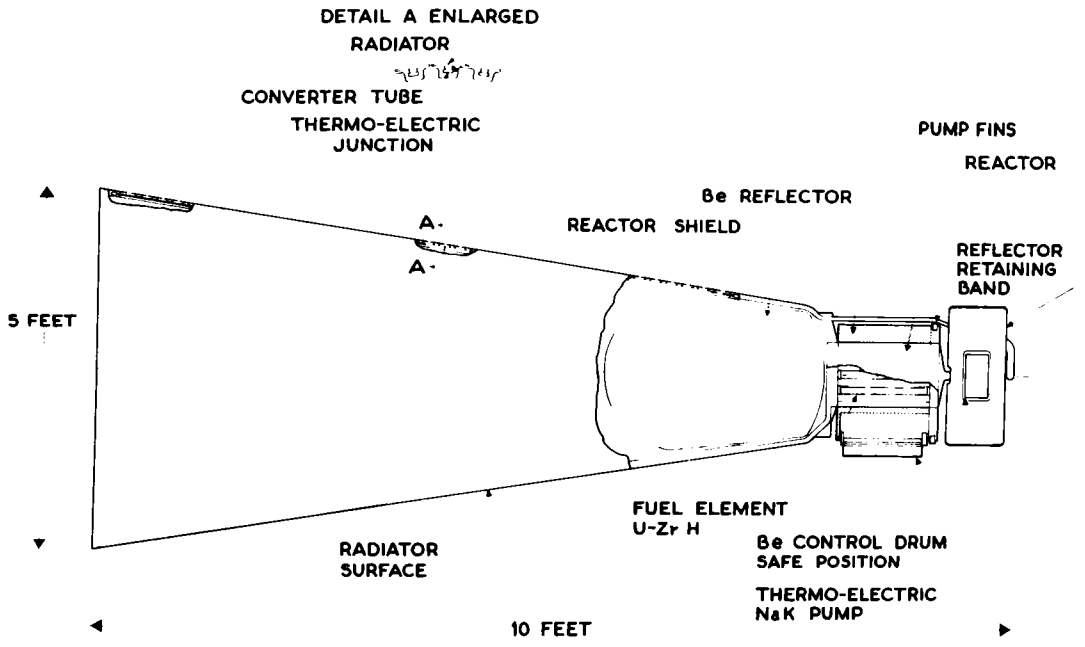

Figure 2. SNAP-10A auxiliary power unit

The APU is designed for one year of continuous operation as an auxiliary power supply for space systems. The reactor is programmed to shut down at the end of one year. After operating at the normal power level for one year, the reactor will have built up an inventory of long-lived fission products within its fuel rods.

If the reactor shut-down mechanism were to fail, the reactor would continue to operate, with its output approaching zero exponentially as the uranium in the fuel rods decays. Thus, if the reactor stayed in orbit long enough, re-entry at the termination of the orbit would pose no radiation hazard from fission products. If only a short-lived orbit were achieved, it would be essential for the core vessel of the reactor to disassemble during re-entry to prevent the reactor from going critical upon impact with the earth. In addition, the fuel rods, containing an inventory of fission products, would have to burn up under re-entry heating, and burn up at a high enough altitude and into small enough particles to allow sufficient decay and dispersion during fallout to prevent any significant hazard (Figure 3). To this end, AI's design philosophy has been to provide a reactor configuration which will allow early disassembly of the core, and subsequent burnup and dispersion of the resulting debris, when the reactor is exposed to the aerodynamic heating experienced during re-entry into the earth's atmosphere from a decaying orbit. To facilitate disassembly, provisions were made for ejection early in re-entry of the exterior reflectors which surround the core vessel. The reflectors are spring-loaded, and are released when brazed lap-joints in a metal retaining band melt under re-entry heating.

In an attempt to approximate the aerodynamic heating which occurs during orbital decay, RFD-1 was flown on a re-entry trajectory from Wallops Island, Virginia, to an impact area about 200 miles southeast of Bermuda. A NASA Scout booster (Figure 4) was used to place the re-entry system (Figure 5) into the required trajectory. The sequence of events during the trajectory is shown in Figure 6.

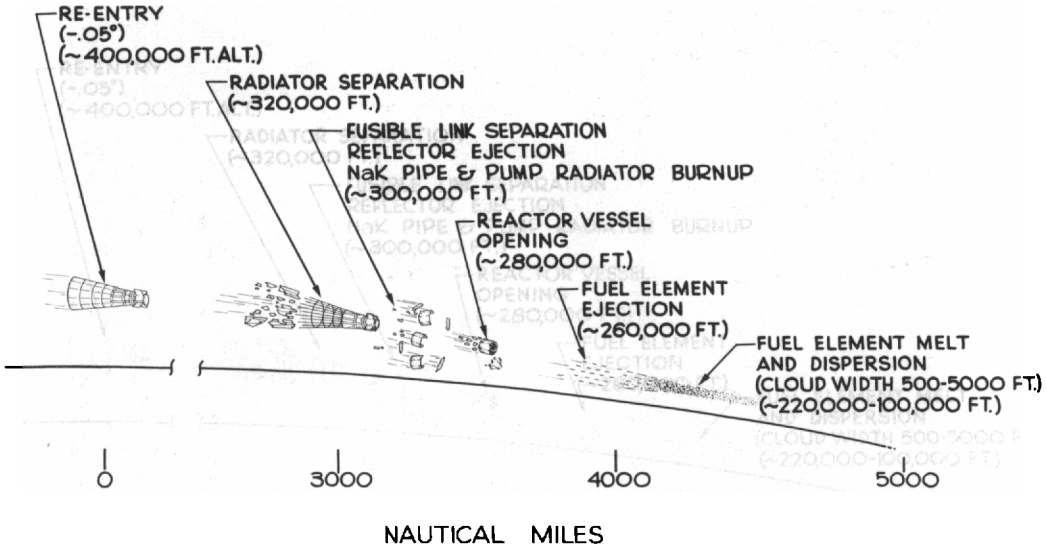

Figure 3. Desired SNAP-10A orbital-decay re-entry sequence

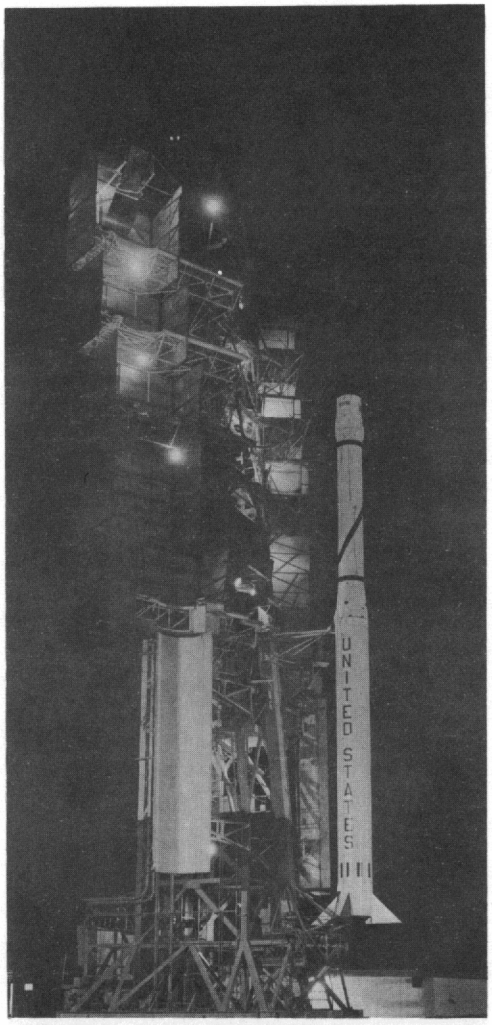

Figure 4.

NASA Scout

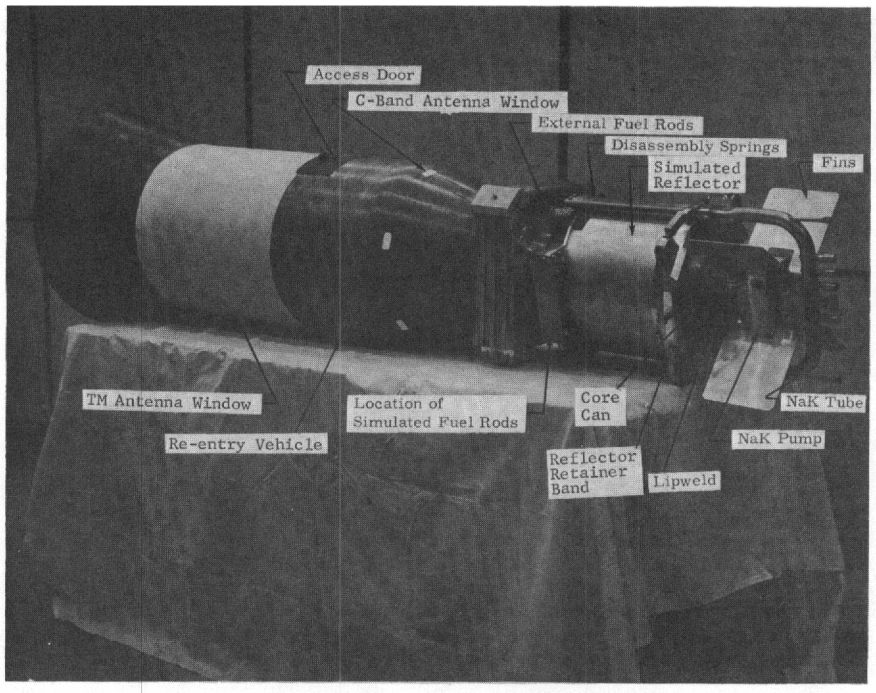

Figure 5. RFD-1 re-entry system

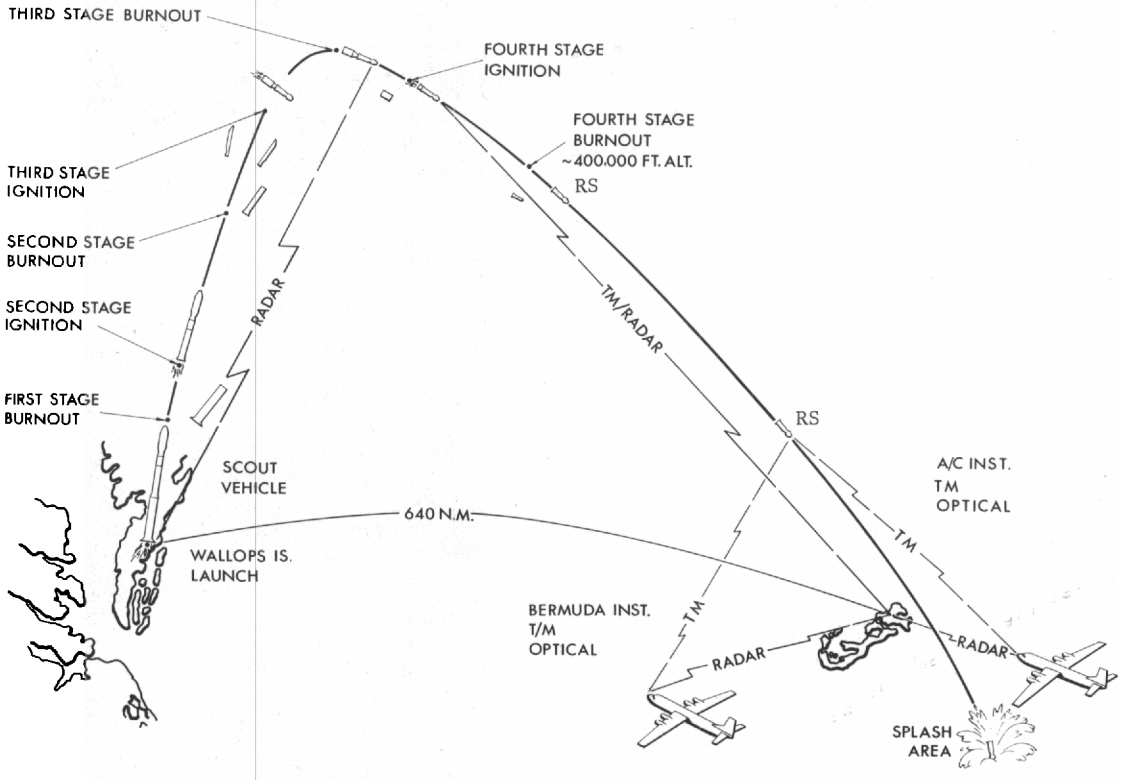

Figure 6. RFD-1 trajectory

At an altitude of 400,000 feet, which was considered the beginning of re-entry, the prescribed RFD-1 parameters were:

Velocity:	20,178 ft/sec
Re-entry angle:	-6°
Ballistic coefficient:	288 lb/ft^2

As may be seen in Figure 7, the stagnation heating for the RFD-1 flight did not duplicate that expected from an orbital-decay re-entry. This was due to launch-vehicle limitations and the need to have RFD-1 re-enter within a given distance of land-based cameras and TM receivers. However, there was enough heating to disassemble the reactor at an altitude above 150,000 feet, permitting the primary objectives of this test to be achieved. These objectives were:

1. To determine the sequence of reactor disassembly during a shallow-angle re-entry. This was accomplished by instrumenting the STR with thermocouples to give the temperature responses of various parts of the reactor, and instrumenting it with switches to reveal the points in the trajectory at which the major parts of the reactor disassembled. This information was transmitted in real time, and data were obtained until TM blackout occurred at 198,000 feet. Supplementary information on reactor disassembly was obtained from telemetered data on changes in pitch and roll of the RV, and from optical coverage.

2. To determine if a computer study, used in conjunction with plasma-jet ablation tests and wind-tunnel tests to define local heating rates, can be used to accurately predict re-entry burnup of a shape as complex as the SNAP-10A reactor. It can be shown by the good correlation between the flight data and the results of this type of study that the current methods of analysis can accurately predict burnup, and this method may be used in lieu of some future flight tests. In addition to offering lower costs and shorter time scales, wind-tunnel and plasma-jet tests can be more heavily instrumented and more closely controlled than flight tests. Unfortunately, ground testing techniques are not sufficiently advanced to allow ground testing to replace all flight testing, but it can be an aid in supplementing flight tests, and possibly in reducing the number of flight tests required. If TM reception is lost before an experiment is completed, as was the case with RFD-1, this analytical approach permits the data obtained to be extrapolated out to destruction temperatures.

3. To determine the amount of stagnation aerodynamic heating corresponding to the failure of each RFD-1 reactor part, thus enabling calculation of the disassembly sequence of a reactor re-entering on an orbital-decay trajectory.

A secondary objective of the flight test was to obtain data on the burnup of full-scale reactor fuel elements. Two groups of simulated fuel rods were incorporated into the re-entry system. One group of 12 full-scale, simulated SNAP-10A fuel rods filled with tracer material was ejected from the re-entry system before appreciable aerodynamic heating had occurred. These rods were ejected early in the trajectory to more closely simulate the total heating they would experience after being released from the core vessel during the higher heating pulse of an orbital-decay re-entry. SC-RR-64-516 gives a comprehensive description of this experiment. A second group of simulated fuel rods (short cylinders of simulated fuel-rod materials) was attached to the base of the reactor. These rods, after being subjected to re-entry heating, were to have been examined upon recovery of the re-entry vehicle to determine ablation rates (see SC-RR-64-511).

The following sections of this report include a description of the simulated test reactor, the preflight and postflight theoretical analyses of reactor disassembly during re-entry, a description of the flight program, and the results of the RFD-1 flight test.

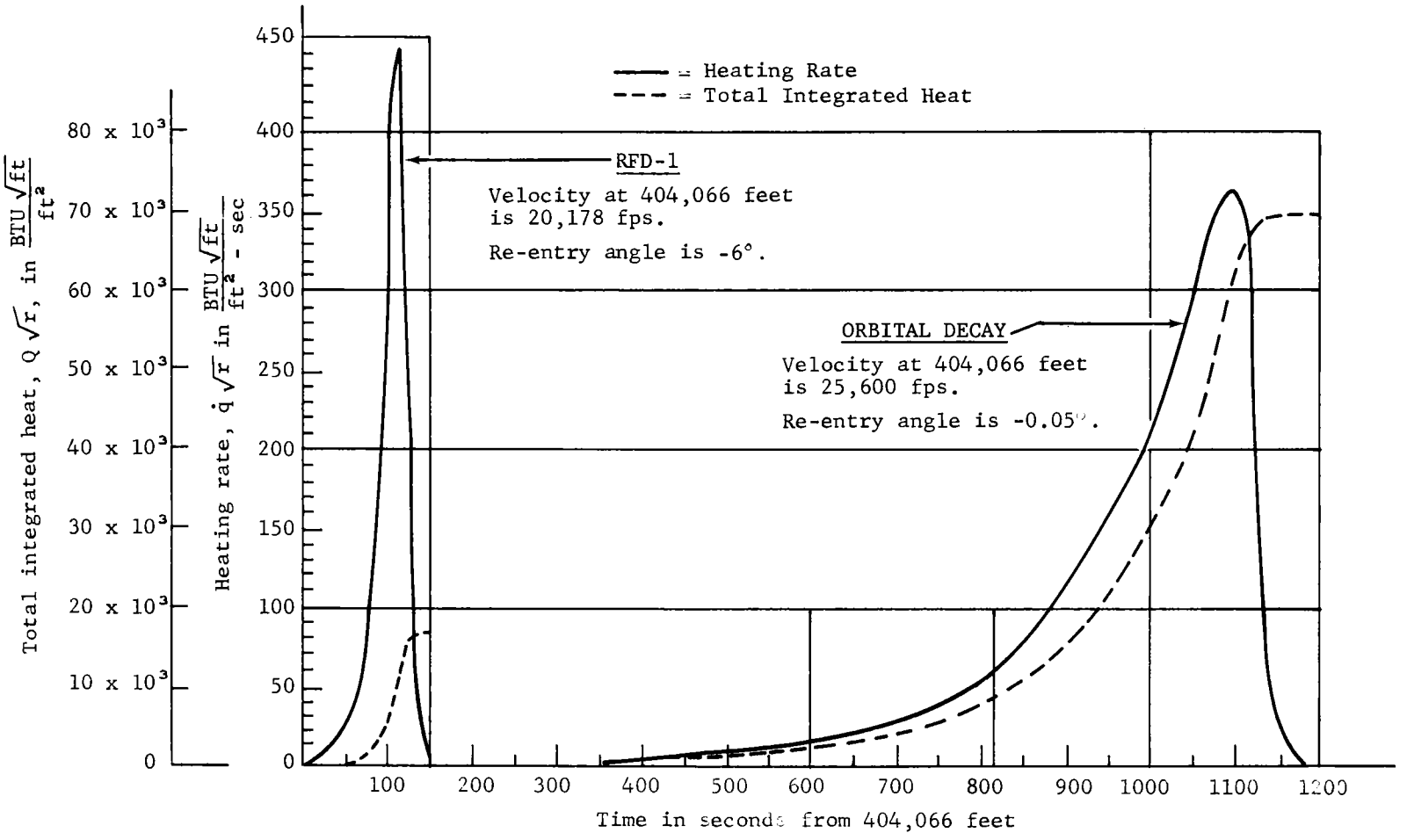

Figure 7. Comparison of heating for predicted RFD-1 re-entry and theoretical orbital-decay re-entry

SECTION II -- DESCRIPTION OF THE SNAP-10A REACTOR

Auxiliary Power Unit

The SNAP-10A APU consists of a reactor and a thermoelectric-converter section. The reactor is controlled by beryllium reflectors. It is started by rotating four segments of the reflector to the inboard position; two of the segments are spring-actuated and two are motor driven. The reactor is shut down by ejecting the exterior reflectors which surround the core vessel.

The core vessel (Figure 8), which is made of 316 stainless steel, is 9 inches in diameter and 16 inches long. It contains 37 moderator-fuel elements of uranium-zirconium hydride clad with Hastelloy N. The fuel rods are held in a hexagonal array by two grid plates, one at either end of the array of rods. The bottom grid plate is permanently fixed to the core vessel, while the top grid plate is spring-loaded to allow for relative thermal expansion in the axial direction. The space between the array of fuel rods and the inner wall of the core vessel is filled with six internal, beryllium reflectors.

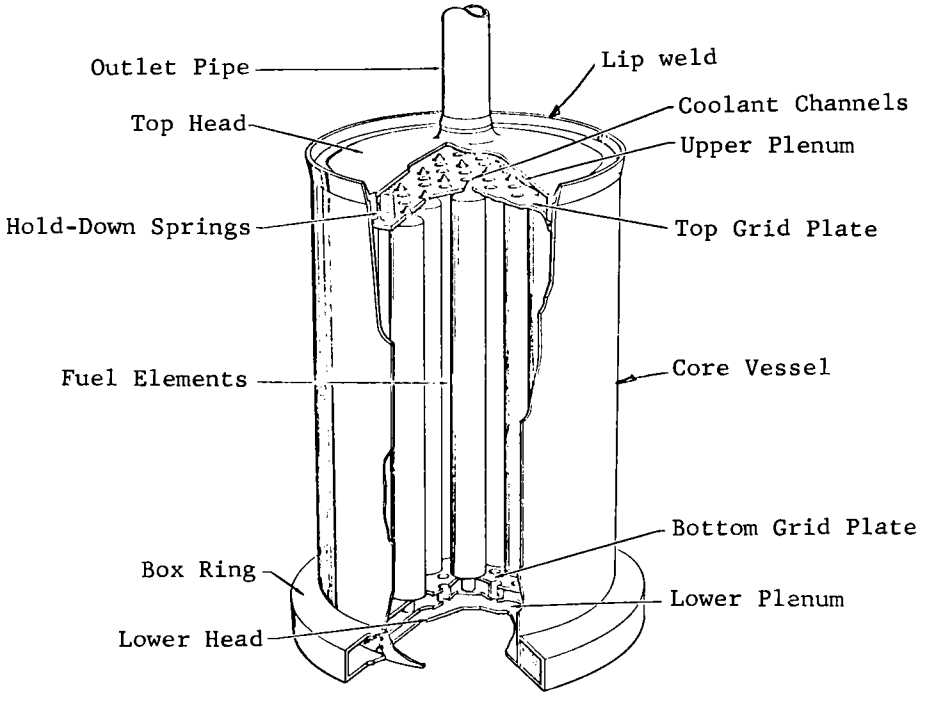

Figure 8. SNAP-10A reactor core

Heat is transferred from the fuel rods to the converter section by a eutectic mixture of sodium and potassium (NaK-78), which is circulated by a thermoelectric DC Faraday conduction pump. The pump derives its power from the Seebeck voltage developed in its own, separate thermoelectric converter, which is mounted as an

integral part of the pump. After leaving the pump, the NaK travels to the upper manifold of the converter through two tubes which run on either side of the core vessel. From the manifold, the NaK coolant is circulated through tubes on the inner surface of the converter section, supplying heat to the hot junction of the thermoelectric elements. The coolant then returns to the lower plenum chamber of the core vessel.

The radiator-converter, which has the form of a truncated cone, incorporates an array of stainless-steel tubes on which the thermoelectric elements are mounted. The skin of the cone is a radiating surface which forms the cold junction and maintains the proper temperature drop across the converter elements by radiating heat to outer space. The radiator is segmented so that each module has an individual radiating surface. A flexible, braided cable provides the electrical connection between modules.

Disassembly and Dispersion Sequence

When the SNAP-10A APU re-enters the earth's atmosphere, disassembly of the reactor, burnup of the fuel rods, and dispersion of the resulting particles depend entirely upon aerodynamic heating and on shear and pressure forces. The reactor was designed to disassemble in the following sequence (assuming that the APU enters pump first):

1. The exterior beryllium reflectors act as good heat sinks, and would delay or prohibit reactor disassembly if they were to remain on the reactor until they melted off. They are therefore ejected early in the re-entry heat pulse. Ejection is accomplished by spring-loading the reflectors away from the core vessel. They are held in place by disconnect hinges at the bottom and by a fusible-link band at the top. Standoffs hold the band out in the airstream and away from the reflectors. When aerodynamic heating raises the temperature of the brazed joints in the band to 1220°F, the joints part, allowing the springs to eject the reflectors.

2. Next to burn off are the aluminum pump fins and the transverse, stainless-steel NaK tube, which partially protect the front of the core vessel from aerodynamic heating.

3. With only the pump remaining to obstruct airflow over the core vessel, the lip-weld area begins to melt and the cover burns through inboard of the relatively massive lip. When the cover burns through, the pump is released. Even with part of the core-vessel cover gone, none of the fuel rods are freed, since the top grid plate is still held in place by the remaining cover rim.

4. After the protuberances from the core vessel have melted off, the core vessel heats up uniformly and more rapidly. Final disassembly of the vessel occurs with the almost simultaneous melting of the core-vessel walls and the lip area.

5. After the core disassembles, each fuel rod re-enters individually and is subjected to re-entry heating from that part of the heat pulse remaining.

Simulated Test Reactor (STR)

A production SNAP-10A could not be used for the RFD-1 test for reasons of safety, weight limitation, and data acquisition. Actual SNAP-10A hardware was used wherever possible in the STR, with deviations from the production unit being determined by joint agreement between AI and Sandia Corporation. Significant differences between the APU and the STR were as follows:

1. The converter section of the APU was not included on the RFD-1 flight vehicle. This section does not affect core disassembly, provided the vehicle is stabilized, and hence was not necessary for this flight. Its additional weight and volume would have precluded the use of the Scout launch vehicle.

2. The NaK pump was simulated with a hollow, stainless-steel box with an exterior shape similar to that of the production pump. At the time the STR was designed, the design of the pump had not been completed, but it was known that it would contain a heavy, iron core. Neither the actual nor the simulated pump would have melted by the time they were freed by the melting of the transverse NaK tube and the core-vessel cover. Since disassembly of the pump would not affect the experiment, the lighter, simulated pump was used.

3. The switches across the front of the transverse NaK tube were not completely designed at the time of STR assembly. Since these switches would not burn off by the time the NaK tube was released, they were replaced by solid, stainless-steel reproductions.

4. The NaK coolant was omitted from the system to reduce weight, to prevent the large NaK flare during re-entry from obscuring the tracer material in the fuel-rod experiment, and to prevent extending the period of RF blackout. NaK has 3.74 times the coefficient of thermal expansion of stainless steel. If the temperature of the reactor is below the melting temperature of NaK prior to re-entry, there will be a gap between the NaK and its containers; thus, when the container heats up during re-entry, only a small fraction of the heat will be transferred to the NaK. When exposed to re-entry heating, the walls will heat up much more rapidly than the NaK, tending to maintain the gap until the NaK melts. If the NaK is liquid at the beginning of re-entry, heat will be transferred from the containers to the coolant by natural convection. During the RFD-1 re-entry, this convection would have been only 2 percent of the total heat input to the cover, 0.5 percent in the lip area, and 6 percent at the core-vessel sides. During an orbital-decay re-entry, the NaK inlet and outlet tubes would burn off early, allowing the NaK to be forced out by aerodynamic pressure. The small amount of heat absorbed by the NaK could easily be accounted for with minimal error in an analytical study of orbital-decay disassembly.

5. The exterior beryllium reflectors and control drums were replaced by an aluminum shell designed to simulate the exterior shape of the beryllium parts and to have the same clearance from the core vessel. This modification was primarily dictated by the payload weight limitations of the Scout launch vehicle. Also, the substitution of aluminum for beryllium eliminated the possibility of any BeO hazard from burnup or ablation of the beryllium parts. The aluminum simulators offered the same thermal protection to the core vessel that the beryllium reflectors would have. Since the same clearance was maintained, the same amount of convective aerodynamic heating to the core vessel took place. The only heat transfer from the reflector to the core vessel is by radiation. An analytical study showed that the maximum temperature that any part of the aluminum simulators would reach before ejection was 590°F. At this temperature, radiation is negligible. The aluminum simulators were provided with production SNAP-10A hinges, ejection springs, band standoffs, fusible-link band, and clearance adjustments.

6. There were no simulated fuel rods in the STR core. The grid plates were held in the proper position by six steel spacer rods to maintain the prescribed spring force on the cover. Theoretical studies showed that very little heat would be lost from the core vessel to the rods, with or without NaK in the vessel. Hence, deleting the rods from the system did not appreciably affect vessel disassembly.

Analytical studies were made, based on heat inputs measured on a full-scale reactor in the Arnold Engineering Development Center (AEDC) 100-inch hot-shot tunnel (Appendix A), and backed up by tests of a reactor core vessel in the Sandia radiant-heat facility, using the measured heat inputs. These studies indicated that the core-vessel cover would melt at approximately a 3.75-inch radius, with the lip area which restrains the top grid plate remaining intact until approximately 150,000 feet altitude for the RFD-1 trajectory. Fuel-rod separation at this low an altitude would not permit fuel-rod burnup or ablation. Furthermore, an analytical study showed that, at 150,000 feet in the RFD-1 trajectory, the aerodynamic force on the front of the core vessel is greater than the combined spring and deceleration forces. Complete burnup of the STR core vessel would therefore be necessary to release the fuel rods. During an orbital-decay trajectory, the core-vessel cover would burn off before aerodynamic forces became high enough to restrain the fuel rods.

Even if a full complement of fuel rods were included to determine if the rods could become wedged in the core vessel, the distortion effects of heating during operation of the reactor would not be duplicated. Since little or no information could be obtained on separation and subsequent burnup of the fuel rods during the RFD-1 flight, it was decided to use the 122 pounds the fuel rods would weigh for other experiments. These experiments included: (a) the fuel rods which were ejected at the beginning of re-entry to more closely simulate the total heating they would see after core-vessel disassembly during an orbital-decay trajectory (see SC-RR-64-516), and (b) the pieces of fuel material permanently attached to the base of the reactor and exposed to aerodynamic heating during the entire re-entry.

7. The six interior beryllium reflectors were omitted from the RFD-1 STR both to reduce weight and to eliminate any BeO hazards. Since there were no fuel rods in the STR core vessel, the presence of the interior reflectors was not necessary to provide lateral restraints on the fuel assembly. Melting of the core vessel would not be enhanced significantly by the removal of the interior reflectors, since very little heat would be transferred from the vessel to these reflectors in the short period of reactor disassembly during re-entry. At most, there would be only line contact between the reflectors and the core-vessel wall. Therefore, all heat transfer from the wall to the reflectors would have to be by radiation or free convection, both of which are negligible. The top grid plate separates the interior reflectors from the vessel cover, acting as a radiation shield and as a deterrent to natural convection.

8. The bottom 2-15/16 inches of the reactor was potted with Sandia Epoxy A, which is a char-forming ablation material. The purpose of this material was to protect the base of the reactor, which held the attached fuel-rod experiment, and to protect the front of the RV.

9. There were other minor modifications necessary for instrumentation mounts and the routing of lead wires, but these did not affect the experiment.

SECTION III -- REACTOR AND RANGE INSTRUMENTATION

Instrumentation of the Simulated Test Reactor

Thermocouples and switches were used to determine the temperature rise of different parts of the STR and to determine the times when different STR components disassembled during the flight of RFD-1. Switch locations are shown in Figure 9. The switches used were high-temperature, positive-action, plunger types. Switches 1 through 6 were used to indicate the time and mode of cover failure. Switches 1, 2, and 3 would open first if the lip or outer periphery of the cover was the first to melt. If the core-vessel walls were to melt before the cover, all six switches would open almost simultaneously. Switches 7 and 8 were to indicate reflector ejection, with Switch 7 to open at first motion and Switch 8 to open when the reflector hinge disconnected.

The 21 thermocouples mounted on the STR gave the temperature profiles of strategic locations on different components. When the component on which a thermocouple was mounted failed, the thermocouple would open or give erratic readings, indicating the time at which a given component melted or came off. Temperature profiles from the thermocouples served three purposes:

1. With the heat-sink properties of the material surrounding each thermocouple known, local heating rates could be determined. By relating these rates to the stagnation heating for the flight of RFD-1, ratios of stagnation heating can be computed for use in analyses of orbital-decay burnup. Comparing these heating ratios with theories for free-molecular and continuum flow will aid in determining the transition conditions.

2. A preflight computer study of burnup of the STR during the RFD-1 flight was made with the aid of plasma-jet ablation tests and wind-tunnel tests to define local heating rates. By comparing the predicted values with the actual temperature rise shown by each thermocouple during the RFD-1 flight, it was possible to determine the validity of analytical analysis.

3. Thermocouple data indicated the failure temperature of each component when exposed to aerodynamic loading.

Thermocouple locations and materials are shown in Figure 10 and Table I. All leads from thermocouples on the STR were routed to the reference junction in the base of the reactor, where they were changed to copper wire. Temperature of the reference junction was monitored with two platinum-resistance thermometers. The epoxy potting compound surrounding the reference junction maintained a nearly constant temperature in the reference junction during the entire reactor burnup.

Other instruments which were located in the RV but provided data essential to the analysis of reactor burnup included pitch, yaw, and roll sensors as well as longitudinal and lateral acceleration transducers. Data from the re-entry system (RS) instrumentation were transmitted by the TM system in the RV and acquired by air-, sea-, and ground-based receivers and recorders.

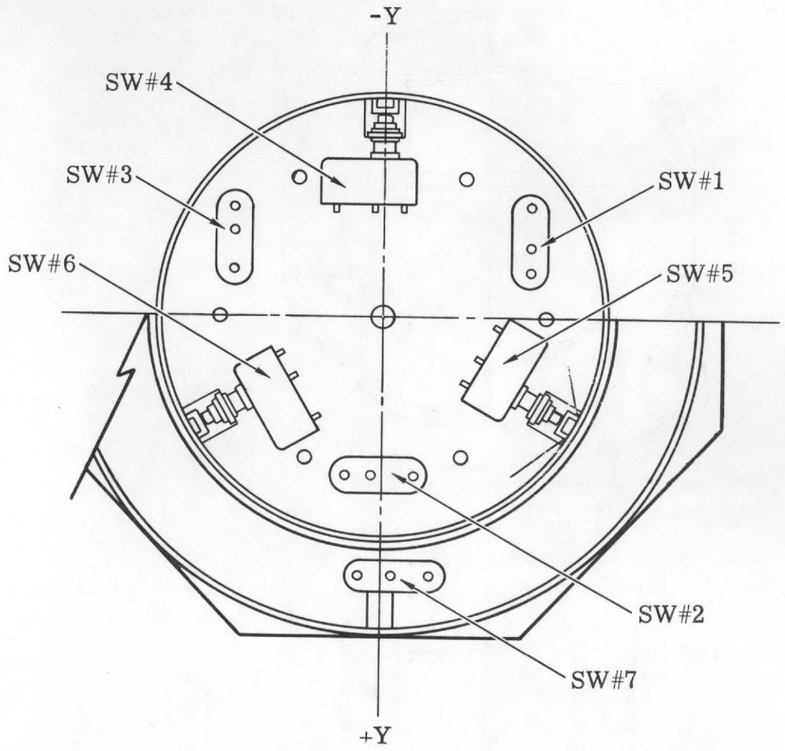

SECTION D-D

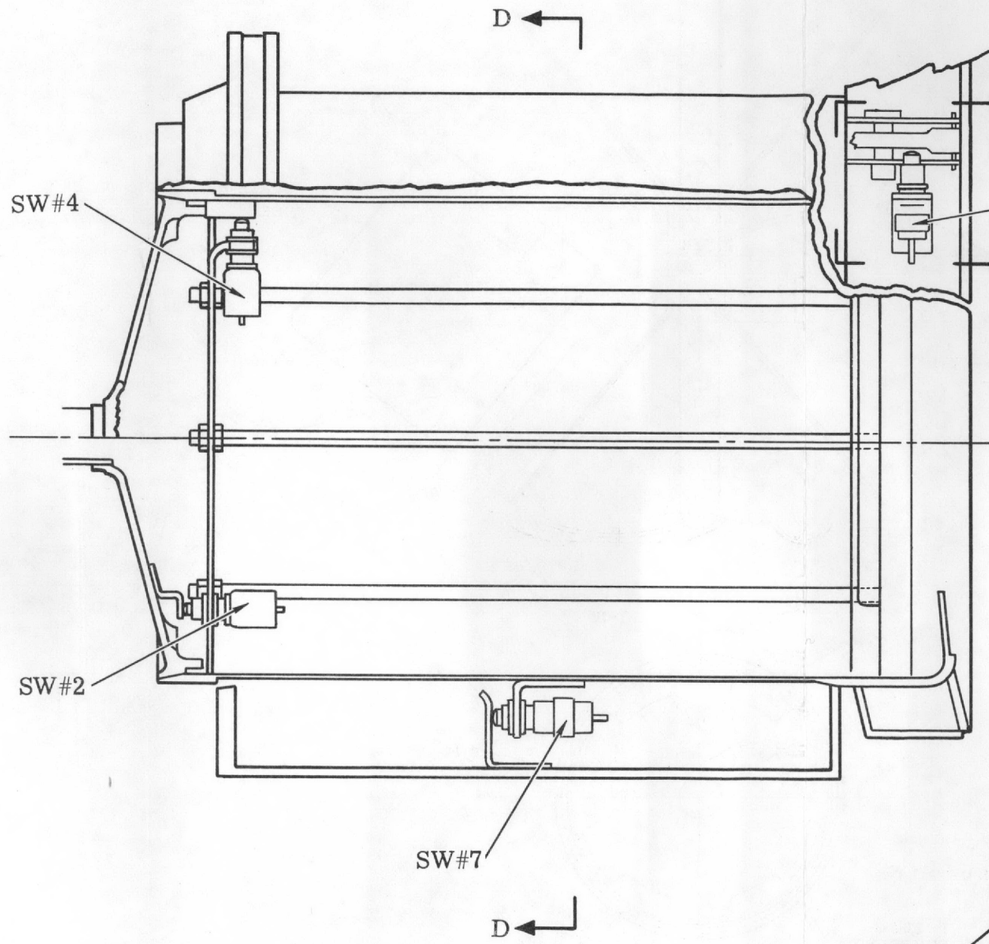

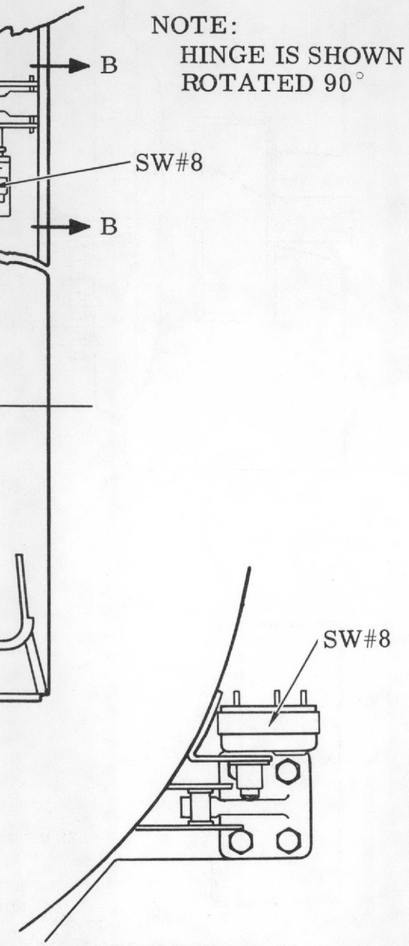

SECTION B-B

NOTE:
HINGE IS SHOWN
ROTATED 90°

Figure 9. Switch locations on the simulated test reactor

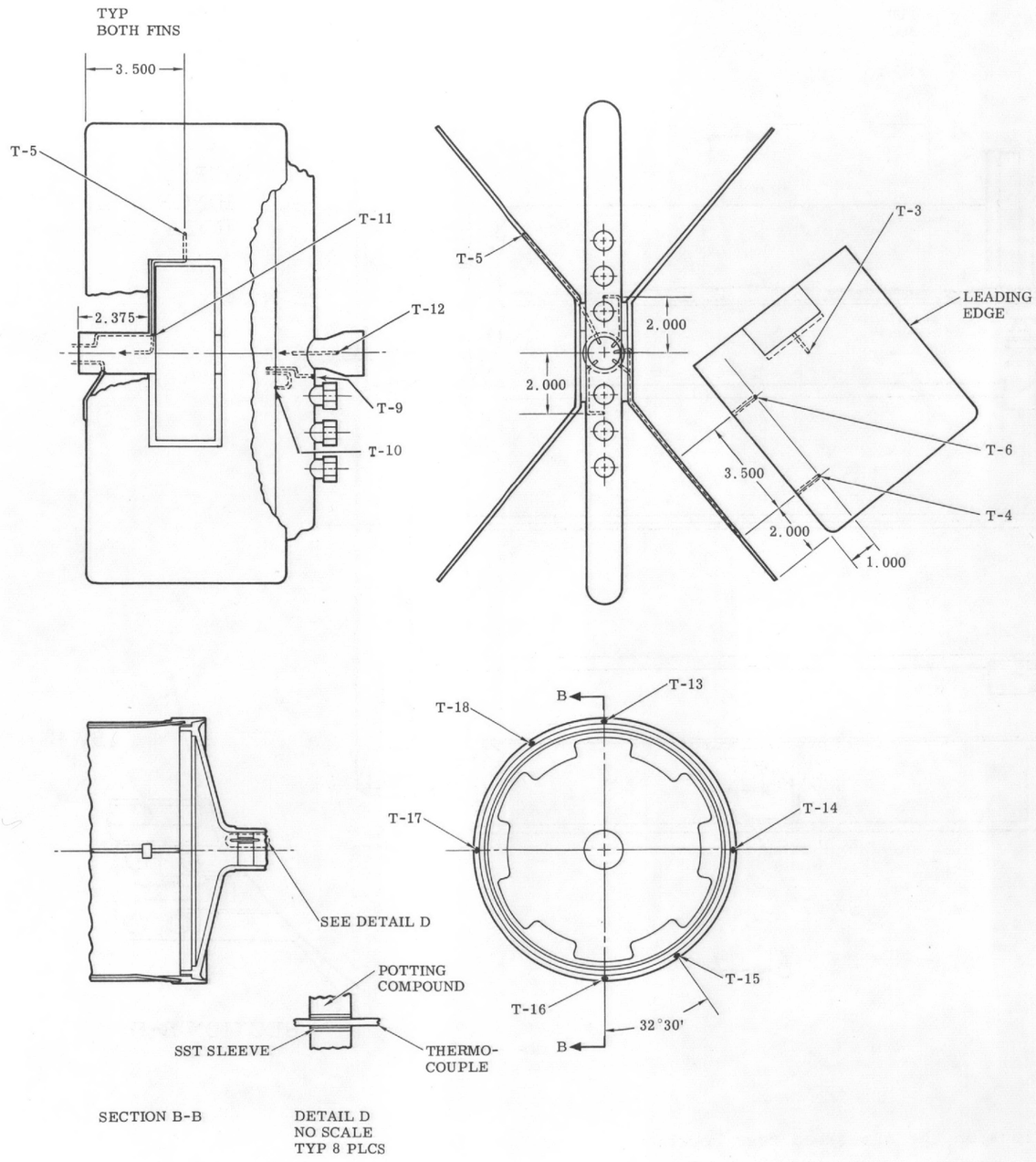

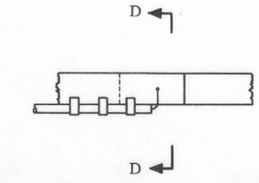

SECTION D-D

DETAIL C
TYPICAL INST. OF
BAND THERMOCOUPLE

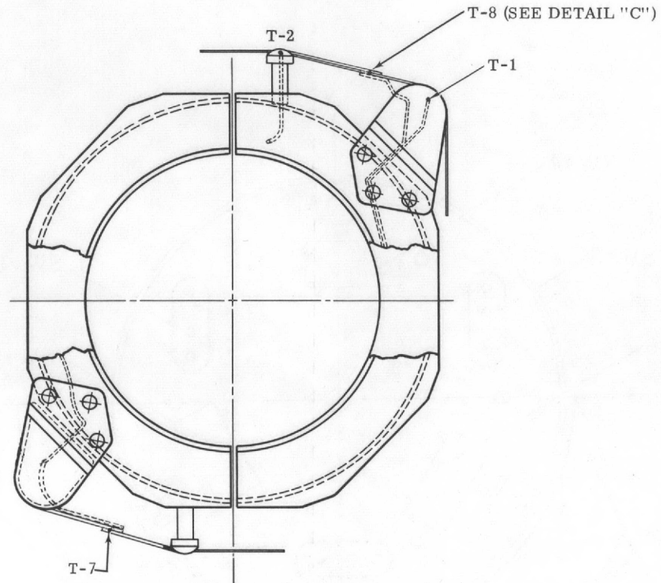

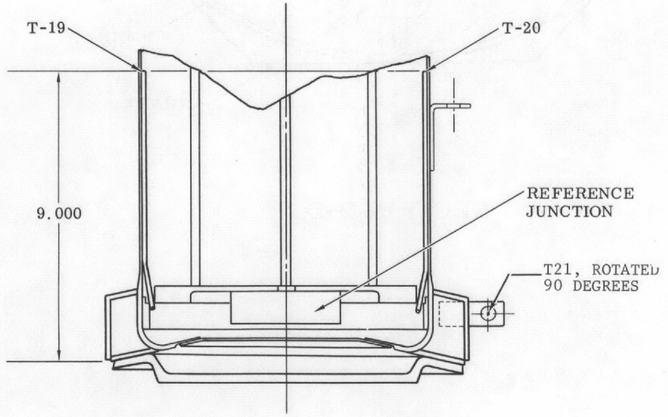

Figure 10. Thermocouple locations on the simulated test reactor

TABLE I

Thermocouple Locations

Thermocouple No.	Material	Location
1	Chromel-Alumel	Bracket, band support
2	Chromel-Alumel	Band standoff
3	Chromel-Alumel	Fin, center
4	Chromel-Alumel	Fin, trailing, outer
5	Chromel-Alumel	Fin, center, opposite T3
6	Chromel-Alumel	Fin, trailing, inner
7	Chromel-Alumel	Band joint
8	Chromel-Alumel	Band joint, opposite T7
9	Pt/Pt/13% Rh	Transverse NaK tube, leading surface
10	Pt/Pt-13% Rh	Transverse NaK tube, trailing surface
11	Pt/Pt-13% Rh	Base of NaK pump
12	Pt/Pt-13% Rh	NaK fill tube
13	Pt/Pt-13% Rh	Lip weld behind NaK tube
14	Pt/Pt-13% Rh	Lip weld in unobstructed flow
15	Pt/Pt-13% Rh	Lip weld behind fin
16	Pt/Pt-13% Rh	Lip weld behind NaK tube, opposite T13
17	Pt/Pt-13% Rh	Lip weld in unobstructed flow, opposite T14
18	Pt/Pt-13% Rh	Lip weld behind fin, opposite T15
19	Pt/Pt-13% Rh	Core-vessel wall
20	Pt/Pt-13% Rh	Core-vessel wall, opposite T19
21	Chromel-Alumel	Sandia heat meter, base of reactor

Telemetry

The RFD-1 TM consisted of an FM/FM system with 10 watts of RF power at 240.2 mc, supplied to a hollow, cylindrical, dipole antenna mounted to the inner surface of the cylindrical section of the RV. Eight subcarrier frequencies were used for real-time transmission of data, and three subcarriers carried information delayed 100 seconds by a tape recorder-playback system. The 100-second delay channels were to be used to relay data acquired during RF blackout. The TM system was designed to provide information concerning the condition of the reactor and the RV shell, the orientation of the RS, as well as vibration and acceleration. Sampling rates for the instruments were as follows:

Pitch, yaw, and roll sensors	Continuous
Accelerometers	10 samples/second
Switches	5 samples/second
Thermocouples	1 sample/second

Details of the electrical design and the construction of the TM system are given in SC-RR-64-501.

Range Instrumentation

Range support consisted of TM receivers, tracking radar, plate and motion-picture cameras, and meteorological sampling devices located at Wallops Island, at Bermuda, aboard ships, and on aircraft. Meteorological data, together with the actual trajectory as determined from photographs, TM, and radar, were used to calculate heating rates for the postflight burnup analysis. Optical coverage, including photographs and spectrographs, was used to supplement the TM data on reactor disassembly.

Wallops Island

TM and tracking radar at the Wallops main base covered the early part of the flight. Standard balloon runs were made to determine wind velocity and direction, which affect the safety of the launch.

Bermuda

The NASA Mercury Station on Bermuda provided downrange radar and TM coverage for RFD-1. An FPS-16 radar was used to track the RS, which carried a C-band transponder (beacon) to aid in acquisition and tracking at maximum distance. To provide optical coverage for this flight, Sandia installed and operated the following equipment at High Point, Bermuda:

1. ME-16 Tracking Mount:
   a. One 70-mm Photosonics 10B, operating at 90 frames per second, using a lens with a 120-inch focal length.
   b. One 35-mm Mitchell, operating at 96 frames per second, using a Paxar lens with an 18-inch focal length.
   c. One 35-mm Mitchell, operating at 96 frames per second, using a lens with a 2-inch focal length.
2. LA-24 Tracking Mount:
   a. One streak spectrograph on the 120-inch main tube.
   b. One sampling photometer.
   c. One 35-mm Mitchell, operating at 96 frames per second, using a lens with a 40-inch focal length.
3. Plate Cameras: Three each, using f2.5 lenses with a 12-inch focal length, and 10 x 12-inch glass plates.
4. Plate Spectrographs: Six each, using f2.5 lenses with a 12-inch focal length, 10 x 12-inch glass plates, and Bausch and Lomb 600-lines/mm transmission gratings.
5. Plate Trajectory Cameras: Three K-37's, using f2.5 lenses with a 12-inch focal length, and modified to take 12 x 12-inch glass plates.
6. Cinespectrograph: One hand-tracked 70-mm Photosonics 10A, operating at 10 frames per second, using an f2.0 lens with a 4-inch focal length, and a Bausch and Lomb 600-lines/cm transmission grating.
7. Hand-Tracked Camera: One 16-mm Bell and Howell, operating at 126 frames per second, using an f2.5 lens with a 6-inch focal length.

To obtain data on high-altitude winds and air density, Sandia and NASA fired six small sounding rockets in groups of three. The first three were fired soon after RFD-1 impacted, and the second group about 12 hours later. Each group consisted of a Sandia Kisha-Judi rocket with densitometer, a Sandia Deacon-Judi rocket with chaff, and a NASA Arcas sounding rocket.

Ships

NASA's Range Recoverer, Navy's Harwood, and AMR's ORV Gulf were stationed in the impact area and were equipped with TM and SARAH (search and rescue and homing) receivers.

Aircraft

Five aircraft were in the recovery area for the purpose of data acquisition. There were two Air Force Special Weapons Center (AFSWC) C-54's carrying TM, SARAH, and optical equipment. Each TM station consisted of two antennas, four receivers, a diversity combiner, and a magnetic tape recorder. The optical equipment in each plane comprised one streak spectrograph using an f2.5 lens with a 12-inch focal length, and a 16-mm Milliken motion picture camera, operating at 400 frames per second, using an f2.5 lens with a 6-inch focal length. One of these aircraft also carried a sampling photometer. AMR provided two C-130's equipped with TM receivers. NASA provided a DC-4 which took motion pictures and spectrograph photos of the reentry. The NASA aircraft was farther downrange than the rest of the aircraft, and obtained excellent optical coverage of the trajectory during the time of maximum aerodynamic heating.

SECTION IV -- PREFLIGHT TESTS AND ANALYSIS

Trajectory and Burnup Analysis

The preflight analysis of reactor burnup was based on the nominal design trajectory for the RFD-1 flight. This trajectory, designated SNAP-394, was computed using a CDC 1604 computer and the Theoretical Trajectory Program A (TTA), a computer program described in SC-RR-64-510. Figure 11 shows the computed velocity and altitude versus time. Appendix C of this report covers the aeroheating subroutines of the TTA program. Figure 12 and Table II show the heating rates and the integrated heating for the stagnation point of a sphere with a 1-foot radius re-entering on the SNAP-394 trajectory. The ballistic coefficients used in calculating this trajectory are shown in Figure 13. The variation shown is due to weight loss and the change of C_D resulting from changes in configuration and Mach number. Vehicle configuration and weight versus altitude were found by an iterative process using a theoretical analysis of reactor burnup and RV ablation. The drag coefficients were based on experimental results from extensive wind-tunnel tests.

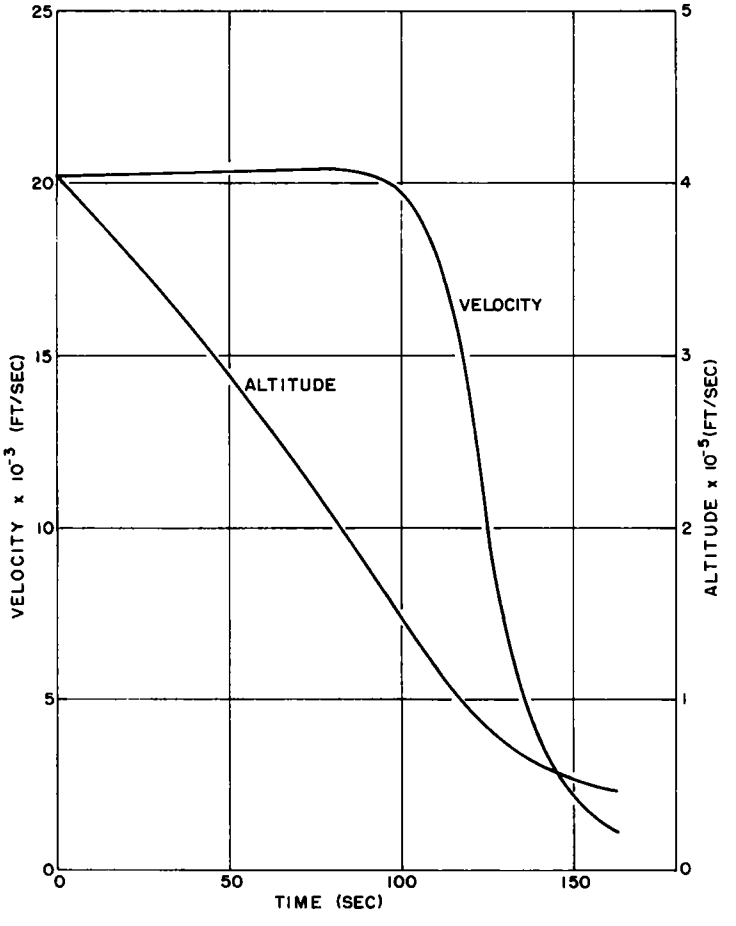

Figure 11. RFD-1 velocity and altitude vs time, as computed for the SNAP-394 trajectory

Figure 12.

Computed heating rates and integrated heating for the stagnation point of a 1-foot-radius sphere re-entering on the SNAP-394 trajectory

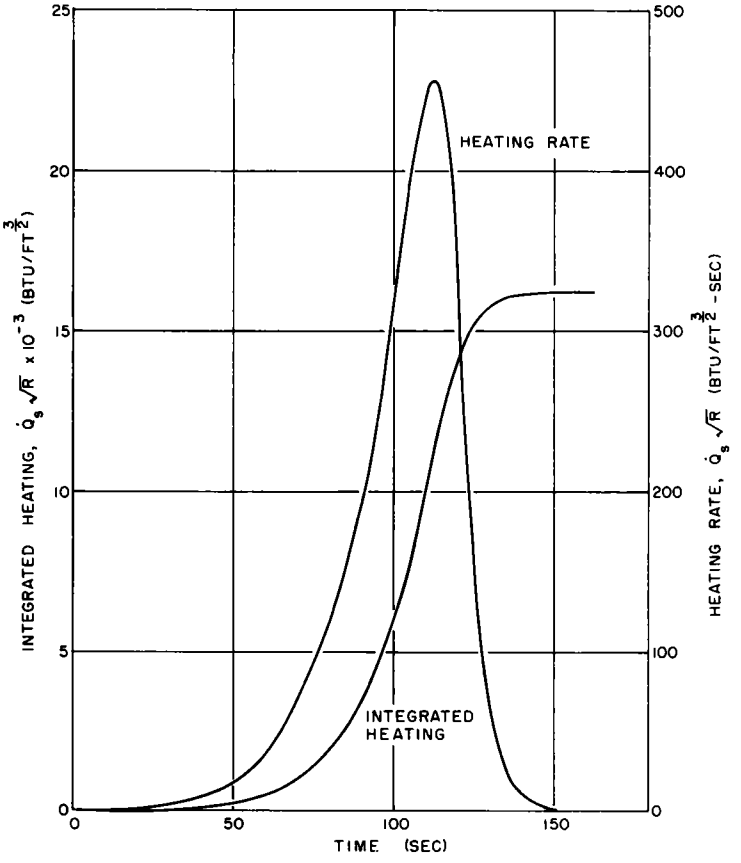

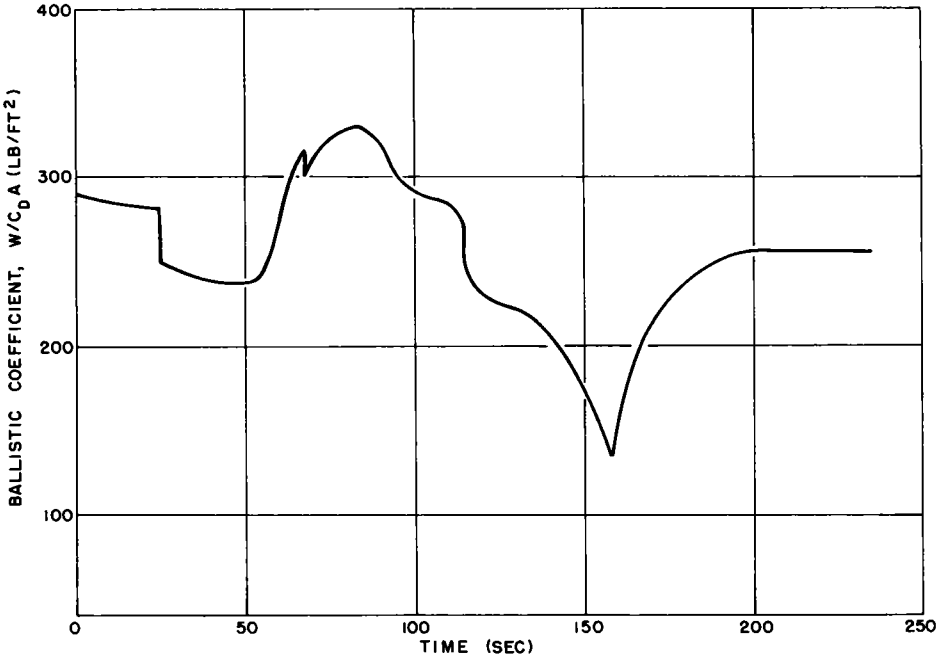

Figure 13. Ballistic coefficient versus time used in calculating the SNAP-394 trajectory

TABLE II

Computed Heating Rates and Integrated Heating for the Stagnation Point of a 1-foot-Radius Sphere Re-entering on the SNAP-394 Trajectory

Time (sec)	Altitude (ft)	Velocity (ft/sec)	Heating Rate ($BTU/ft^{3/2}$-sec)	Integrated Heat ($BTU/ft^{3/2}$)
0.000	404066	20178	1.23	0.00
1.000	401991	20181	1.28	1.25
2.000	399906	20184	1.33	2.56
3.000	397810	20188	1.38	3.91
4.000	395705	20191	1.44	5.32
5.000	393589	20194	1.50	6.79
6.000	391462	20197	1.56	8.32
7.000	389326	20201	1.62	9.91
8.000	387179	20204	1.69	11.57
9.000	385022	20207	1.76	13.30
10.000	382855	20211	1.84	15.10
11.000	380677	20214	1.93	16.99
12.000	378490	20217	2.01	18.95
13.000	376292	20221	2.10	21.01
14.000	374083	20224	2.20	23.16
15.000	371865	20227	2.30	25.41
16.000	369636	20231	2.41	27.76
17.000	367397	20234	2.53	30.23
18.000	365148	20238	2.65	32.82
19.000	362888	20241	2.78	35.53
20.000	360619	20245	2.92	38.38
21.000	358339	20248	3.07	41.37
22.000	356048	20252	3.22	44.52
23.000	353748	20255	3.39	47.82
24.000	351437	20259	3.57	51.30
24.620	350000	20261	3.69	53.55
25.000	349116	20262	3.76	54.97
26.000	346785	20266	3.96	58.83
27.000	344443	20269	4.18	62.90
28.000	342092	20273	4.42	67.20
29.000	339730	20277	4.67	71.74
30.000	337357	20280	4.94	76.55
31.000	334975	20284	5.23	81.63
32.000	332582	20288	5.54	87.01
33.000	330179	20291	5.87	92.72
34.000	327766	20295	6.24	98.77
35.000	325342	20299	6.63	105.20
36.000	322909	20302	7.05	112.04
37.000	320465	20306	7.51	119.31
38.000	318010	20310	8.00	127.06
39.000	315546	20314	8.53	135.32
40.000	313071	20317	9.11	144.14
41.000	310586	20321	9.73	153.56
42.000	308091	20325	10.41	163.63
43.000	305586	20329	11.16	174.40
44.000	303070	20332	11.97	185.96
45.000	300544	20336	12.85	198.37
46.000	298008	20340	13.77	211.68
47.000	295461	20344	14.71	225.92
48.000	292905	20347	15.71	241.12
49.000	290338	20351	16.79	257.36
50.000	287761	20355	17.95	274.73
51.000	285174	20359	19.20	293.30
52.000	282576	20362	20.55	313.17
53.000	279968	20366	21.98	334.42
54.000	277350	20370	23.53	357.17
55.000	274722	20373	25.19	381.52
56.000	272084	20376	26.98	407.59

TABLE II
(Cont)

Time (sec)	Altitude (ft)	Velocity (ft/sec)	Heating Rate ($BTU/ft^{3/2}$-sec)	Integrated Heat ($BTU/ft^{3/2}$)
57.000	269436	20380	28.89	435.51
58.000	266777	20383	30.96	465.43
59.000	264108	20386	33.18	497.48
60.000	261429	20389	35.57	531.84
61.000	258741	20392	38.14	568.68
62.000	256041	20395	40.91	608.19
63.000	253332	20398	43.89	650.57
64.000	250613	20400	47.05	696.02
65.000	247884	20403	50.39	744.72
66.000	245145	20405	53.67	796.76
67.000	242395	20407	57.01	852.10
67.144	242000	20407	57.51	860.31
68.000	239636	20408	60.57	910.88
69.000	236867	20410	64.30	973.30
70.000	234088	20410	68.22	1039.55
71.000	231300	20411	72.32	1109.80
72.000	228501	20411	76.61	1184.25
73.000	225693	20410	81.10	1263.09
74.000	222875	20410	85.80	1346.53
75.000	220048	20408	90.70	1434.76
76.000	217211	20406	95.81	1527.99
77.000	214364	20403	101.14	1626.45
78.000	211509	20399	106.70	1730.36
79.000	208644	20395	112.49	1839.93
80.000	205770	20389	118.51	1955.41
81.000	202887	20383	124.76	2077.02
82.000	199996	20375	131.25	2205.01
83.000	197095	20367	137.98	2339.60
83.033	197000	20366	138.20	2344.15
84.000	194187	20356	144.94	2481.06
85.000	191269	20344	152.13	2629.60
87.000	185412	20314	167.22	2948.80
89.000	179524	20275	183.21	3299.08
91.000	173608	20227	200.84	3682.85
93.000	167668	20165	221.40	4104.60
95.000	161707	20084	243.64	4569.36
97.000	155732	19982	267.30	5080.06
99.000	149749	19852	294.67	5641.42
101.000	143766	19684	324.00	6259.77
103.000	137797	19468	354.19	6937.82
105.000	131856	19194	384.11	7676.15
107.000	125961	18850	412.10	8472.68
109.000	120134	18421	435.92	9321.40
111.000	114403	17891	452.55	10211.07
113.000	108801	17238	457.95	11123.43
115.000	103369	16432	447.53	12031.54
117.000	98162	15418	414.98	12897.74
119.000	93251	14181	359.67	13676.18
121.000	88694	12833	294.34	14331.86
123.000	84510	11484	230.70	14856.62
125.000	80695	10178	173.50	15259.75
127.000	77231	8959	126.11	15557.73
129.000	74089	7858	89.89	15771.88
131.000	71234	6885	63.47	15923.61
133.000	68628	6029	44.46	16030.30
138.000	63009	4328	17.78	16179.22
143.000	58340	3137	7.19	16234.96
148.000	54311	2313	2.94	16257.65
153.000	50720	1718	1.22	16267.00
158.000	47458	1298	0.46	16270.79
163.000	44399	1041	0.28	16272.38

Wind-tunnel tests were conducted in the AEDC 100-inch hot-shot tunnel to determine the ratios of local heating on the full-scale reactor to stagnation heating on a hemisphere with a 1-foot radius. These tests are discussed in Appendix A. As can be seen from the tabulated data in Appendix A, heating ratios varied with Reynolds number in some areas. The free-stream Reynolds number for Trajectory 394 is shown in Figure 14. In areas such as the reflector band, which were too small to instrument in the wind-tunnel tests, heating ratios were found analytically, using properties behind a bow shock assumed to form over the entire frontal area of the reactor. Since only a small portion of the heating during the RFD-1 flight took place in free-molecular flow, all heating was assumed initially to be in continuum flow. Refined calculations made later included free-molecular heating. The heating ratios, Fq, used for the zero-degree-angle-of-attack preflight analysis are shown in Table III. The variations listed in some areas include heating gradients over a surface caused by shock-wave/boundary-layer interactions as well as variations with Reynolds number.

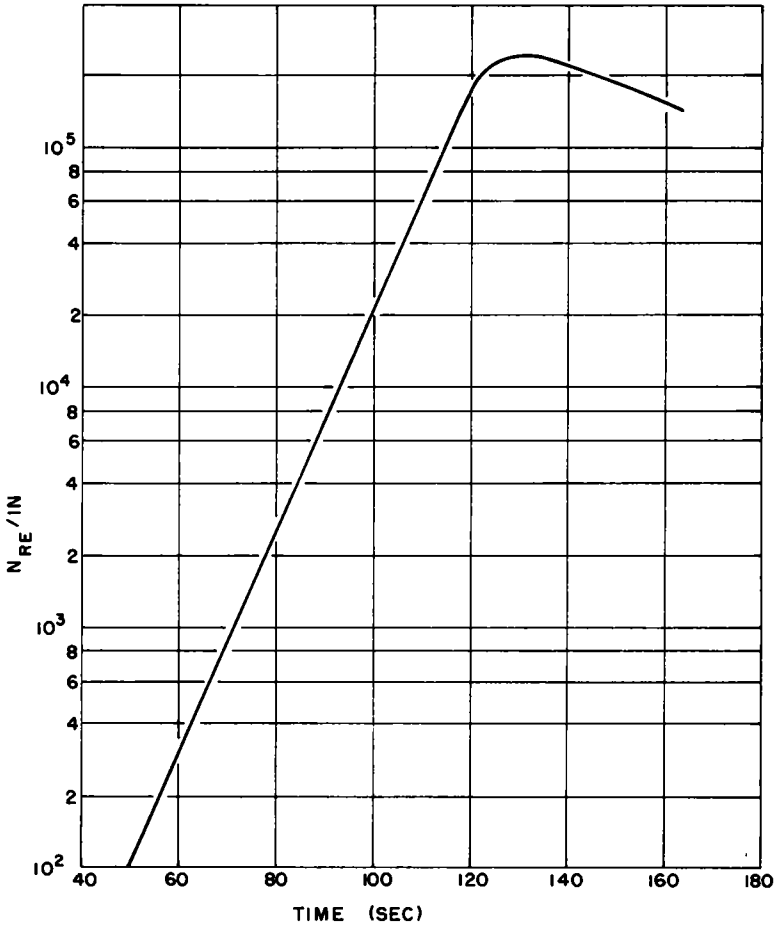

Figure 14. Free-stream Reynolds number used for the SNAP-394 trajectory

TABLE III

Heating Ratios for Preflight Analysis

Location	Heating Ratios $F_q(ft^{-1/2})$
NaK fill tube (front)	6.0
NaK fill tube (sides)	0.20
Transverse NaK tube (front)	2.2 to 4.2
Transverse NaK tube (back)	0.30
Fin (front)	5.0
Fin (sides, forward)	0.115
Fin (sides, aft)	0.090
Pump (front)	1.5 to 2.3
Pump (sides)	0.30
Core-vessel cover (behind pump)	0.25
Core-vessel cover (outboard of pump)	2.2 to 3.1
Core-vessel cover (without pump)	0.90 to 2.3
Lip weld (behind NaK tube)	0.15 to 0.45
Lip weld (behind fins)	0.4 to 0.7
Lip weld (in unobstructed flow)	3.2
Lip weld (without pump)	1.7
Core-vessel sides (forward)	0.07 to 0.16
Core-vessel sides (aft)	0.02 to 0.13
Core-vessel base (front)	0.7 to 1.3
Core-vessel base (sides)	0.07 to 0.18
Reflector band joint (front)	12.1
Reflector band joint (sides)	0.27
Band support	1.5
Band standoff	3.2

Internal-heating calculations were made by using both the "Herman" program (Appendix E) with a digital computer and with the Thermalog (Appendix D). The time-temperature curves resulting from these studies are shown in Figures 15 through 22. Times and altitudes calculated for the various stages of disassembly are given in Table IV. Times are given from an altitude of 400,000 feet.

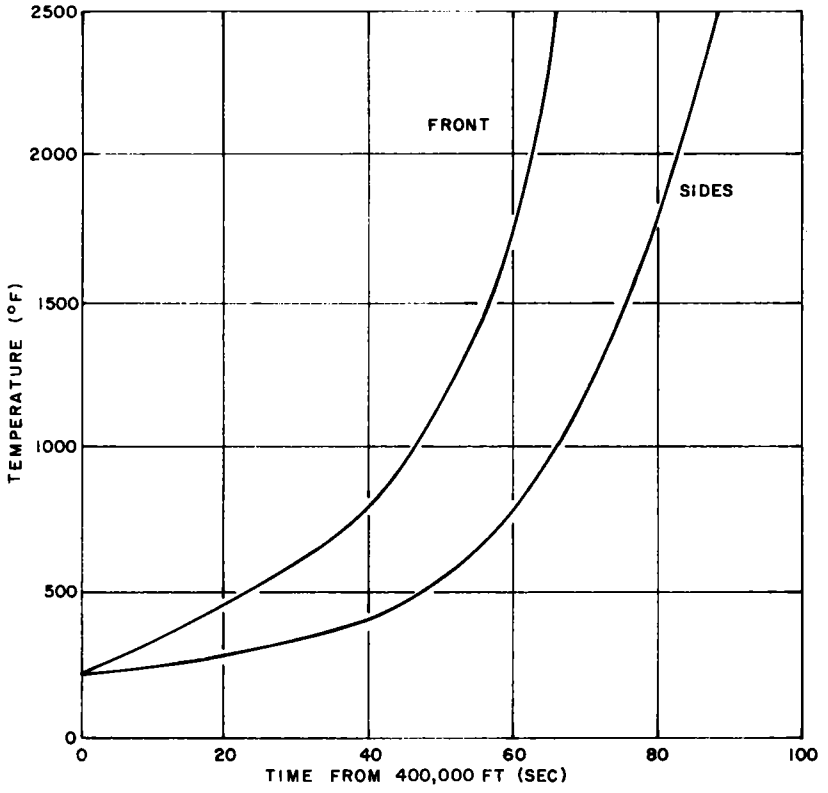

Figure 15.

Calculated time-temperature curves for front and sides of NaK fill tube (T12)

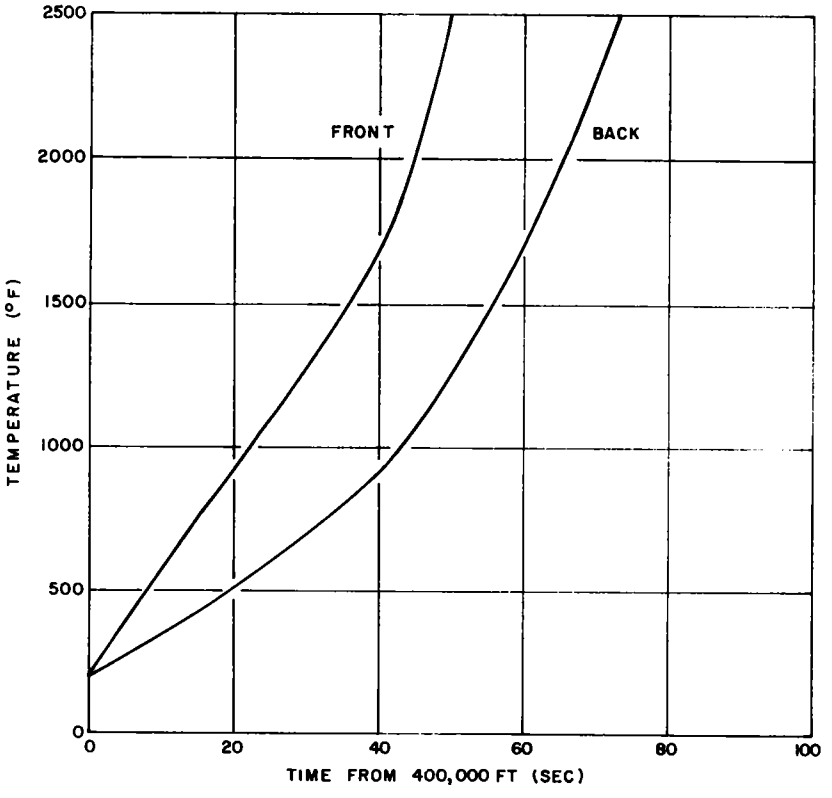

Figure 16.

Calculated time-temperature curves for front and back of transverse NaK tube (T9, T10)

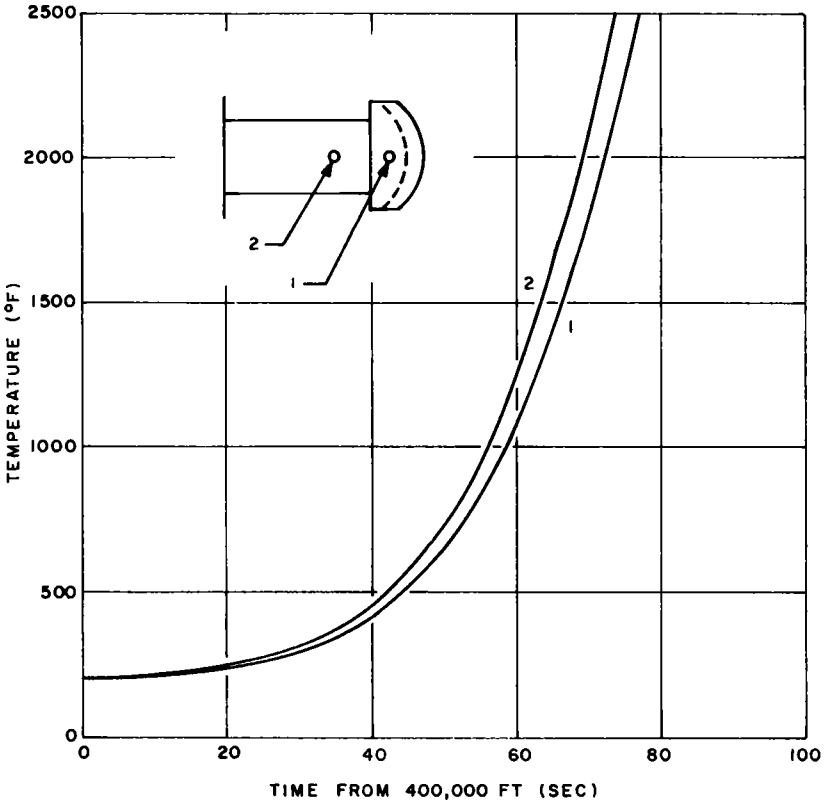

Figure 17. Calculated time-temperature curves for band standoff

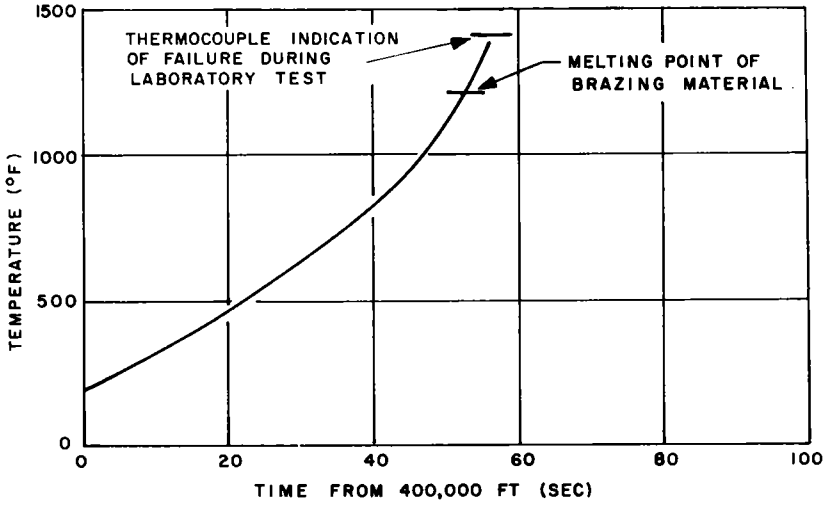

Figure 18. Calculated time-temperature curve for reflector band joint (T7)

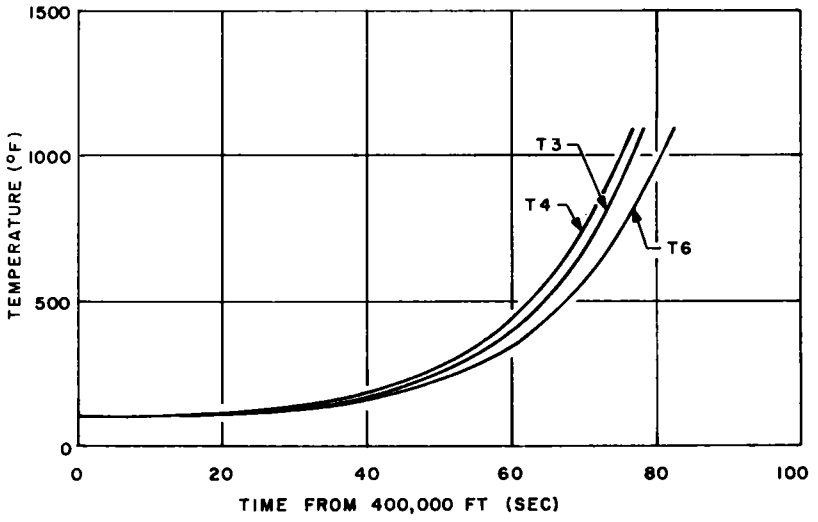

Figure 19. Calculated time-temperature curves for pump fin (T3, T4, T6)

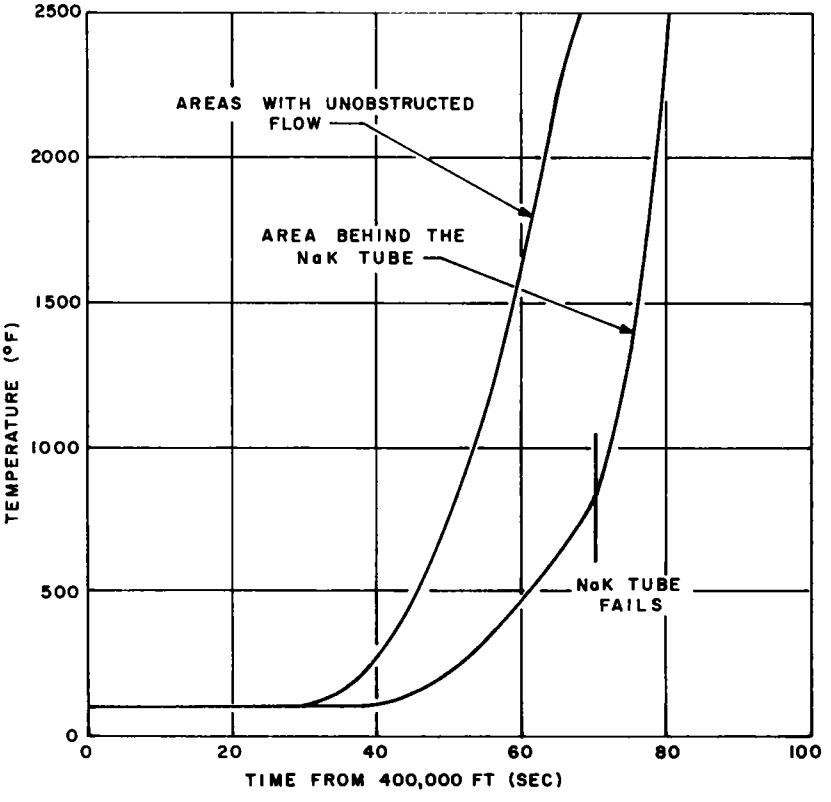

Figure 20. Calculated time-temperature curves for core-vessel cover 3.75 inches from centerline

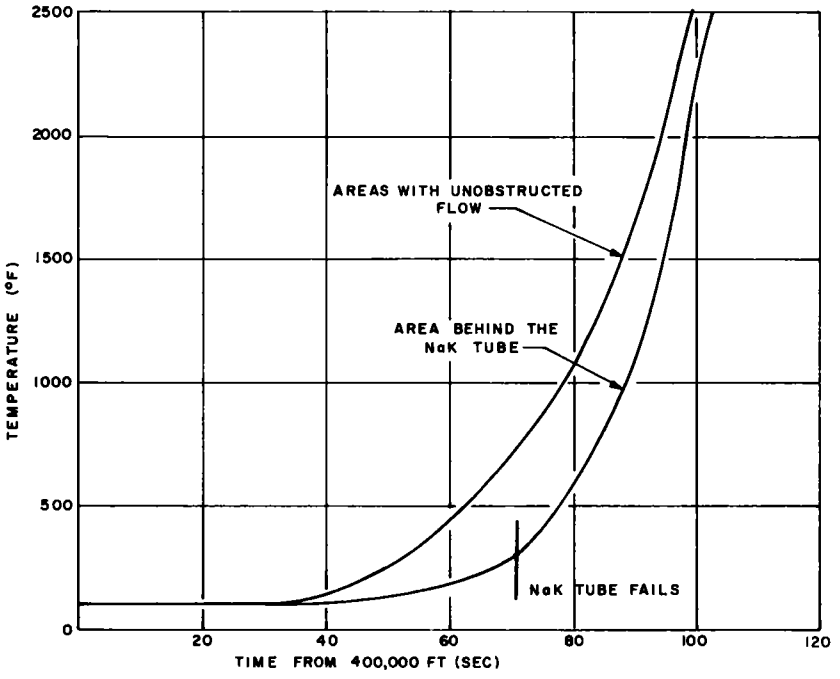

Figure 21. Calculated time-temperature curves for lip area (including upper 1-5/32 inch of the vessel)

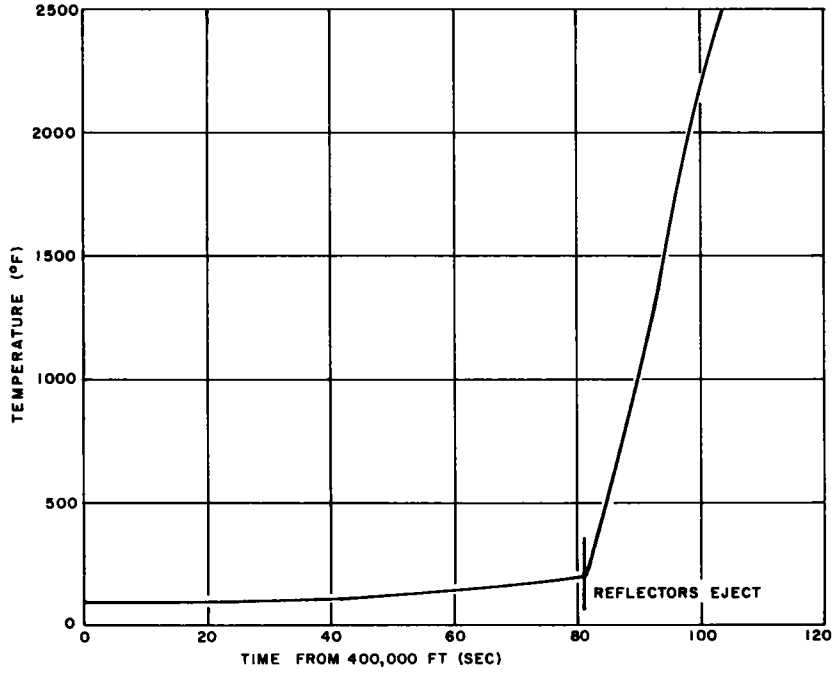

Figure 22. Calculated time-temperature curves for core-vessel sides

TABLE IV

Calculated Altitudes for Stages of Reactor Disassembly

Event	Time (sec)	Altitude (ft)
Reflectors eject	53	279,968
Transverse NaK tube parts	73	225,693
Pump and central cover come off	82	199,996
Pump fins completely melted	83	197,095
Lip area melts	109	120,134
Can sides melt	111	114,403

Radiant-Heat Test

A production SNAP-10A reactor core vessel was tested in the Sandia radiant-heat facility to establish the mode of disassembly and the amount of heat required to melt the vessel and free the fuel rods when exposed to a heat pulse similar to that expected on the RFD-1 flight. The AI-installed thermocouples in the lip-weld area, which were the same as those on the flight models, were monitored to determine their temperature readings at the time of lip or cover failure. Numerous other thermocouples were monitored during the test to determine the temperature profiles in the walls and lip area. Five displacement gages were placed between the top grid plate and the test support to measure the longitudinal thermal expansion of the vessel before failure and to give an indication of when the cover failed.

Re-entry heating conditions, based on the AEDC wind-tunnel tests and a theoretical trajectory, were simulated as nearly as possible in the radiant-heat facility. The heat inputs to various parts of the vessel are shown in Figure 23. Calibration consisted of pyrometer temperature readings of the graphite heating elements, and copper heat-sink calorimeter readings made during several trial runs before the test. The test setup and core vessel before the test are shown in Figures 24 and 25. The purpose of the copper disc in front of the cover (Figure 25) was to reduce the heat input to the center of the cover, offering protection similar to that provided by the NaK pump during re-entry.

Camera coverage showed that the thinnest part of the lip, the forward edge, began to melt at 106 seconds; the heavier portions of the lip did not melt during the entire test. The eventual failure, at 140 seconds, was caused by the top head melting through inboard of the relatively massive lip area, in accordance with the analytical study of reactor burnup. However, even after the failure, portions of the periphery of the top head remained attached to the lip, as shown in Figure 26.

On an earlier, reduced-heating, nondestructive run, the displacement gages showed that the vessel expanded 0.09 inch axially. During the destructive test, the displacement gages showed the vessel expanding for the first 140 seconds of the test. At 140 seconds, they suddenly read full-scale deflection, apparently when the aluminum top grid failed when exposed directly to the heat source. Although the cover failed, if a production, stainless-steel top grid plate had been used, the fuel rods would not have been free to come out because of the flange left by the cover in the lip area. Part of the graphite heating array broke at 135 seconds, preventing completion of the test, so the amount of heat required to completely free the top grid plate was not determined. However, the initial mode of failure and temperature profiles throughout the unit were found.

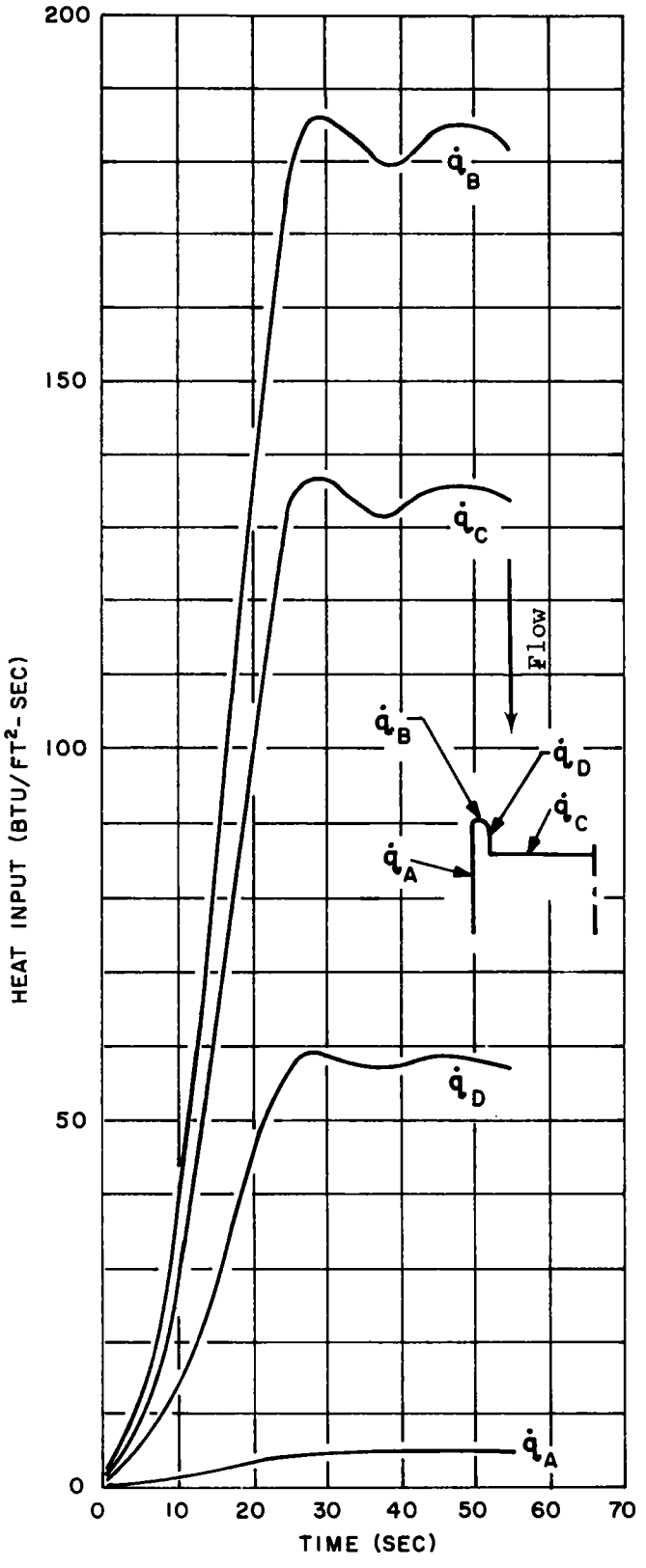

Figure 23. Calculated heat inputs for the second radiant-heat test of the SNAP-10A reactor core-vessel cover

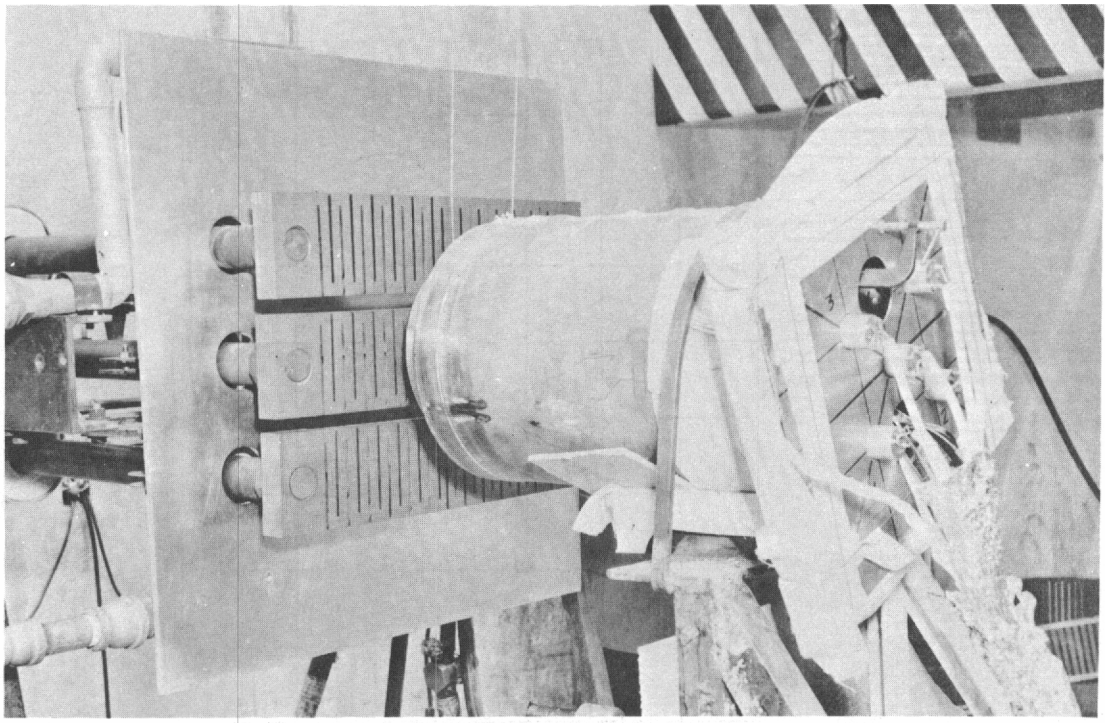

Figure 24. Setup for radiant-heat test

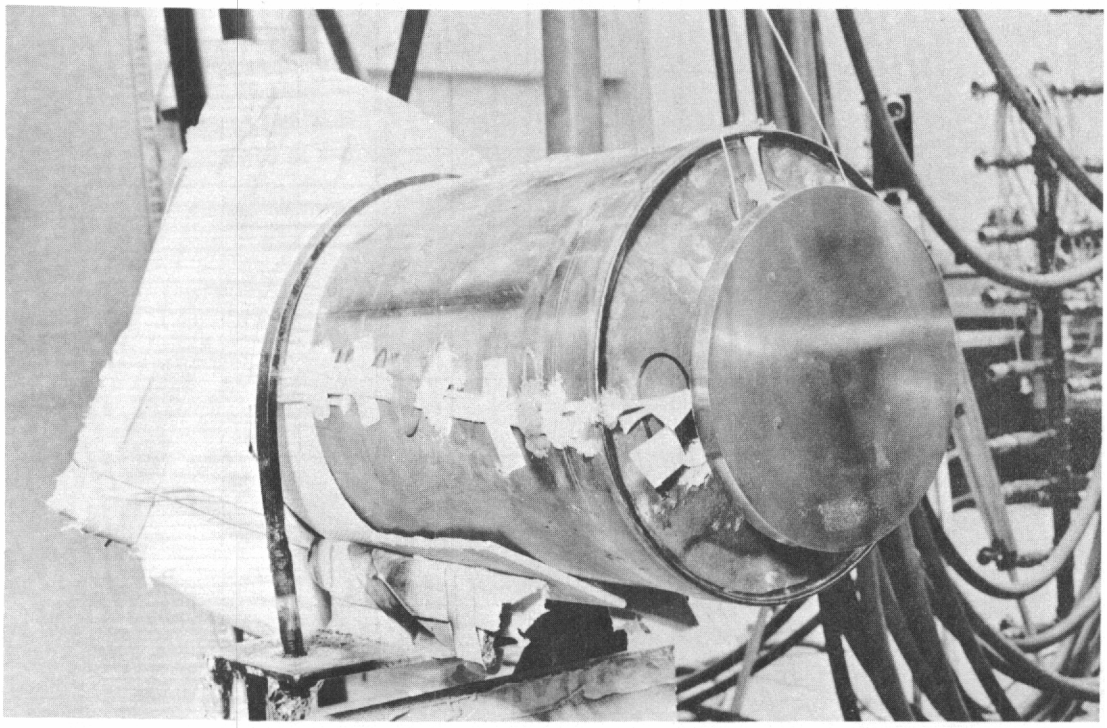

Figure 25. Core vessel used in radiant-heat test

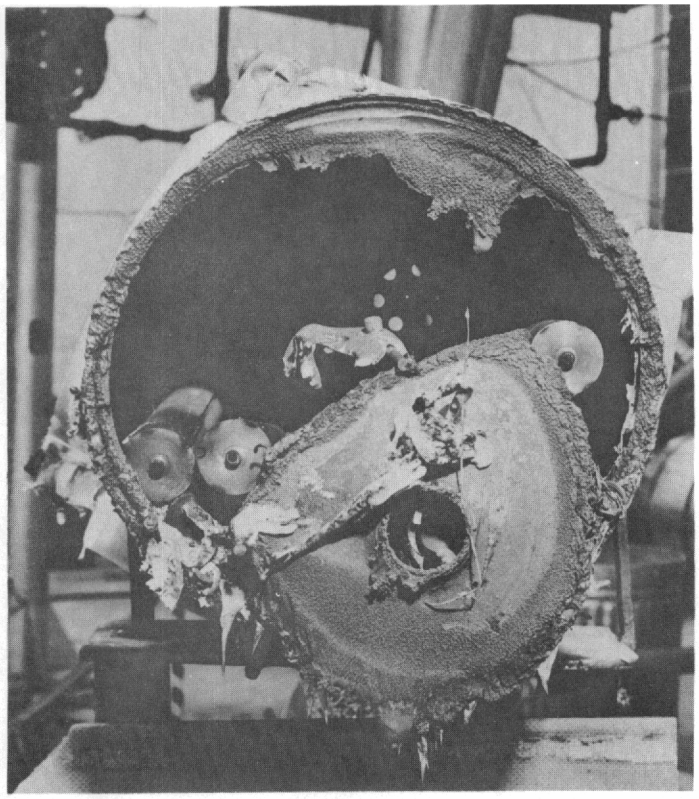

Figure 26. Core vessel after radiant-heat test

Reflector-Ejection Test

A reflector-ejection test was conducted at Sandia to help predict the temperatures that would be read by Thermocouples 7 and 8 (on the band joints) at the time of band separation, and to determine if the reflectors would clear the RV during a static test. Qualification Reactor Number 2 was mounted vertically on an RV nose, as shown in Figure 27. The brazed fusible link on which flight-test Thermocouple 2 was installed was heated to failure by three propane torches. The thermocouple read 1404°F when the band failed, although the brazing material melts at 1220°F. This disparity was due to the higher heating rates to the exposed thermocouple wires, and to the lag in temperature rise between the thermocouples welded to the surface and the brazing material between the band segments. Figure 28 shows the time-temperature plot of the thermocouple during the test. For higher heating rates, the indicated temperature would have been even higher at the time that the brazed joint melted. The first indication of band separation came with the opening of the thermocouple 23.5 seconds after heating began, followed by the opening of Switch 7 (between the core-vessel wall and the reflector) at 23.7 seconds, and the opening of Switch 8 (attached to the hinge) at 24.0 seconds.

Of the eight thermocouple connectors between the reflectors and the core vessel, only one disconnected. The other seven wires broke, but only after four support brackets were torn loose from the core vessel. Three of the four brackets holding the lead wires to the band also were pulled loose when the reflectors ejected. These four brackets were not required for structural strength, and were removed from the flight reactor to reduce the possibility of the reflectors hanging up during the flight test.

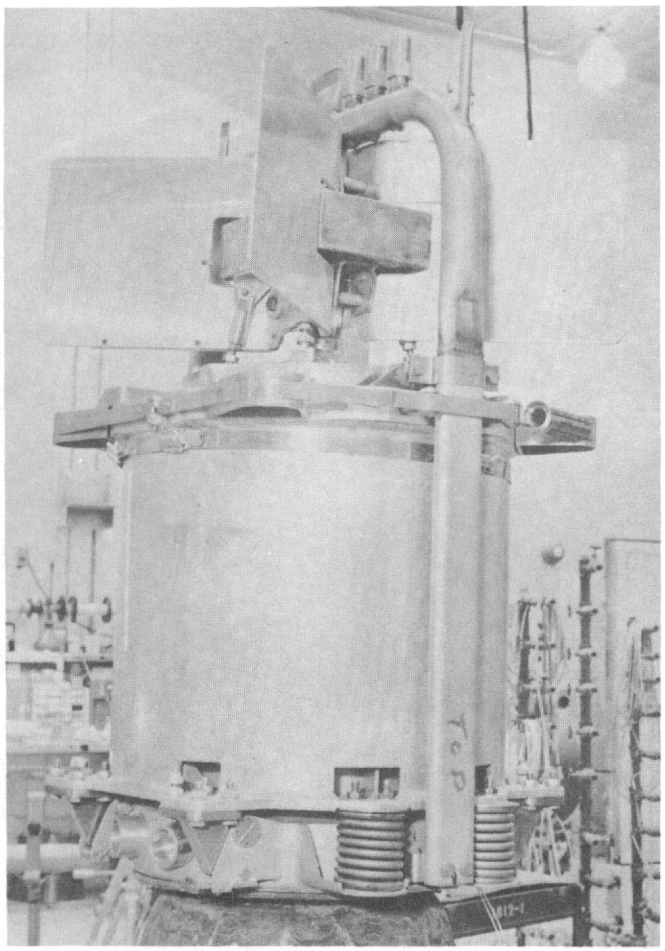

Figure 27.

Setup for reflector-ejection test

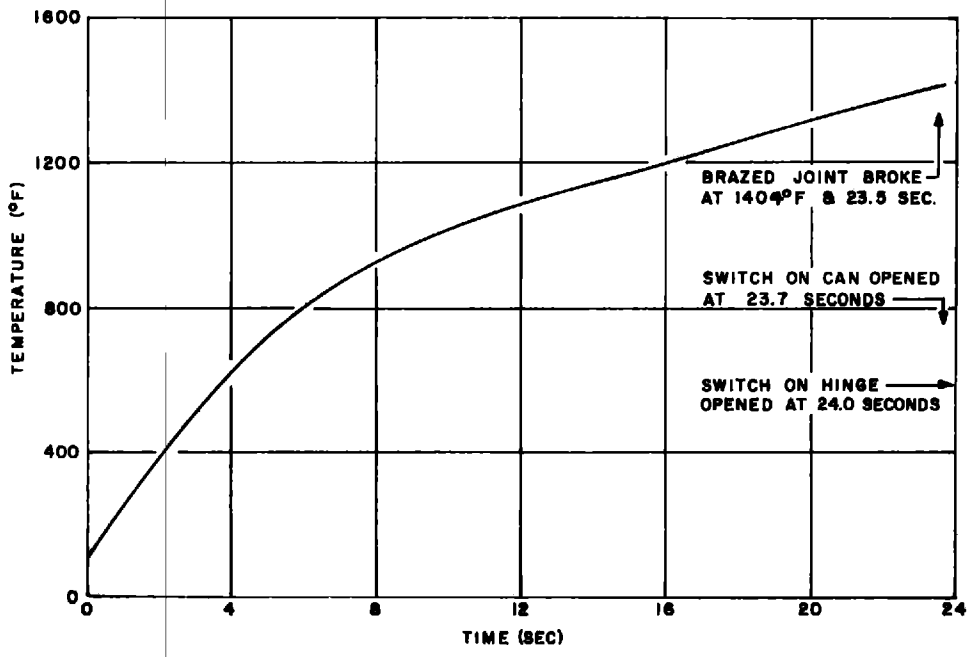

Figure 28. Temperature rise of the brazed joint, and subsequent switch openings during the reflector-ejection temperature test of the retainer band

Both reflectors cleared the RV, but Reflector 1, which had to break more lead wires and brackets, did not have the radial motion that Reflector 2 did, as shown in Figure 29. Fastax motion pictures taken during the test showed the reflectors clearing the RV nose by 10 and 14 inches.

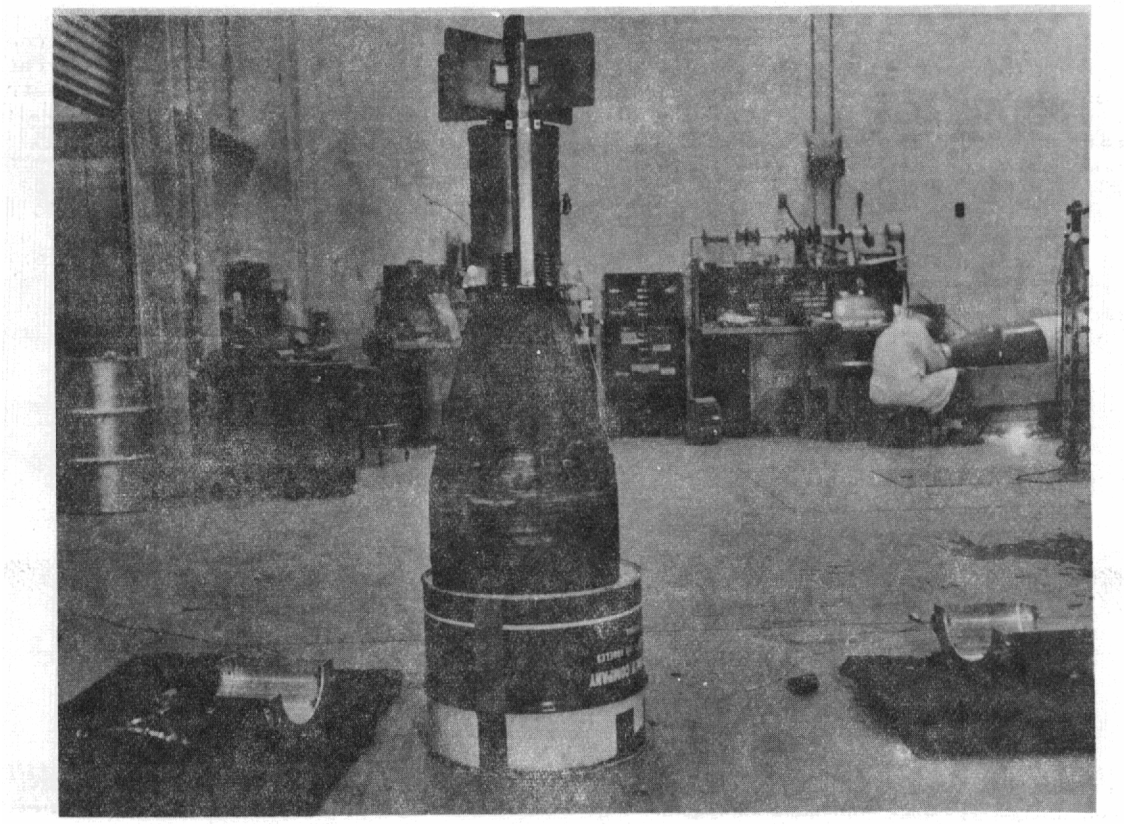

Figure 29. Position of reflectors after ejection test

Environmental Tests and Instrumentation Checkout

After the bases of the qualification and flight reactors were potted, all reactor thermocouples, resistance bulbs, and the attached fuel-rod heat meter were checked. The checks were made by placing the reactors in an oven preheated to 165°F and monitoring the net voltage from each thermocouple and the heat meter and the resistance of the reference-junction thermistors. Knowing the temperature of the reference junction and the net voltage output, local temperatures could be determined. Since the reference junction was covered by several inches of potting compound, its temperature rise was much slower than that of the thermocouples in the rest of the reactor, resulting in a positive output until the unit reached equilibrium temperature. All thermocouples and resistance bulbs operated satisfactorily on all units. The thermocouples and resistance bulbs were calibrated at AI before the reactors were shipped to Sandia.

The qualification reactors were attached to corresponding re-entry vehicles during all the system environmental tests. These tests were designed to simulate environments expected during shipping, storage, and flight. For the purpose of

certifying the re-entry system, the qualification units were subjected to more extreme conditions than those they were expected to encounter in the cycle from manufacture to recovery. On the other hand, the flight units were subjected to acceptance tests which were less severe than the expected environments. The acceptance tests were to show only that the two flight systems were properly fabricated and that the instrumentation and TM would operate properly during and after the tests. A detailed description of the environments and testing procedures can be found in Chapters XII and XIII of SC-RR-64-511.

During the latter part of each test series, the RS was subjected to three temperature cycles from -5° to 160°F, as shown in Figure 30. The TM was operated intermittently to check the functioning of the reactor thermocouples through the TM system. As with the previously described temperature check, the thermocouples responded to temperature changes more rapidly than did the reference junction, resulting in an emf during the entire transient part of the cycle. Again, all thermocouples functioned in the expected manner, with those closest to the surface or in materials with a high thermal diffusivity responding the most rapidly. No thermocouple responded less rapidly than expected, indicating that there were no shorts and no intermittent or continuous opens. The switches could not be tested for operation without destruction of the reactor, so the only switches that were checked were Switches 7 and 8, which were checked in qualification Unit 2 as described previously. However, none of the switches opened as a result of any of the environmental tests.

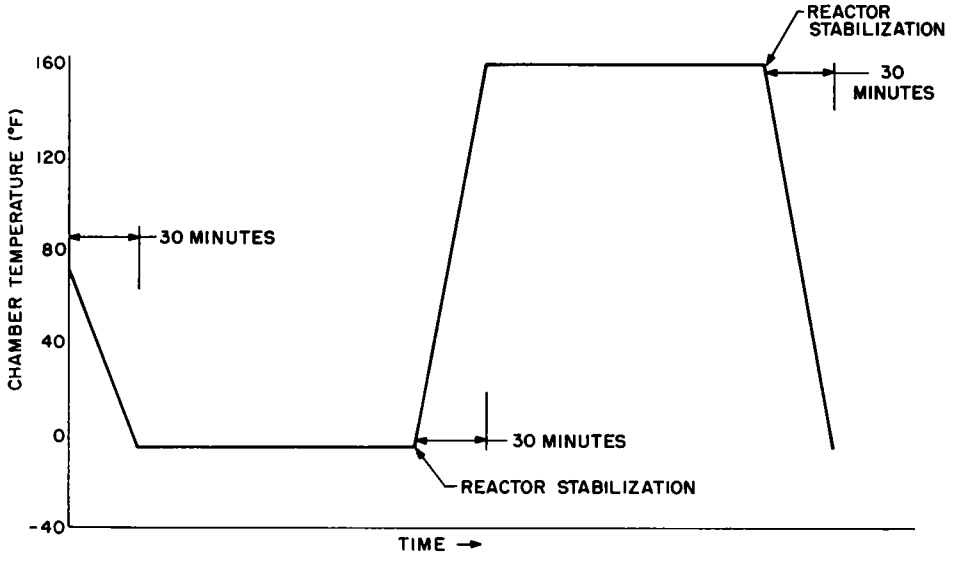

Figure 30. Temperature cycle for environmental tests of the qualification and flight reactors

SECTION V -- POSTFLIGHT ANALYSIS AND FLIGHT DATA

Analytical Analysis

A postflight analysis of reactor heating has been made in an effort to more accurately predict the altitude of reactor disassembly. This analysis was based on ratios of local to stagnation-point heating obtained in hot-shot tunnels before and after the flight, along with the actual trajectory observed during the RFD-1 flight. Predictions of temperature versus time for various parts of the reactor were made with the aid of the "Herman" computer program (Appendix E).

Flight data are plotted in Figures 31 through 50, along with preflight and postflight data, when calculated. Table V lists parameters and trajectories used in the analysis.

TABLE V

Trajectory Parameters Used in the Postflight Analysis of Reactor Heating

Velocity	19,928 ft/sec
Angle of attack (α)	0 degrees
Re-entry angle (γ)	-5.82 degrees
Density	Measured after launch
Local heating ratios	As determined in tests at Rhodes and Bloxsom and at AEDC

(Conditions listed are for an altitude of 400,000 feet and for Trajectory 635.)

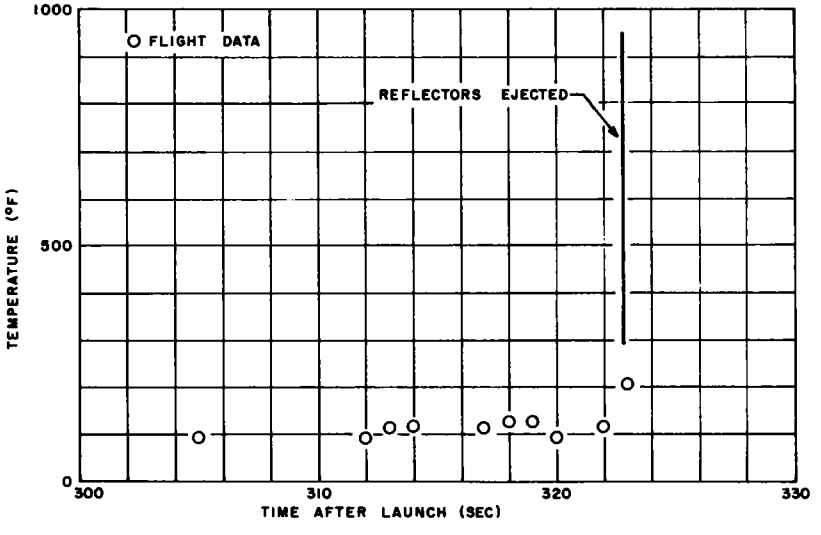

Figure 31. T1 (bracket, band support) temperatures during the RFD-1 flight

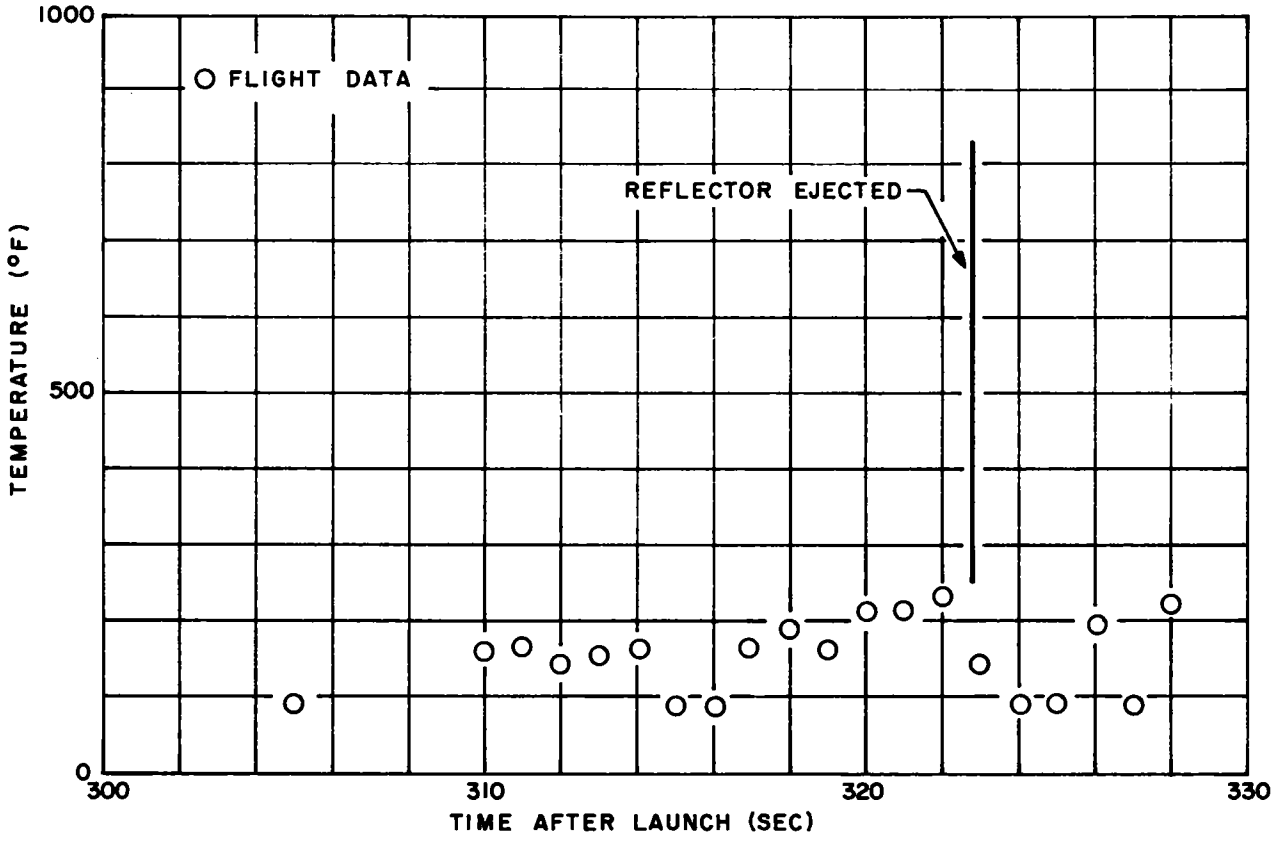

Figure 32. T2 (band standoff) temperatures during the RFD-1 flight

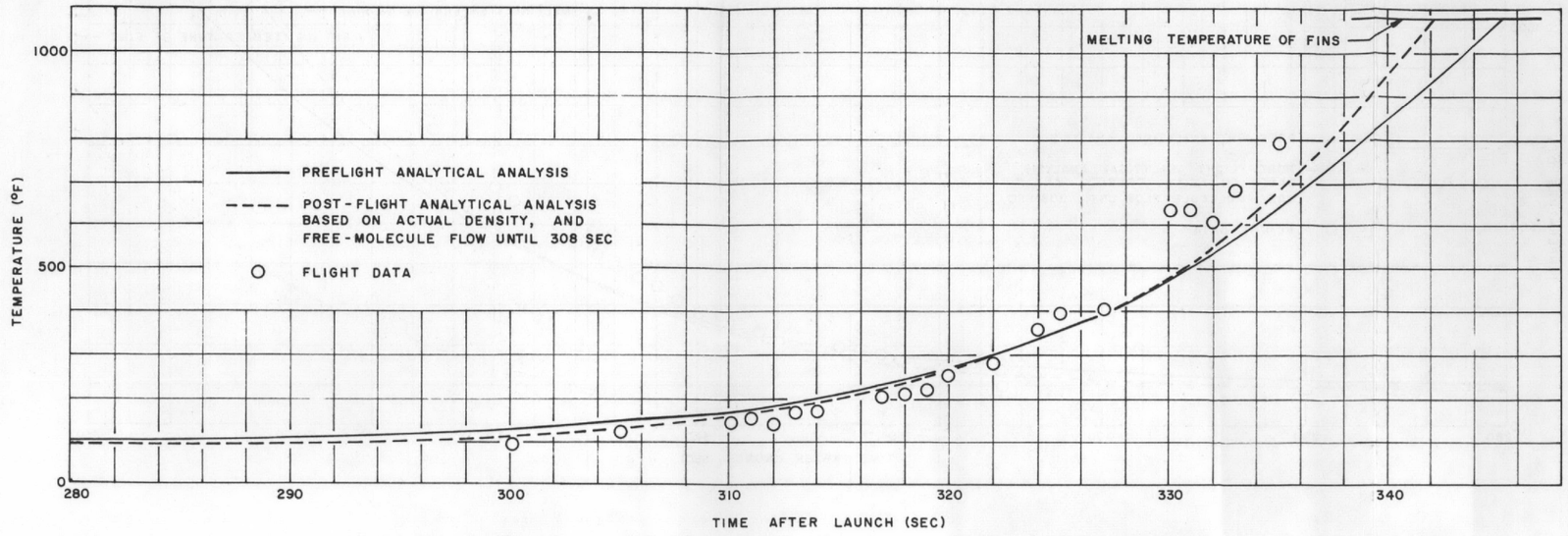

Figure 33. T3 (fin, center) temperatures as measured during the RFD-1 flight and as calculated in the preflight and postflight analyses

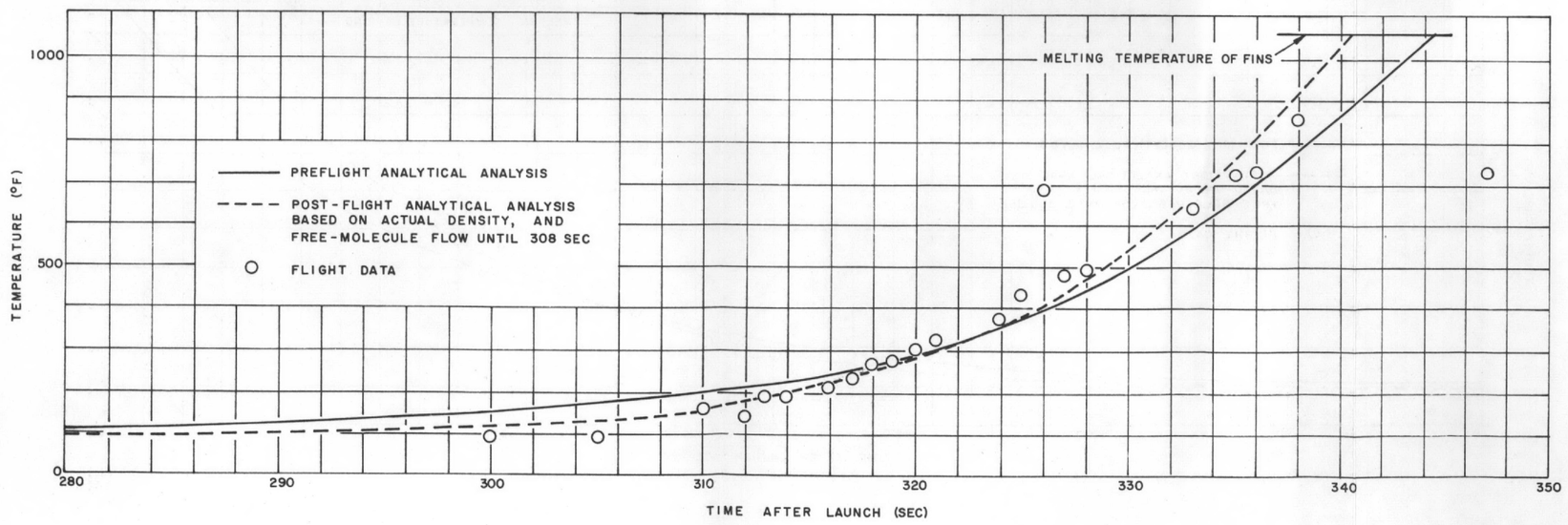

Figure 34. T4 (fin, trailing, outer) temperatures as measured during the RFD-1 flight and as calculated in the preflight and postflight analyses

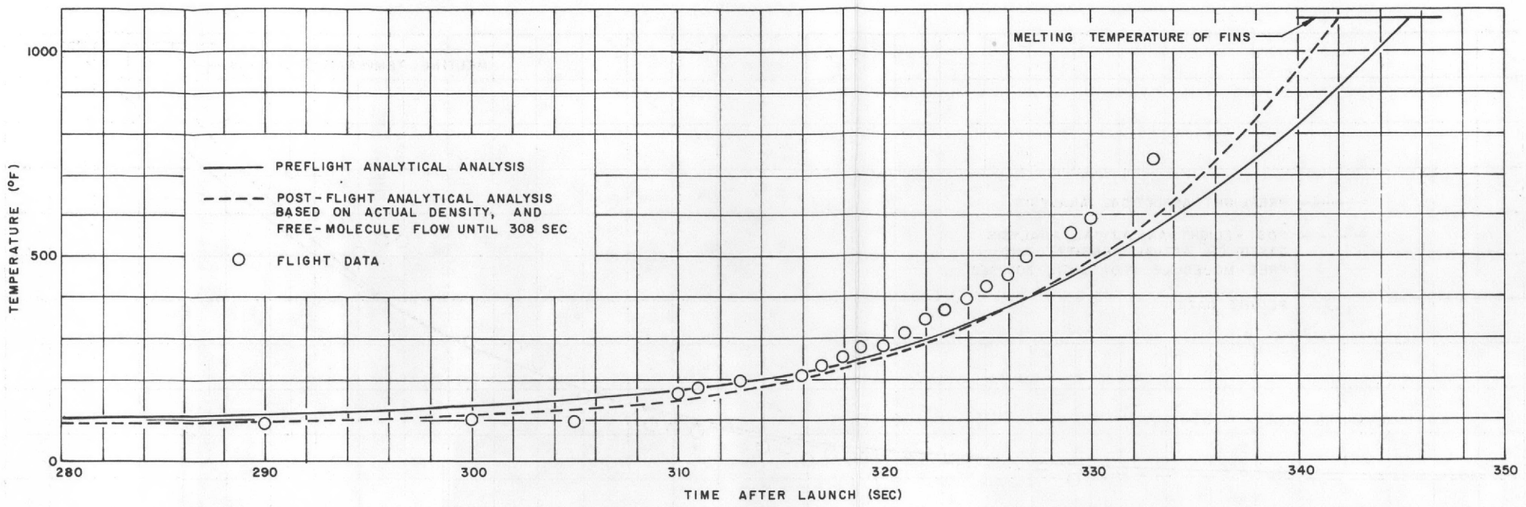

Figure 35. T5 (fin, center, opposite T3) temperatures as measured during the RFD-1 flight and as calculated in the preflight and postflight analyses

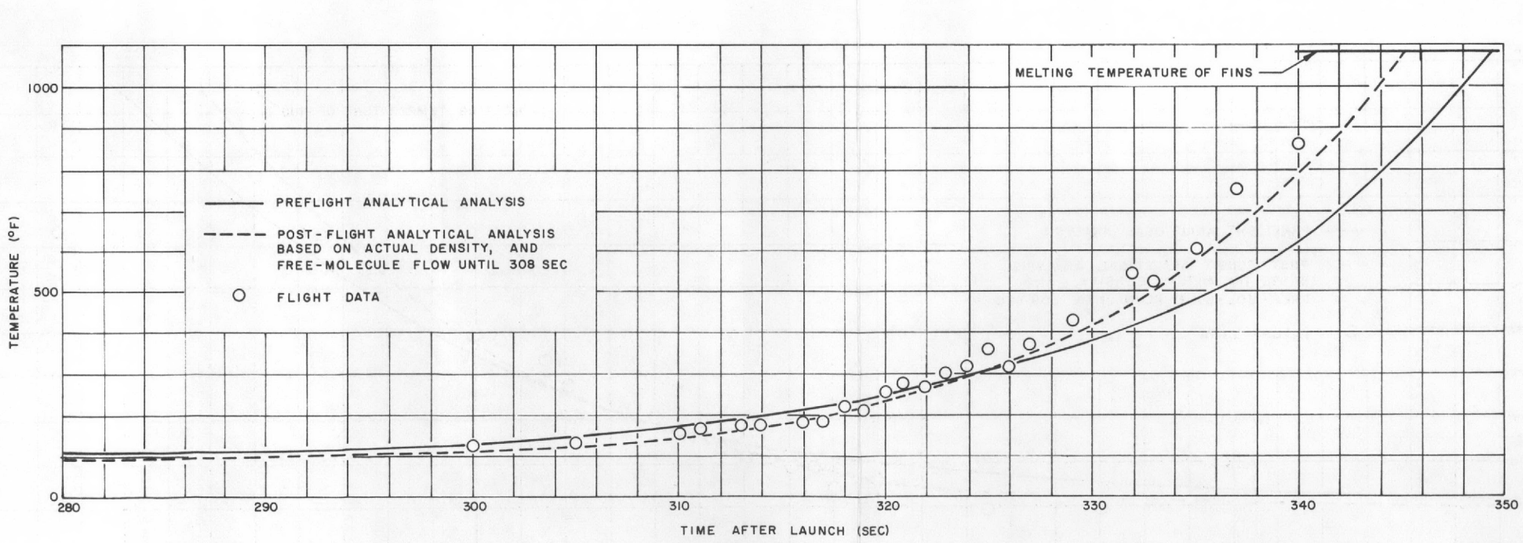

Figure 36. T6 (fin, trailing, inner) temperatures as measured during the RFD-1 flight and as calculated in the preflight and postflight analyses

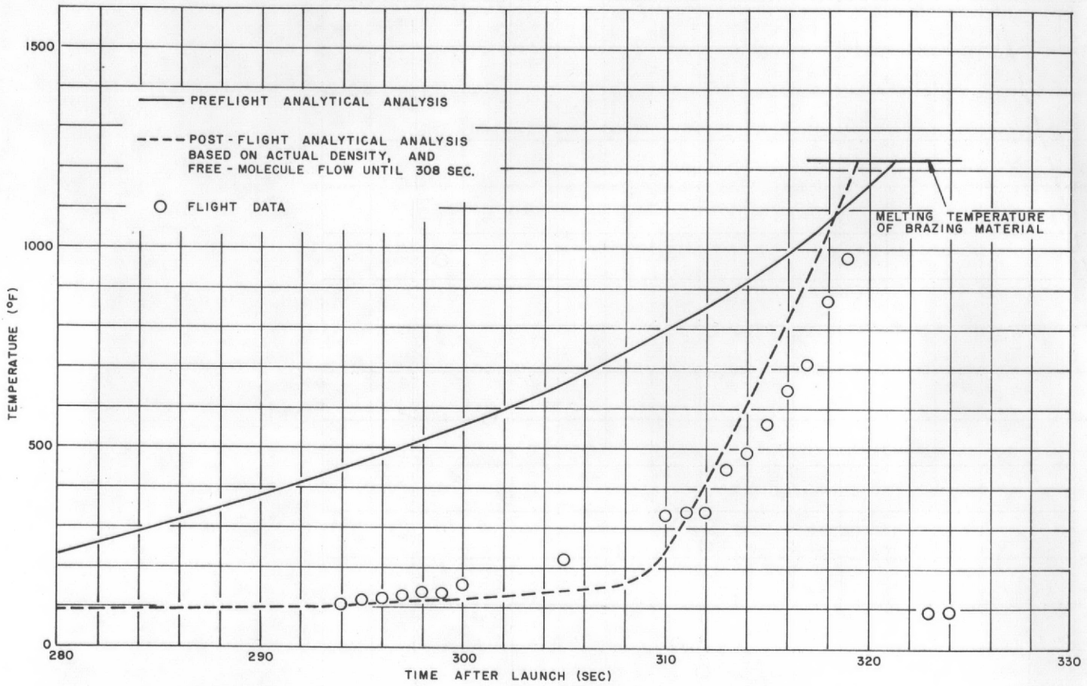

Figure 37. T7 (band joint) temperatures as measured during the RFD-1 flight and as calculated in the preflight and postflight analyses

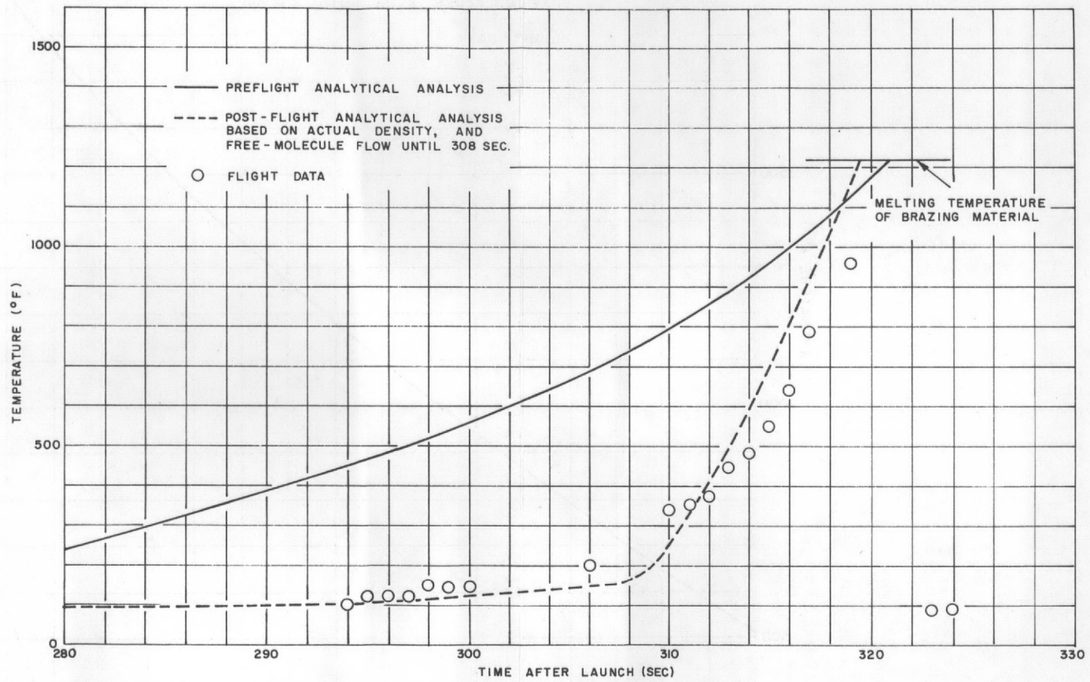

Figure 38. T8 (band joint, opposite T7) temperatures as measured during the RFD-1 flight and as calculated in the preflight and post-flight analyses

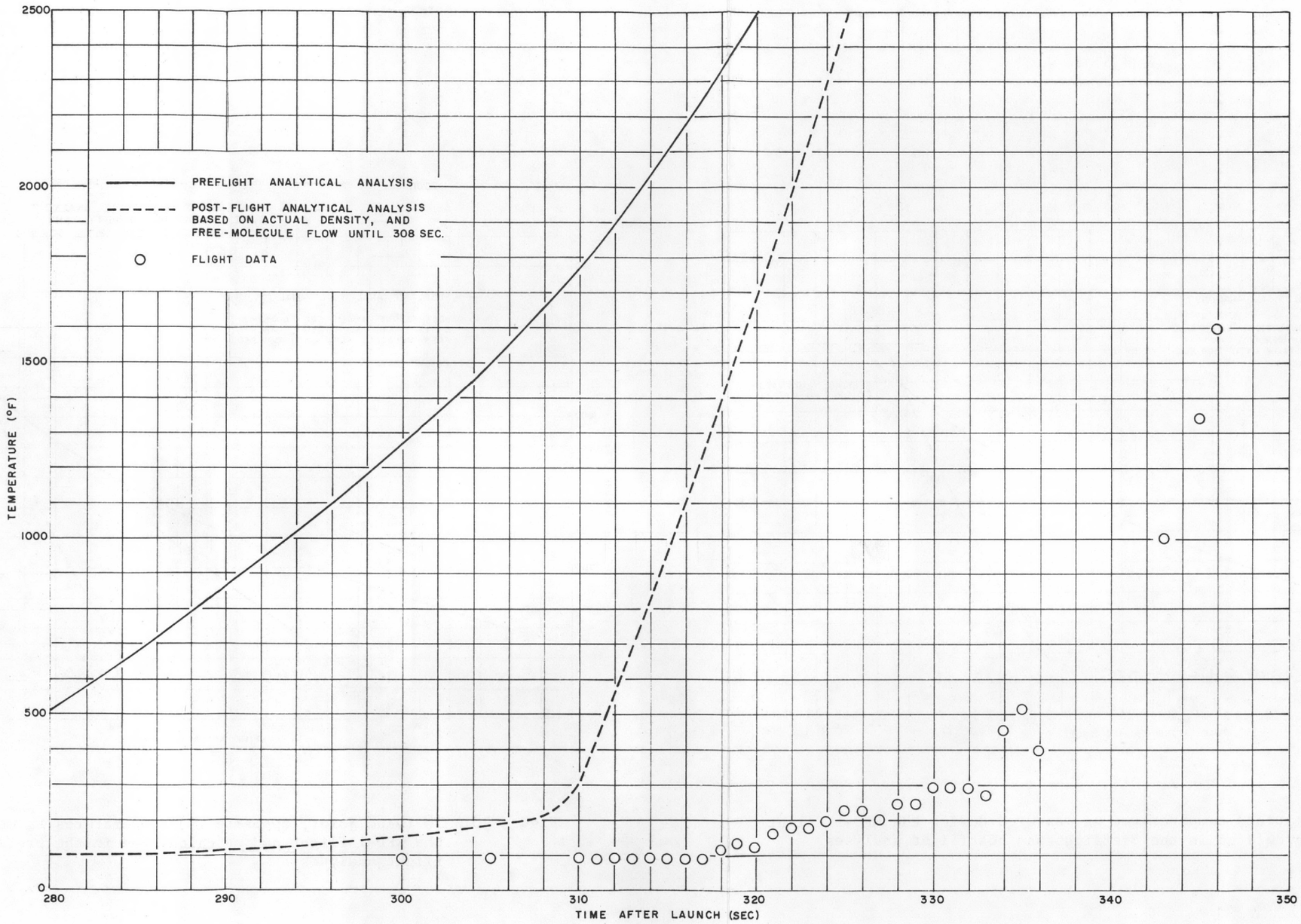

Figure 39. T9 (transverse NaK tube, leading surface) temperatures as measured during the RFD-1 flight and as calculated in the preflight and postflight analyses

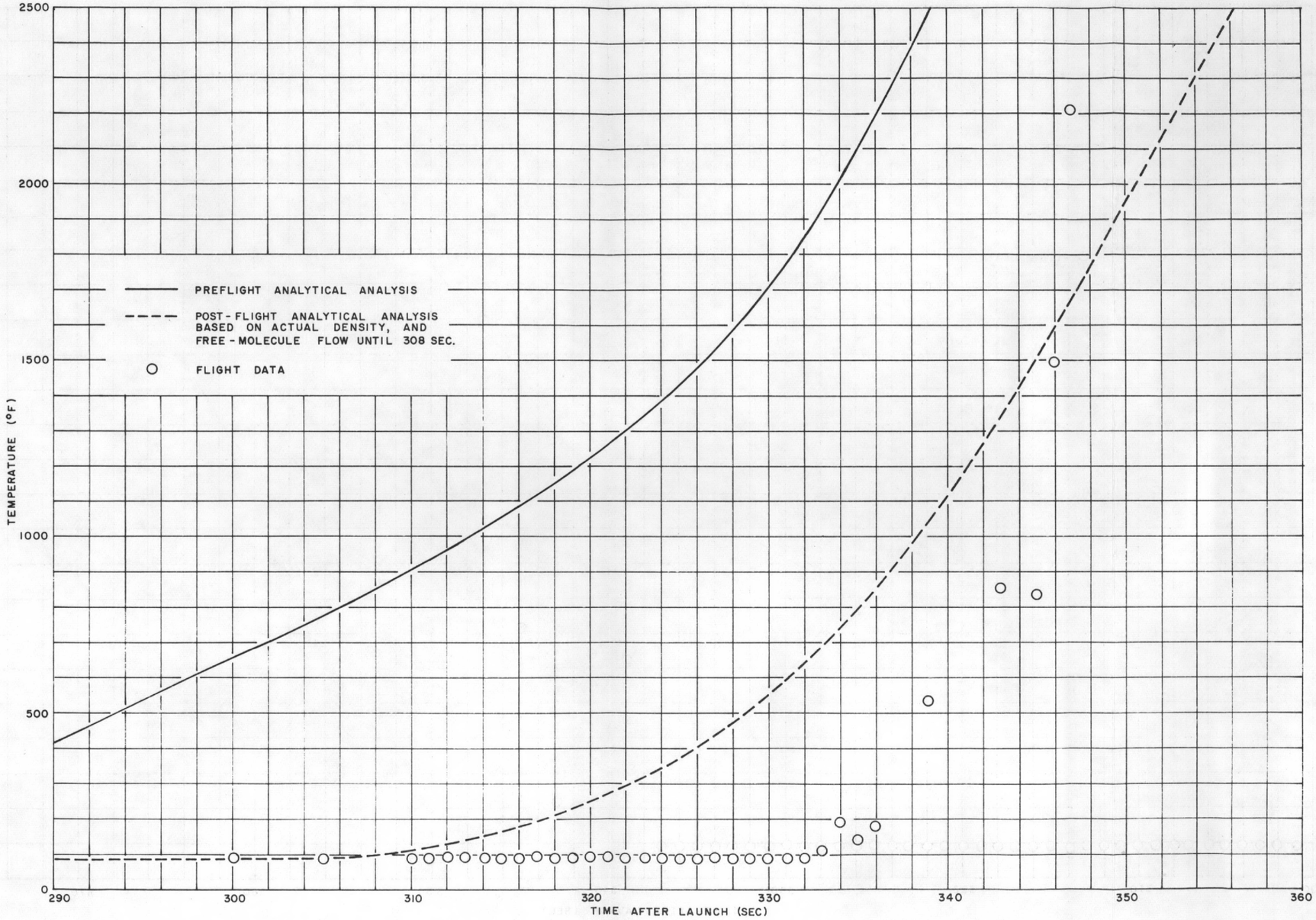

Figure 40. T10 (transverse NaK tube, trailing surface) temperatures as measured during the RFD-1 flight and as calculated in the preflight and postflight analyses

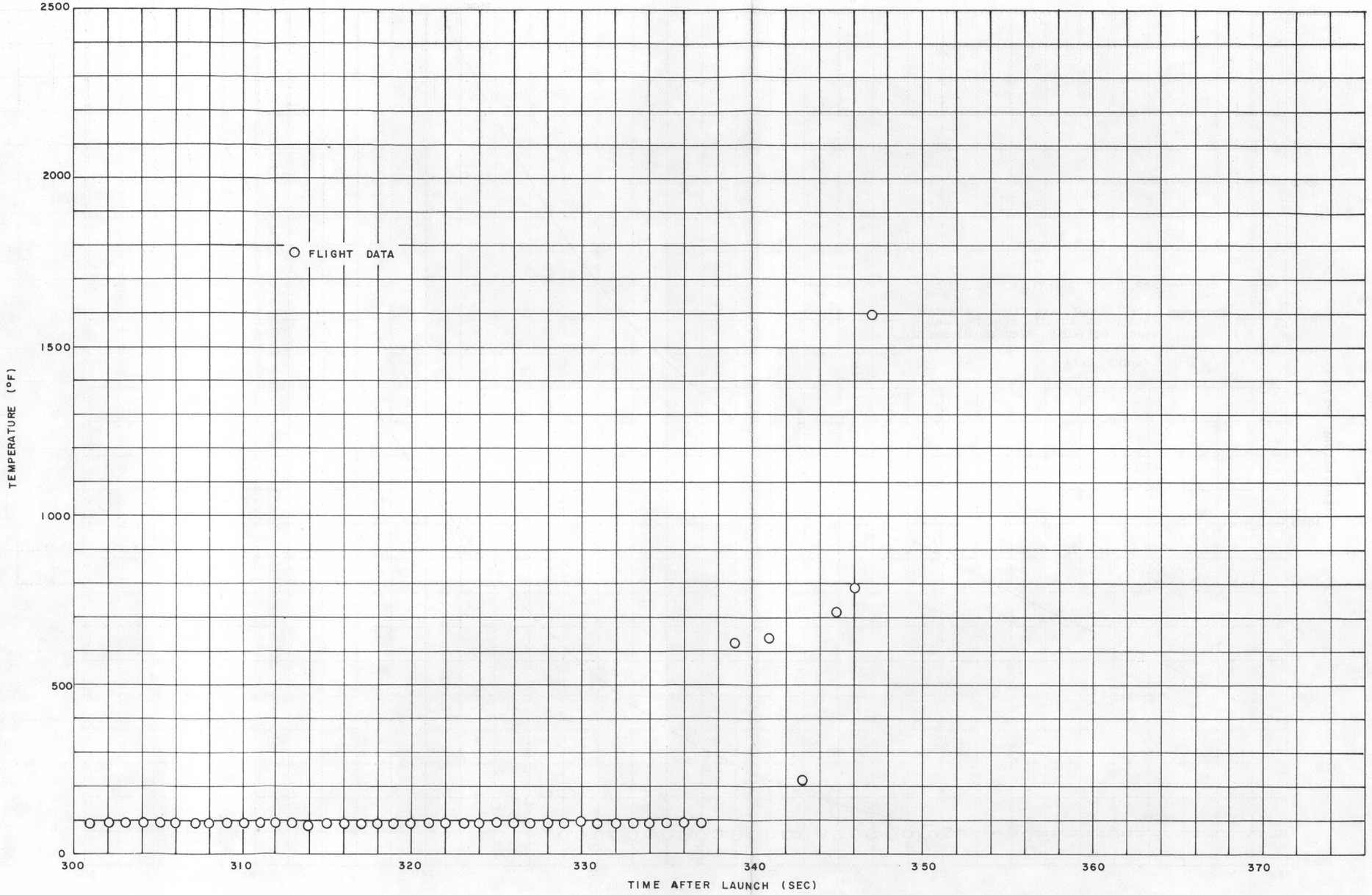

Figure 41. T11 (base of NaK pump) temperatures as measured during the RFD-1 flight

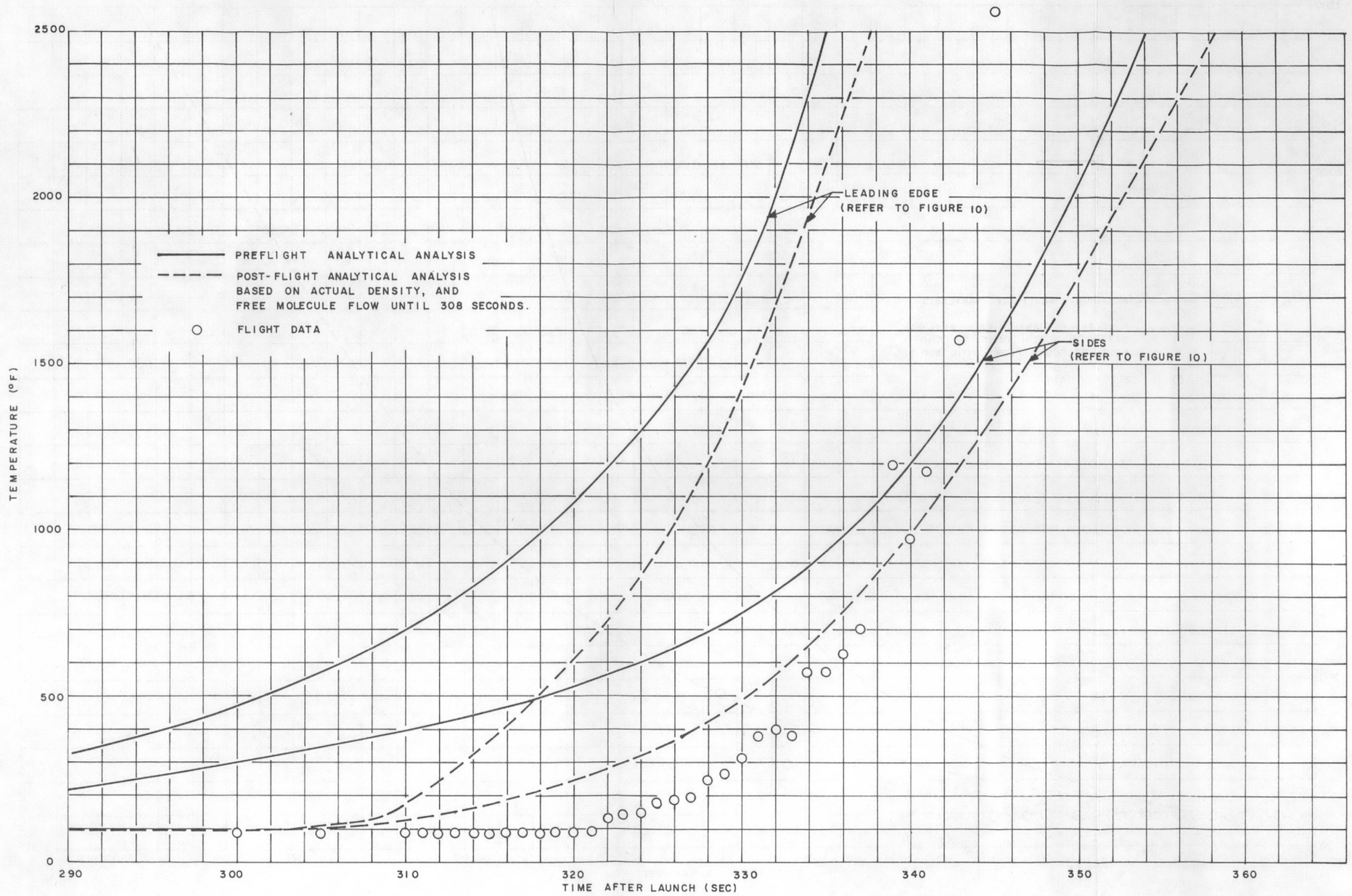

Figure 42. T12 (NaK fill tube) temperatures as measured during the RFD-1 flight and as calculated in the preflight and postflight analyses

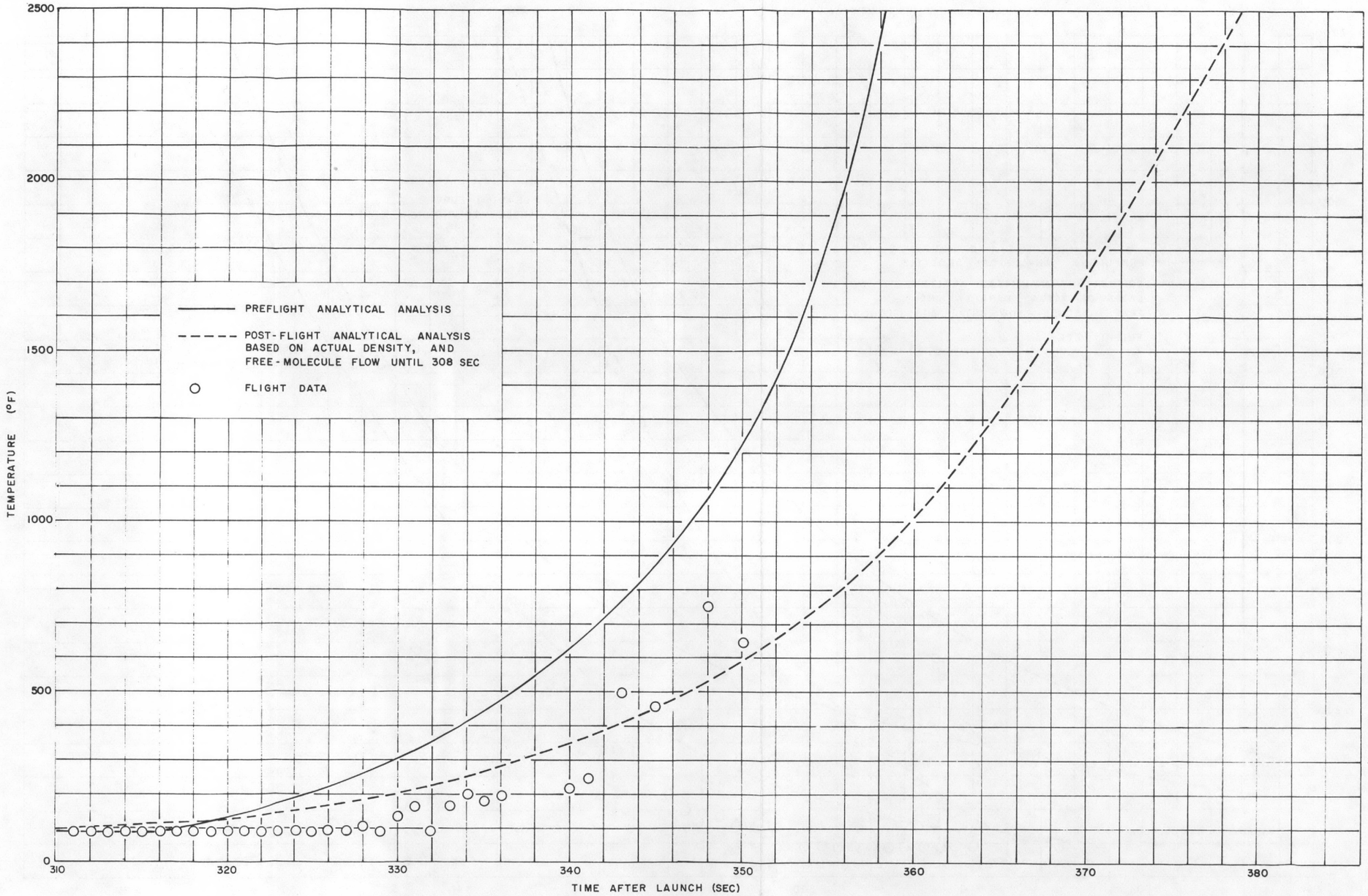

Figure 43. T13 (lip weld behind NaK tube) temperatures as measured during the RFD-1 flight and as calculated in the preflight and postflight analyses

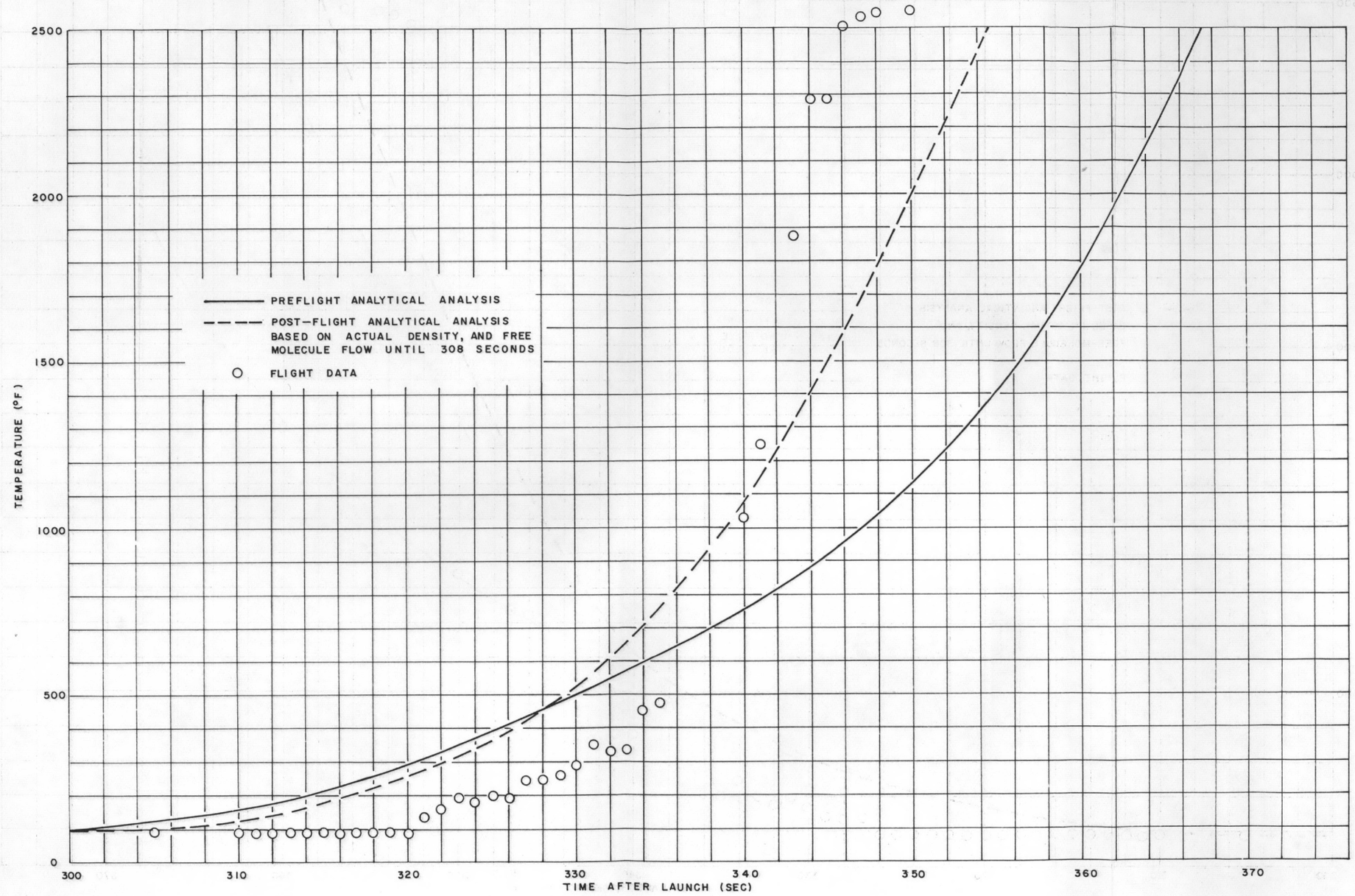

Figure 44. T14 (lip weld, unobstructed flow) temperatures as measured during the RFD-1 flight and as calculated in the preflight and postflight analyses

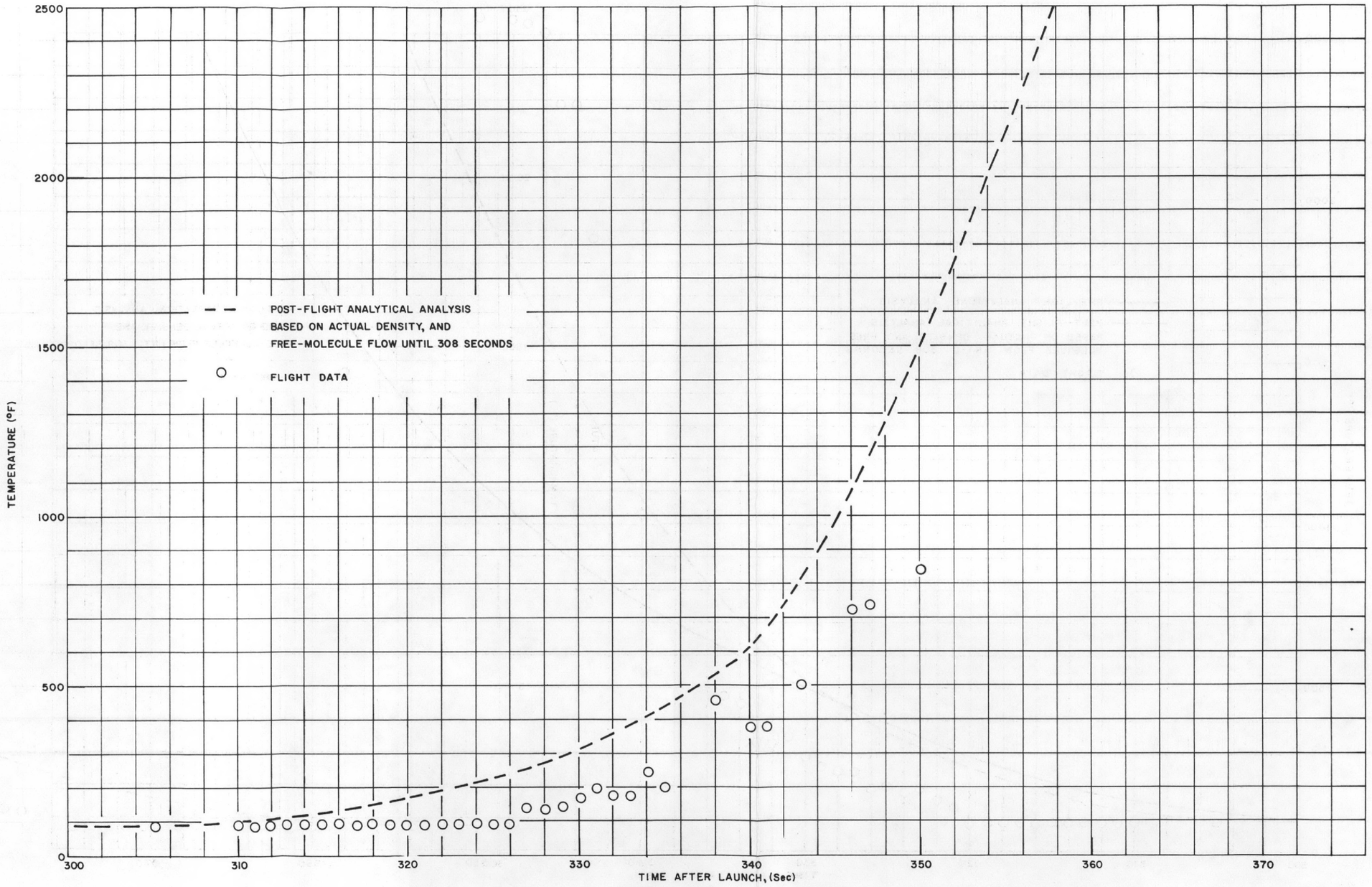

Figure 45. T15 (lip weld, behind fin) temperatures as measured during the RFD-1 flight and as calculated in the postflight analysis

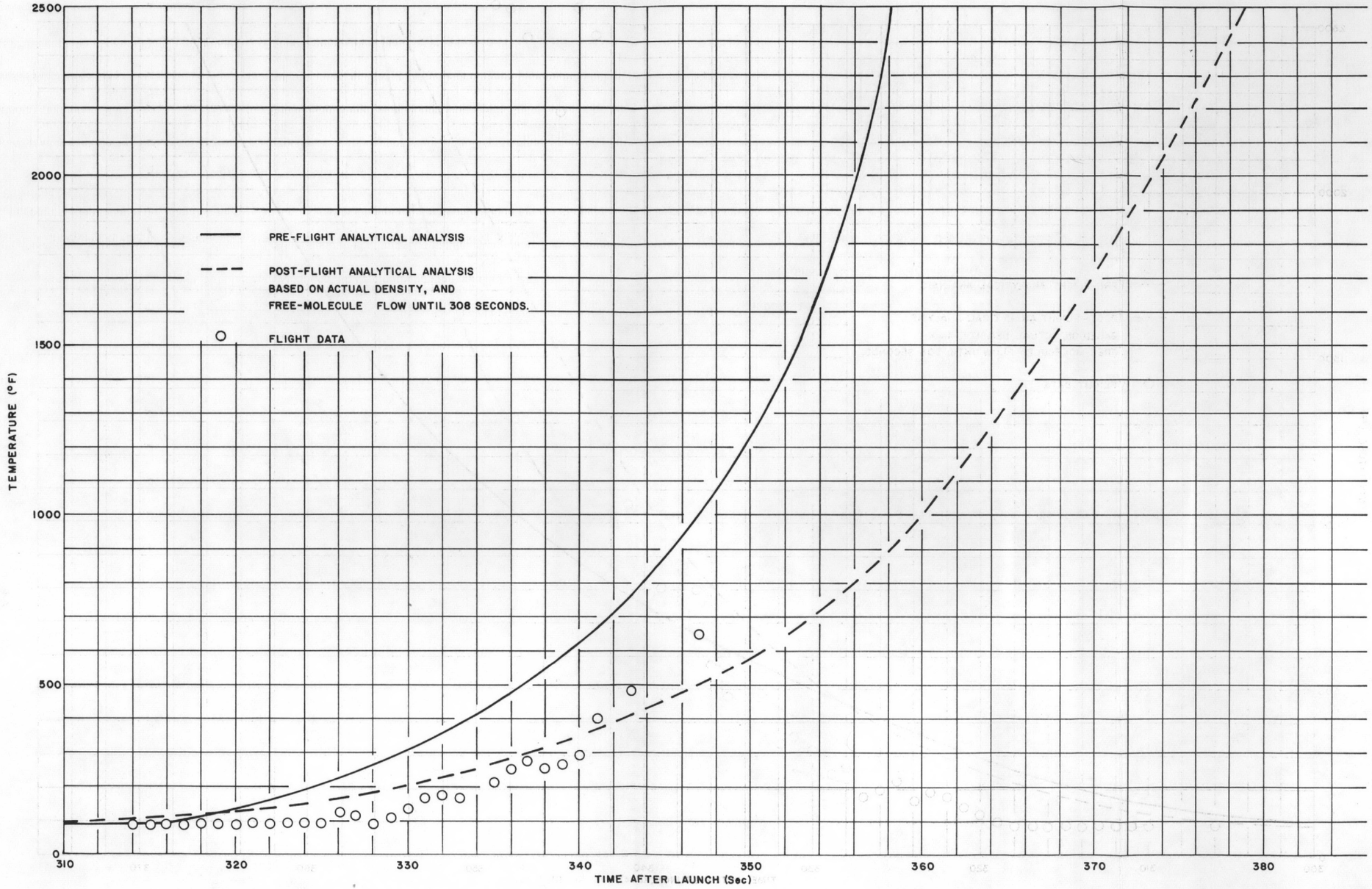

Figure 46. T16 (lip weld, behind NaK tube, opposite T13) temperatures as measured during the RFD-1 flight and as calculated in the preflight and postflight analyses

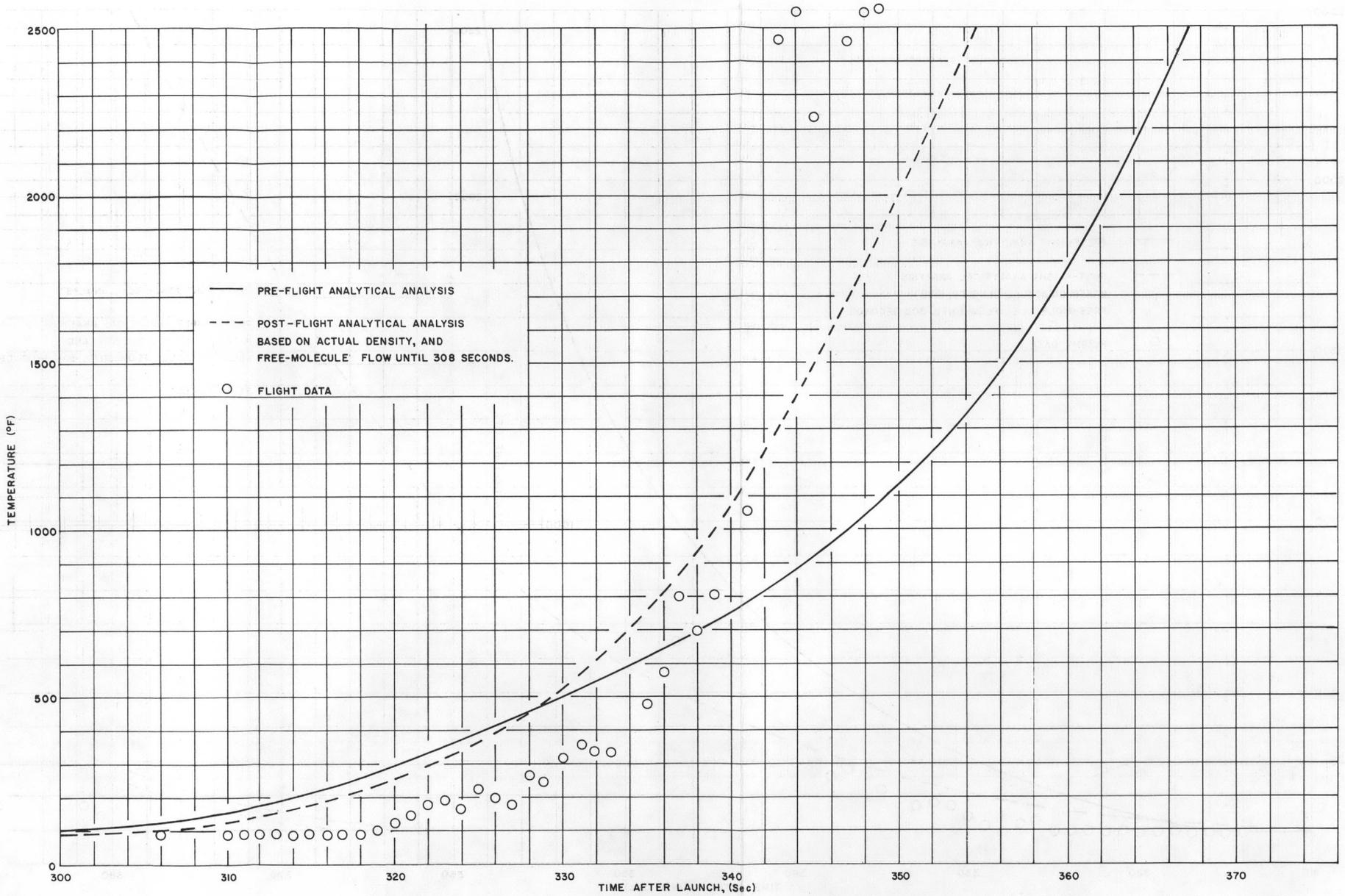

Figure 47. T17 (lip weld, unobstructed flow, opposite T14) temperatures as measured during the RFD-1 flight and as calculated in the preflight and postflight analyses

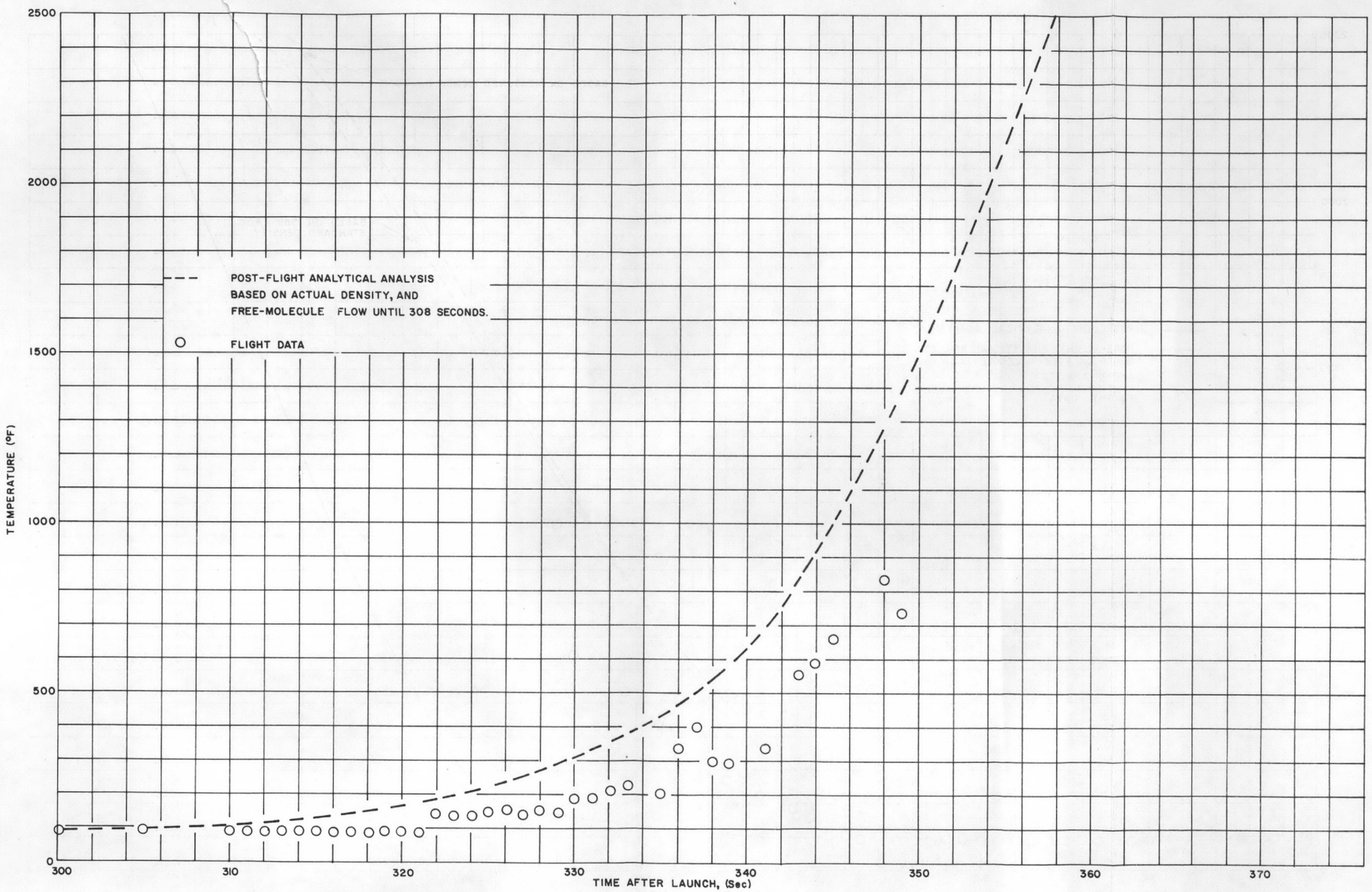

Figure 48. T18 (lip weld, behind fin, opposite T15) temperatures as measured during the RFD-1 flight and as calculated in the postflight analysis

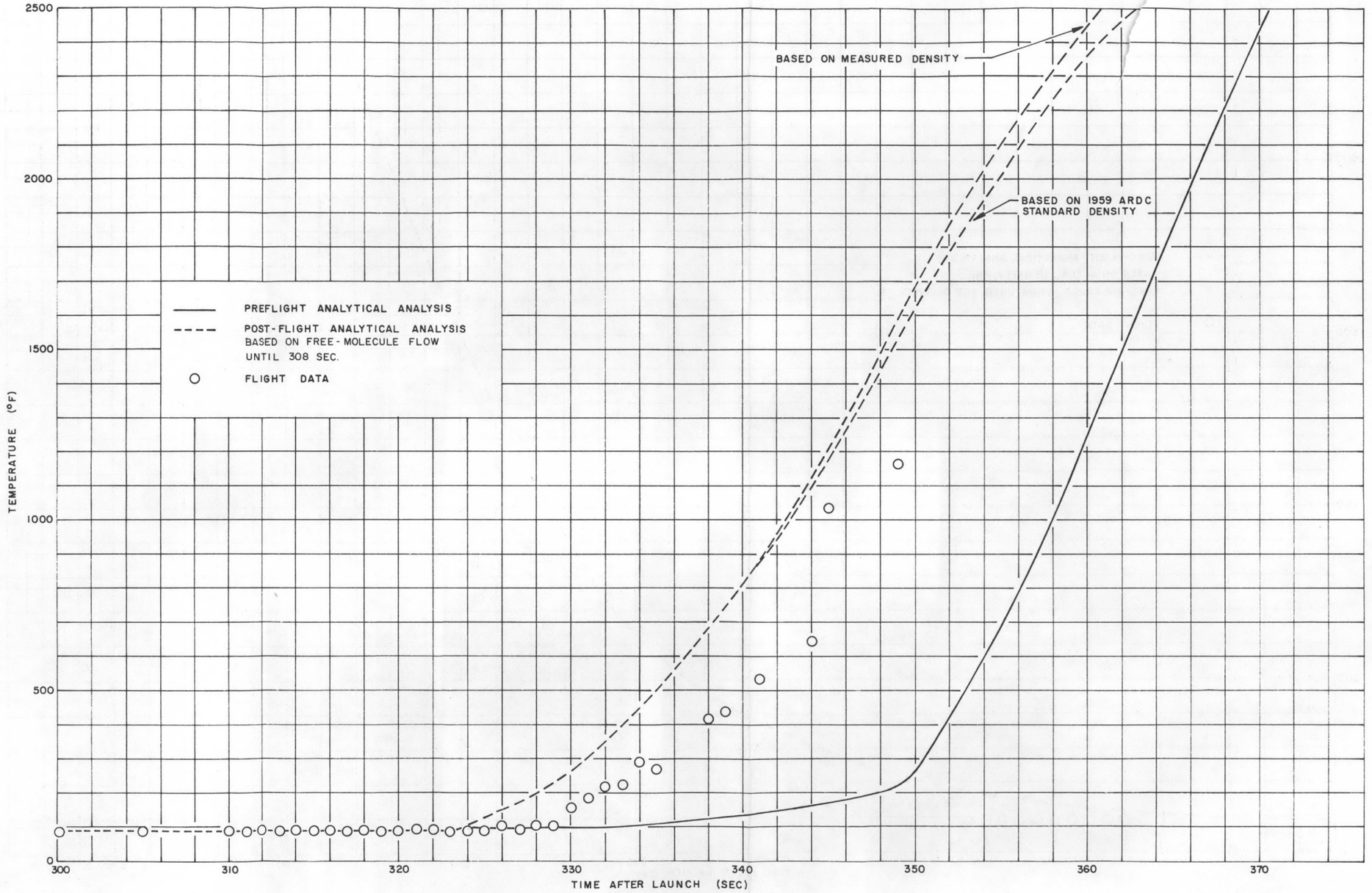

Figure 49. T19 (core-vessel wall) temperatures as measured during the RFD-1 flight and as calculated in the preflight and postflight analyses

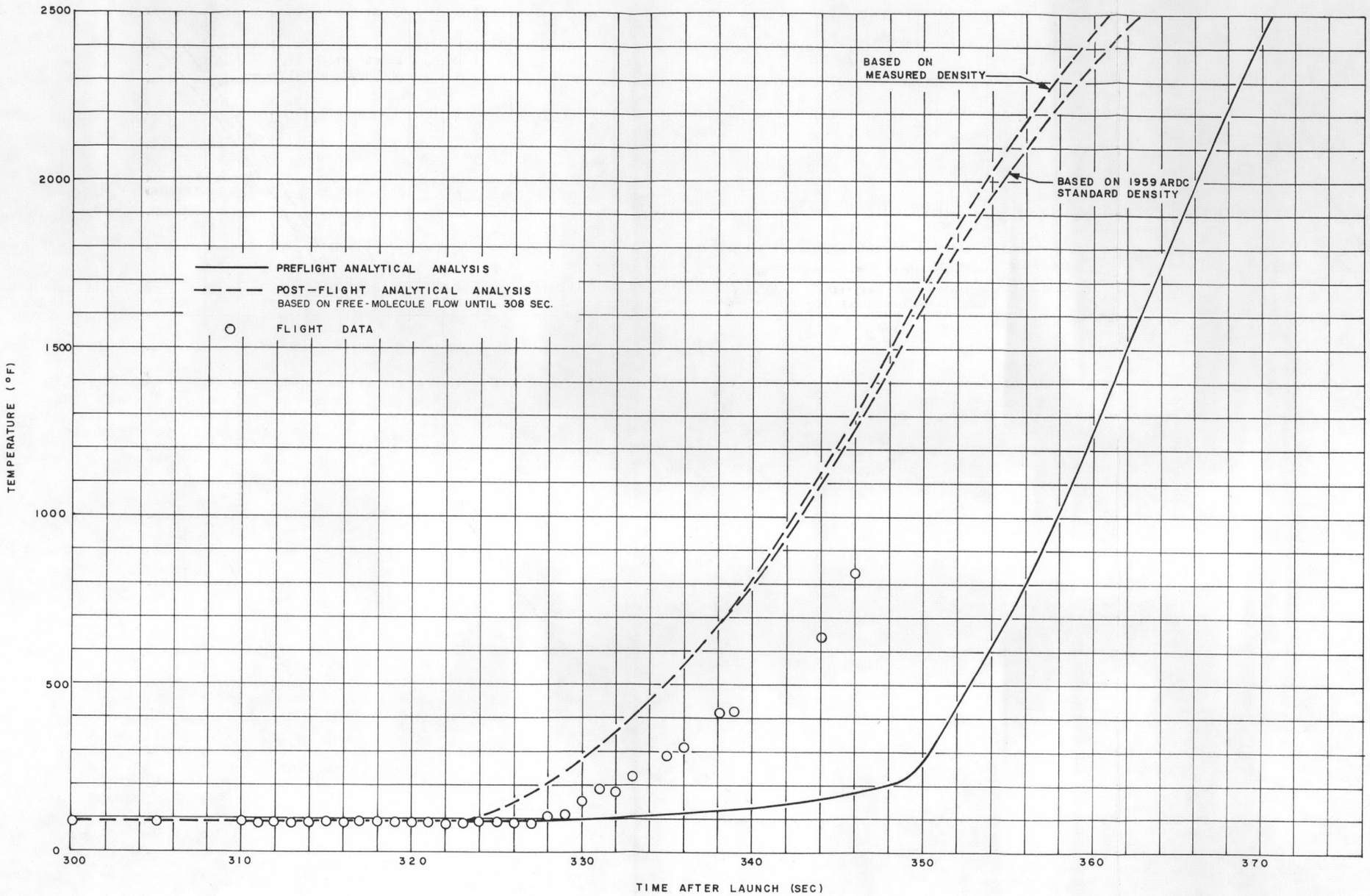

Figure 50. T20 (core-vessel wall, opposite T19) temperatures as measured during the RFD-1 flight and as calculated in the preflight and postflight analyses

Calculations for aerodynamic heating above 310,000 feet (occurring before 308 seconds in the trajectory) were based on the theory of Oppenheim[1] for free-molecule flow. However, integrated heating in the free-molecule region is relatively small, and thus has a negligible effect on reactor disassembly.

Aerodynamic heating below 310,000 feet was based on experimentally determined ratios of local to stagnation-point heating (see Appendices A and B). Calculation of the postflight stagnation-point heating curve was essentially the same as in the preflight analysis, except that the input data were obtained from the radar-measured trajectory (No. 635) and the air density as measured by sounding rockets. See Table VI for Trajectory 635 and Figure 51 for ballistic coefficient versus time. Figure 52 shows the sequence of events from launch. For a discussion of density measurement and Trajectory 635, see SC-RR-64-517 and SC-RR-64-510. Heating ratios measured at Rhodes and Bloxsom were used to calculate the temperature history of the core-vessel wall and the lip weld. AEDC data were used for all other locations on the reactor except the band joint and NaK fill tube, for which the parameters were calculated by Sandia. Table VII lists values of heating ratios used.

Analysis of reactor burnup based on measured density is not appreciably different from the same analysis based on 1959 ARDC standard atmosphere. The difference in stagnation-point heating can be seen in Figure 53. The larger differences in stagnation-point heating are seen to occur later in the heat pulse, and do not therefore affect to a large extent the time at which the reactor will disassemble. The time difference at which the core-vessel walls are predicted to reach melting temperature based on measured density compared to ARDC standard atmosphere can be seen in Figures 49 and 50. In the analysis based on actual density, the core-vessel walls reach melting temperature about 2 seconds before they do in the analysis based on ARDC standard atmosphere.

Table VIII lists the altitudes at which burnup of certain components occurred during the RFD-1 flight. Above 200,000 feet, these represent actual measured values from telemetered data. Below 200,000 feet, the telemetered data were extrapolated to the melting point, using the same analytical methods discussed previously.

Heat losses from the reactor surfaces through thermal radiation were calculated assuming emissivity as a function of temperature only. It would be desirable to have emissivity as a function of temperature for the exact surface condition of the material used in the reactor for a more accurate analysis of radiation loss. In the case of RFD-1, which had a high peak heating over a short period of time, the effect of radiation was to delay attainment of melting temperature by only a few seconds. However, if an orbital-decay trajectory is considered, radiation losses become much greater and it would be desirable to use more accurate values of emissivities in analytical predictions.

TABLE VI

Trajectory 635

Key:

Time - Time from launch, in seconds.
Altitude - Feet above mean sea level.
Latitude - The geodetic latitude, in degrees, of the intersection of a line from the re-entry system perpendicular to the rotating oblate earth.
Longitude - The longitude, in degrees, of the intersection of a line from the re-entry system perpendicular to the surface of the rotating oblate earth.
Velocity - Velocity, in feet per second, relative to the rotating earth.
Re-entry Angle - Relative re-entry angle in degrees; i.e., the angle between the relative velocity and a plane perpendicular to a line from the re-entry system perpendicular to the surface of the earth.
Integrated Heating - Total integrated stagnation-point heating, in BTU/ft$^{1/2}$, on a 1-foot-radius hemisphere re-entering on Trajectory 635.
Heating Rate - Stagnation-point heating, in BTU/ft$^{1/2}$-sec, on a 1-foot radius hemisphere re-entering on Trajectory 635.

Time	Altitude	Latitude	Longitude	Velocity	Re-entry Angle	Heating Rate	Integrated Heating
259.4	416756	34.29	-70.51	19902	- 5.56	.622	.00000
260.0	415597	34.27	-70.48	19904	- 5.58	.632	.37603
262.0	411704	34.19	-70.39	19910	- 5.64	.664	1.6717
264.0	407769	34.12	-70.29	19916	- 5.70	.703	3.0350
266.0	403791	34.05	-70.20	19922	- 5.76	.746	4.4829
268.0	399770	33.98	-70.10	19928	- 5.82	.788	6.0170
270.0	395706	33.90	-70.01	19935	- 5.88	.848	7.6501
272.0	391599	33.83	-69.92	19941	- 5.94	.904	9.4023
274.0	387449	33.76	-69.82	19947	- 6.00	.977	11.281
276.0	383256	33.68	-69.73	19954	- 6.06	1.06	13.313
278.0	379020	33.61	-69.64	19961	- 6.12	1.14	15.514
280.0	374741	33.54	-69.54	19967	- 6.18	1.26	17.917
282.0	370420	33.47	-69.45	19974	- 6.24	1.37	20.558
282.0	370420	33.47	-69.45	19974	- 6.24	1.37	20.558
283.0	368243	33.43	-69.40	19977	- 6.27	1.46	21.977
284.0	366055	33.39	-69.35	19981	- 6.30	1.56	23.489
286.0	361648	33.32	-69.26	19988	- 6.36	1.73	26.782
288.0	357198	33.24	-69.17	19994	- 6.42	2.00	30.498
290.0	352704	33.17	-69.08	20001	- 6.48	2.30	34.789
292.0	348168	33.10	-68.98	20008	- 6.54	2.60	39.685
294.0	343589	33.02	-68.89	20016	- 6.60	2.94	45.223
296.0	338967	32.95	-68.80	20023	- 6.66	3.30	51.456
298.0	334302	32.87	-68.71	20030	- 6.72	3.78	58.511
300.0	329594	32.80	-68.61	20037	- 6.78	4.24	66.539
302.0	324843	32.73	-68.52	20045	- 6.84	4.95	75.693
304.0	320050	32.65	-68.43	20052	- 6.90	5.58	86.235
306.0	315213	32.58	-68.34	20059	- 6.96	6.62	98.365
308.0	310334	32.50	-68.25	20067	- 7.01	7.54	112.55
310.0	305411	32.43	-68.15	20075	- 7.07	9.08	129.07
312.0	300446	32.35	-68.06	20082	- 7.13	10.5	148.64
314.0	295438	32.28	-67.97	20090	- 7.19	12.5	171.46

TABLE VI (cont)

Time	Altitude	Latitude	Longitude	Velocity	Re-entry Angle	Heating Rate	Integrated Heating
316.0	290387	32.20	-67.88	20097	- 7.25	14.3	198.22
318.0	285293	32.13	-67.79	20105	- 7.31	17.0	229.36
320.0	280156	32.05	-67.70	20112	- 7.37	19.5	265.95
322.0	274977	31.98	-67.61	20119	- 7.43	23.4	308.61
322.0	274977	31.98	-67.61	20119	- 7.43	23.4	308.61
323.0	272371	31.94	-67.56	20123	- 7.46	25.1	332.87
324.0	269755	31.90	-67.52	20126	- 7.49	26.9	358.89
326.0	264490	31.82	-67.43	20133	- 7.54	32.0	417.86
328.0	259183	31.75	-67.34	20139	- 7.60	36.8	486.76
330.0	253833	31.67	-67.24	20144	- 7.66	42.5	565.87
332.0	248441	31.60	-67.15	20149	- 7.72	48.2	656.56
334.0	243008	31.52	-67.06	20153	- 7.78	54.9	759.54
336.0	237532	31.44	-66.97	20156	- 7.84	62.1	876.48
338.0	232016	31.37	-66.88	20158	- 7.89	69.9	1008.4
340.0	226458	31.29	-66.79	20158	- 7.95	78.7	1156.8
342.0	220859	31.21	-66.70	20157	- 8.01	87.6	1323.1
344.0	215221	31.14	-66.62	20153	- 8.07	98.3	1508.8
346.0	209543	31.06	-66.53	20146	- 8.13	109.	1715.9
348.0	203826	30.98	-66.44	20136	- 8.19	121.	1945.3
350.0	198071	30.91	-66.35	20121	- 8.25	133.	2199.8
352.0	192281	30.83	-66.26	20102	- 8.31	147.	2479.5
353.0	189372	30.79	-66.22	20090	- 8.34	154.	2629.8
354.0	186455	30.75	-66.17	20076	- 8.37	161.	2787.3
354.0	186445	30.75	-66.17	20076	- 8.37	161.	2787.3
356.0	180596	30.68	-66.08	20041	- 8.43	176.	3124.6
358.0	174707	30.60	-65.99	19998	- 8.49	192.	3493.0
360.0	168790	30.52	-65.91	19942	- 8.55	212.	3897.1
362.0	162848	30.45	-65.82	19872	- 8.61	234.	4343.2
364.0	156887	30.37	-65.73	19783	- 8.68	257.	4833.9
366.0	150912	30.29	-65.65	19671	- 8.74	283.	5373.4
368.0	144931	30.22	-65.56	19527	- 8.81	312.	5967.9
370.0	138954	30.14	-65.48	19342	- 8.88	343.	6621.9
372.0	132994	30.07	-65.39	19106	- 8.95	374.	7338.7
374.0	127068	30.00	-65.31	18805	- 9.03	404.	8117.0
376.0	121196	29.92	-65.23	18426	- 9.11	431.	8952.4
378.0	115405	29.85	-65.15	17952	- 9.20	451.	9835.2
380.0	109725	29.79	-65.08	17363	- 9.30	462.	10750.
382.0	104196	29.72	-65.00	16635	- 9.41	460.	11675.
384.0	98862.	29.66	-64.93	15757	- 9.53	441.	12580.
384.0	98862.	29.66	-64.93	15757	- 9.53	441.	12580.
386.0	93779.	29.60	-64.87	14665	- 9.68	398.	13424.
386.0	93779.	29.60	-64.87	14665	- 9.68	398.	13424.
388.0	89023.	29.54	-64.81	13376	- 9.85	336.	14160.
390.0	84633.	29.49	-64.75	12033	-10.1	268.	14764.
392.0	80621.	29.45	-64.70	10691	-10.3	204.	15237.
392.1	80383.	29.45	-64.70	10609	-10.3	200.	15262.

End of run.

TABLE VII

Heating Ratios Used for Burnup Calculations

Thermocouple No.	Location of Thermocouple	Heating Ratios for Times and Locations Indicated For Ratio q_L/q_s		
		Time < 308 sec		Time > 308 sec
3	Fin, center	Leading edge = 1 Sides = .11		Leading edge = 5 Sides = .11
4	Fin, trailing, outer	Leading edge = 1 Sides =.11		Leading edge = 5 Sides = .11
5	Fin, center (opposite T3)	Leading edge = 1 Sides = .11		Leading edge = 5 Sides = .11
7, 8	Band joint	Leading edge = 1 Sides = .12		Leading edge = 12.1 Sides = 2.68
9	Transverse NaK tube, leading surface	1		3.6
10	Transverse NaK tube, trailing surface	0		0.3
12	NaK fill tube	Leading edge = 1 Sides = .12		Leading edge = 6 Sides = .2
14, 17	Lip weld in unobstructed flow	Leading edge = 1 Sides = .12		Leading edge = 4 Sides = .62
		Time < 308 sec	Time 308-340 sec	Time > 340 sec
15, 18	Lip weld behind fin	Leading edge = 0 Sides = 0	Leading edge = 1.1 Sides = .37	Leading edge = 4 Sides = .62
		Time < 308 sec	Time 308-354 sec	Time > 354 sec
13, 16	Lip weld behind NaK tube	Leading edge = 0 Sides = 0	Leading edge = .37 Sides = .19	Leading edge = .82 Sides = .19
		Time < 323 sec		Time > 323 sec
19, 20	Core-vessel wall	0		.17

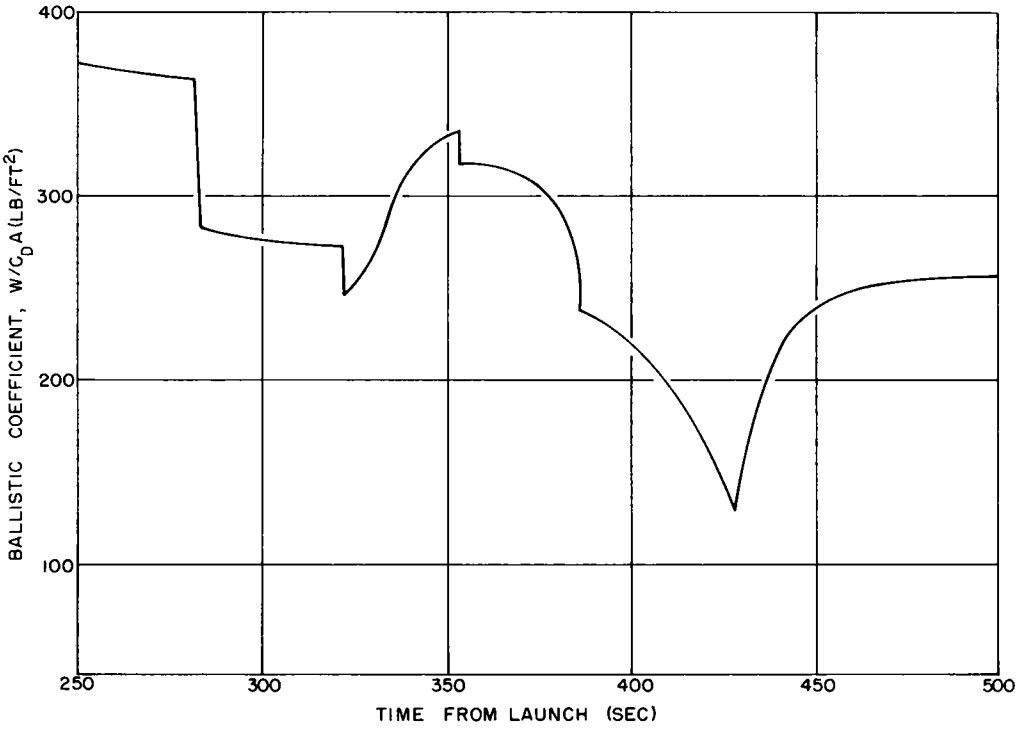

Figure 51. Ballistic coefficients versus time used in calculating Trajectory 635

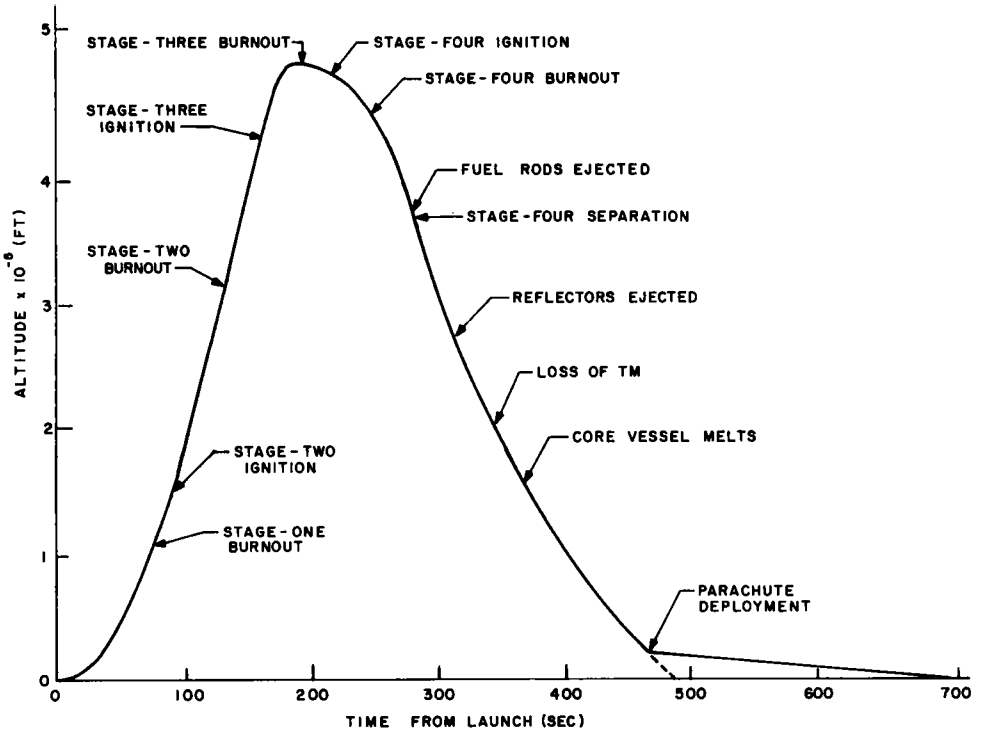

Figure 52. Sequence of events from launch

TABLE VIII

Flight-Test Altitudes for Stages of Reactor Disassembly

Event	Time from launch (sec)	Altitude (ft)
Reflectors ejected	323	272,000
Pump fins melted	340	226,000
Transverse NaK tube melted	350	198,000
Lip weld melted in regions of unobstructed flow	350	198,000
Core-vessel walls melted	361	166,000

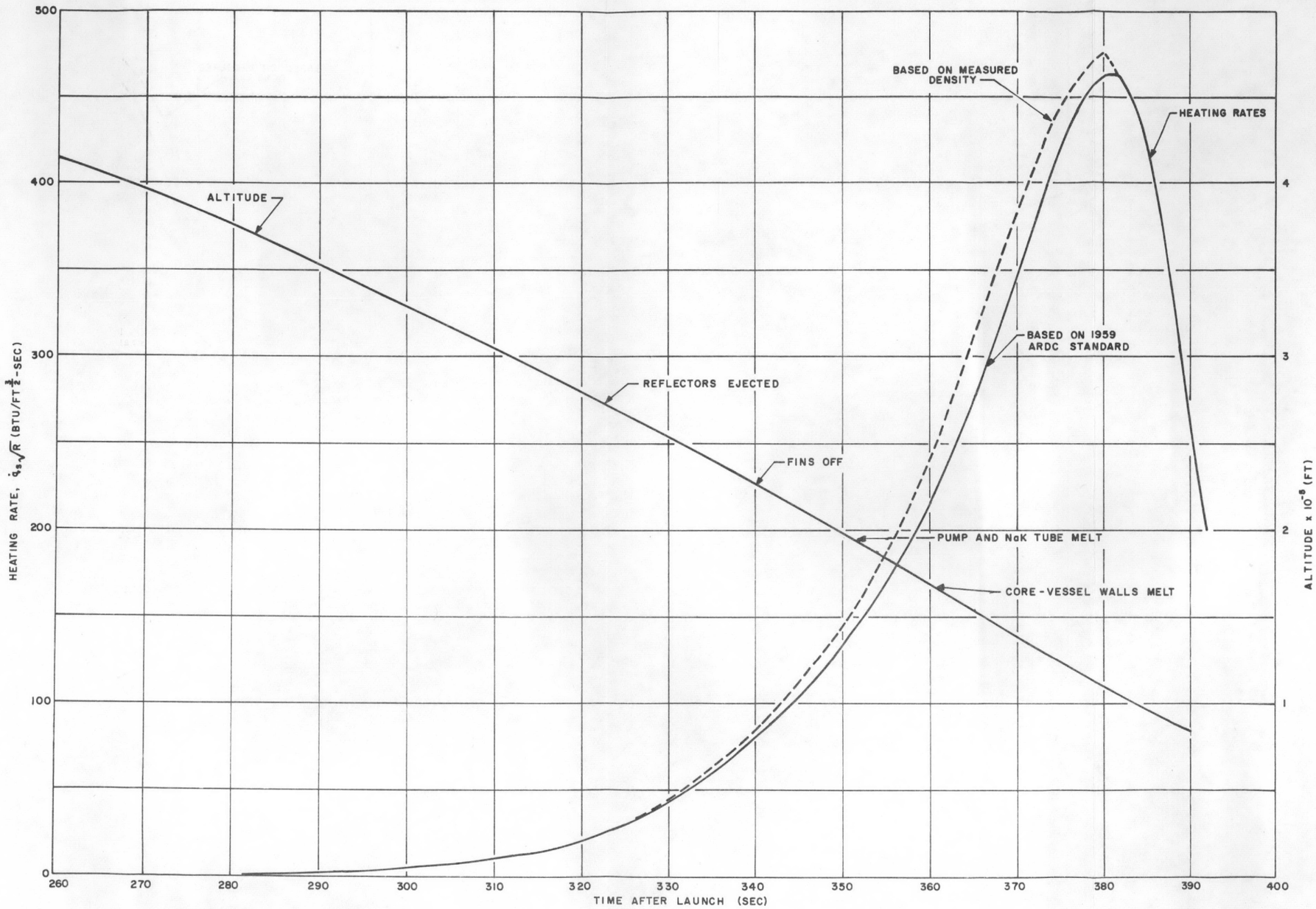

Figure 53. Stagnation heating for a 1-foot-radius hemisphere: a comparison of calculations based on the 1959 ARDC standard atmosphere versus calculations based on measured density; and reactor-disassembly events versus time and altitude

Optical Data

Motion pictures taken by NASA from aircraft located close to the end of the RFD-1 trajectory show objects following along behind the RV during re-entry at two different times. Blown-up frames from the black-and-white, 35-mm NASA movie are shown in Figures 54, 55, 56, 57, and 58. The apparently upward path of the re-entry trajectory in these pictures is due to the orientation of the NASA aircraft with respect to the RV. The first group of objects, believed to be the pump, NaK tube, and core-vessel lid, becomes visible at about 354 seconds (Figures 54 and 55). At 365 seconds, several objects are again visible behind the RV (Figures 56, 57, and 58); these are believed to be the core-vessel walls breaking up.

Figure 59 is a chopped plate-camera picture taken from Bermuda, showing the RV during re-entry. The sequence of events and the times from launch are marked on the photograph. It should be noted that relative brightness does not necessarily mean more intense burning, since the RV was not at a constant distance from the camera. Figure 60 shows the position of Bermuda relative to the trajectory. For a detailed discussion of the various types of cam coverage and the location of cameras relative to the RV, see SC-RR-64-516.

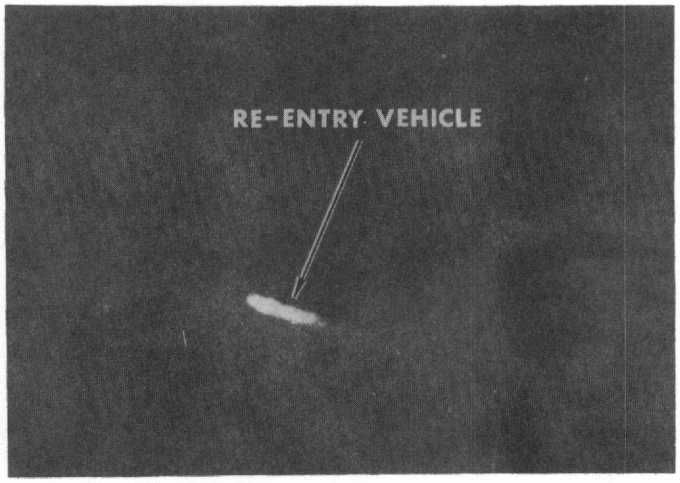

Figure 54.

RFD-1 re-entry at 354.0 seconds, showing RV

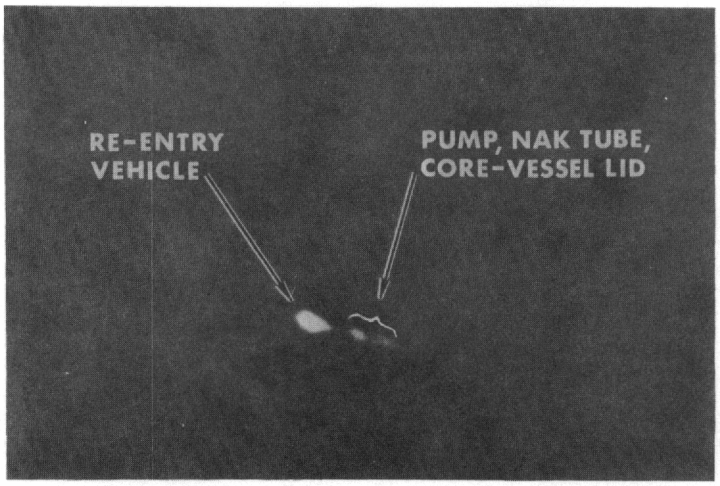

Figure 55.

RFD-1 re-entry at 354.9 seconds, showing RV and objects believed to be the NaK pump, NaK tube, and core-vessel lid

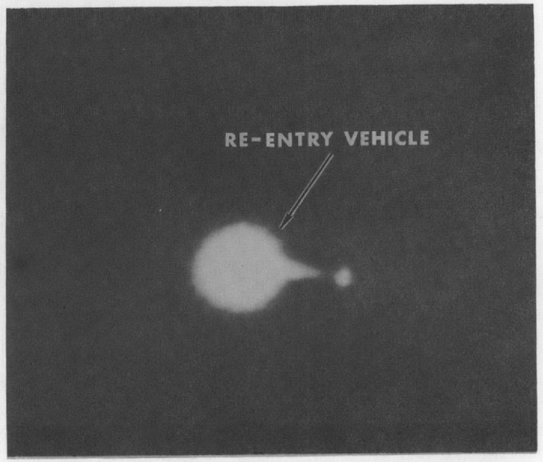

Figure 56. RFD-1 re-entry at 364.6 seconds, showing RV

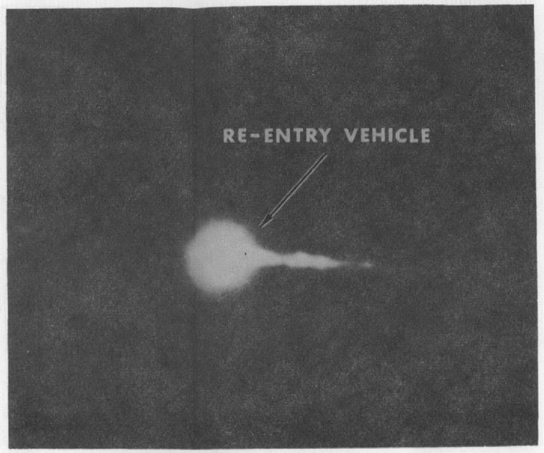

Figure 57. RFD-1 re-entry at 365.8 seconds showing RV

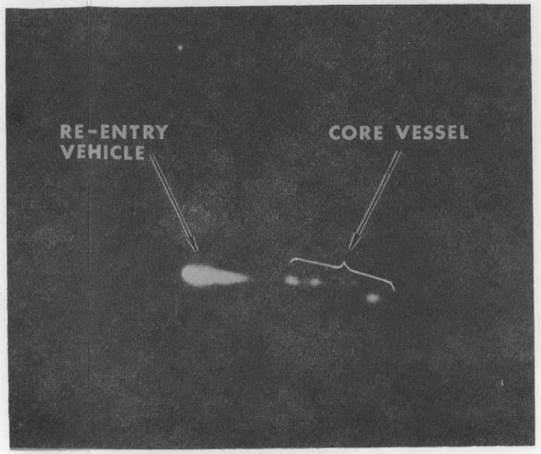

Figure 58. RFD-1 re-entry at 366.9 seconds, showing RV and objects believed to be parts of the core-vessel walls

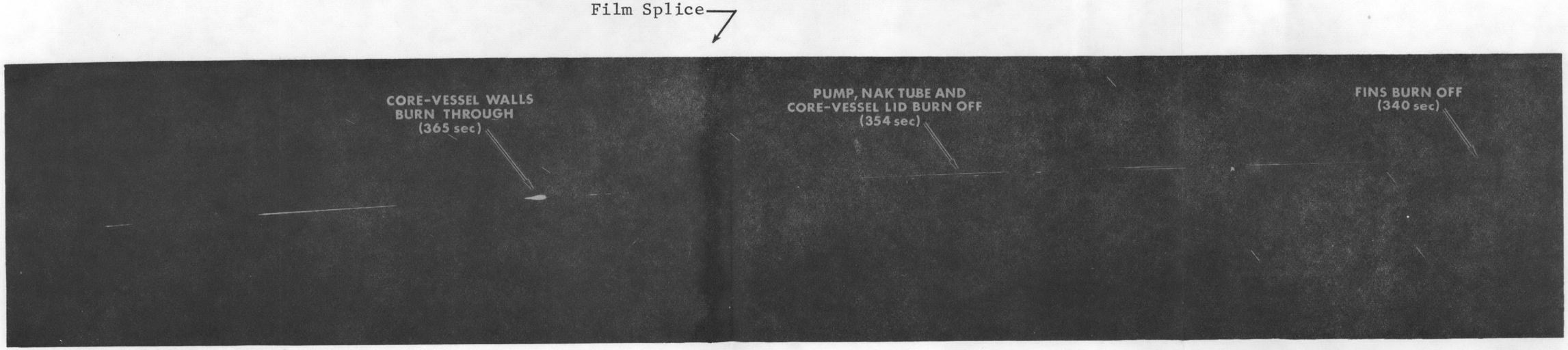

Figure 59. Chopped plate-camera picture showing reactor-disassembly events

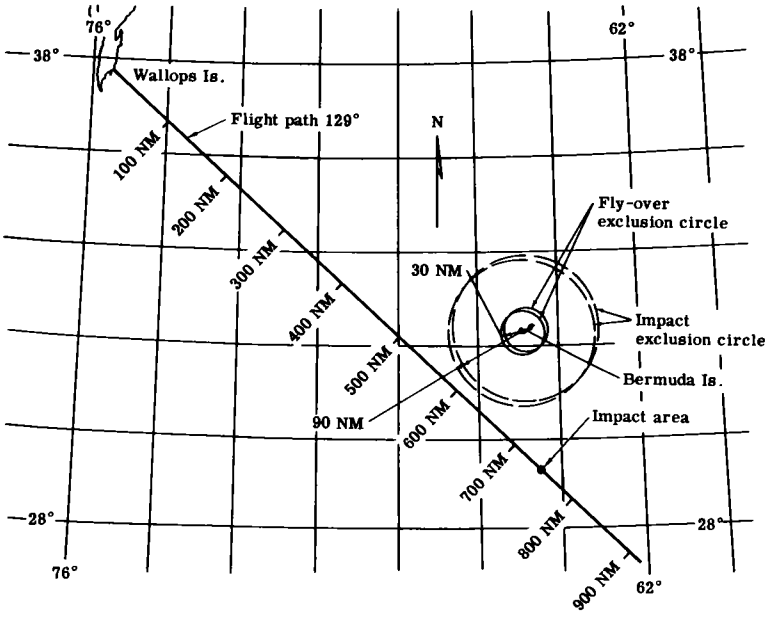

Figure 60. RFD-1 flight path

Telemetry Data

Thermocouple data (Figures 31 through 50) were good until blackout at 350 seconds. All 20 thermocouples in the reactor operated, but some of the data were very scattered.

T1 and T2 were located in the band supports on the reflectors. When the reflectors were ejected, at 323 seconds, the lead wires to T1 and T2 were disconnected, so data after this event should be disregarded for these two locations.

T7 and T8 were located in the band joints, which are welded lap joints in a thin steel band that holds the reflectors on. When the band joints melted, the reflectors were ejected. Thermocouple data for the band joints were very good, showing a definite break at 323 seconds. Reflector ejection at 323 seconds was verified by signals received from switches at the base of the reflectors and between the reflectors and the core-vessel wall. There was also a decrease in roll rate at 323 seconds (Figure 61), indicating reflector ejection at this time. Thermocouple readings when the band joint melted were higher than the measured melting temperature of the brazing material, as expected from the results of the test discussed previously.

T3, T4, T5, and T6 were located in the aluminum fins. The data from these thermocouples were also very good, showing temperatures approaching the melting point of aluminum at around 340 seconds. TM for these locations was very noisy after this time.

T9 and T10, located in the forward NaK tube, gave scattered data after 340 seconds. However, there seemed to be a trend toward the melting temperature at around 350 seconds. Local heating in this location depends strongly on angle of attack.

The data from T11, located in the NaK pump, were very scattered, indicating only a trend in temperature rise.

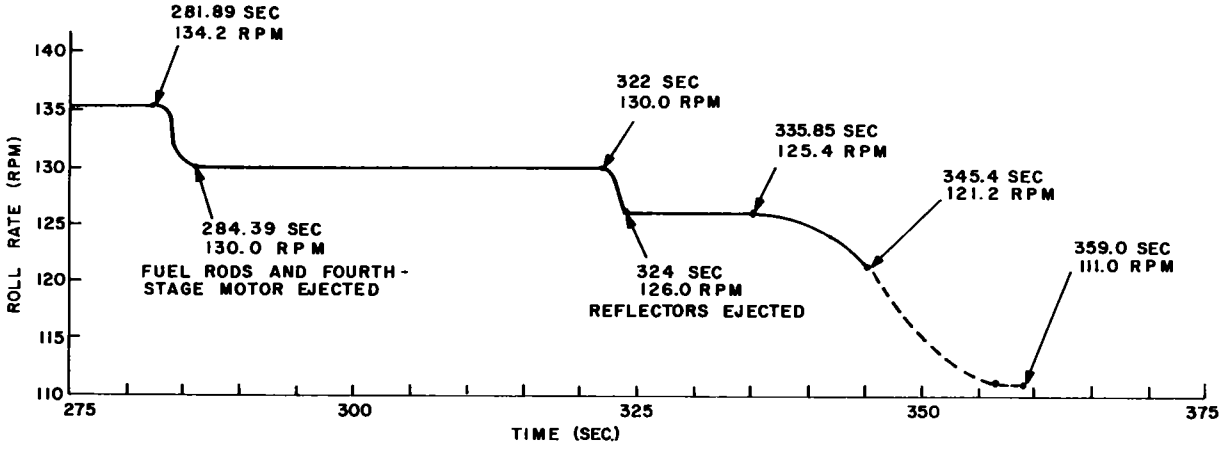

Figure 61. RFD-1 roll rate

T12 was located in the NaK fill tube, which was the most forward location of any thermocouple. Again, the data were good, indicating that the melting point should have been reached at around 348 seconds.

T13, T14, T15, T16, T17, and T18 were located in the lip weld on top of the core vessel. T14 and T17 were in an unobstructed flow path, while T13, T16, T15, and T18 were in the shadow of the NaK tube and fins. Data from T14 and T17 were very good, indicating the material reached melting temperature at 350 seconds, before blackout. The rest of the thermocouples in the obstructed flow read around 1000°F or less at blackout. However, it should be kept in mind that these locations received larger heating inputs as soon as the obstructions burned off.

T19 and T20 were located in the core-vessel wall. It should be noted that heating of the core-vessel wall did not start until the reflectors ejected, at 323 seconds. There was a lag from the time heating started, at 323 seconds, until thermocouple response indicated a change in temperature. The lag was about 3 seconds for T19 and 5 seconds for T20. This lag was much too long to be due only to material response, which is of the order of a few milliseconds. Sandia therefore conducted tests to determine the reason for this lag. A thermocouple similar to the one used on the flight unit was taken from the fin of a SNAP-10A reactor and welded to the back side of a 0.032-inch-thick plate of 316 stainless steel. Two fine chromel-alumel wires were also welded to the same plate about 1/2 inch from the thermocouple. The front side of the plate was then subjected to a heat pulse similar to the one the core-vessel wall is believed to have experienced. The results (Figure 62) indicated that a lag of 3 to 5 seconds may be expected from the time the heat pulse starts until the thermocouple responds.

Comparison of Analytical with Flight Data

Agreement between analytical predictions and flight data is good for most thermocouple locations, particularly for the band joint and the fins. Such disagreement as exists is believed to be due mainly to the fact that the analytical study was based on zero angle of attack for the RV, while the actual angle of attack for the RFD-1 RV varied from 0 to 25.06 degrees during the time of reactor burnup. Local heating varied slightly with angle of attack in all locations, but in some areas the change in heating was pronounced, as shown in Appendix B. The angle of attack coupled with the high roll rate of the RV made heating rates change at too rapid a rate to allow any correlation of angle of attack and roll angle with local heating. See Figures 63 and 64 for pitch and yaw diagrams. Figures 65 through 68 show the coning angle of the RV from 281 to 345 seconds. After the completion of AI's current series of aeroheating tunnel tests, a more complete analysis can be made of variations in local heating resulting from variations in angle of attack.

The motion pictures of re-entry do not show any definite objects behind the RV at the time the fins burned off (approximately 340 seconds). This is believed to be due to the greater distance of the RV from the camera at this time. However, thermocouple data are sufficient to confirm that the fins burned off. At 354 seconds, objects can be seen behind the RV on the motion pictures. This time is in agreement with analytical analysis and the extrapolation of thermocouple data for burnup of the pump, NaK tube, and core-vessel lid. The analytical prediction for the time at which the core-vessel wall would reach melting temperature (approximately 361 seconds) coincides reasonably well with the motion-picture data, which show objects behind the RV at 365 seconds, corresponding to an altitude of 153,000 feet.

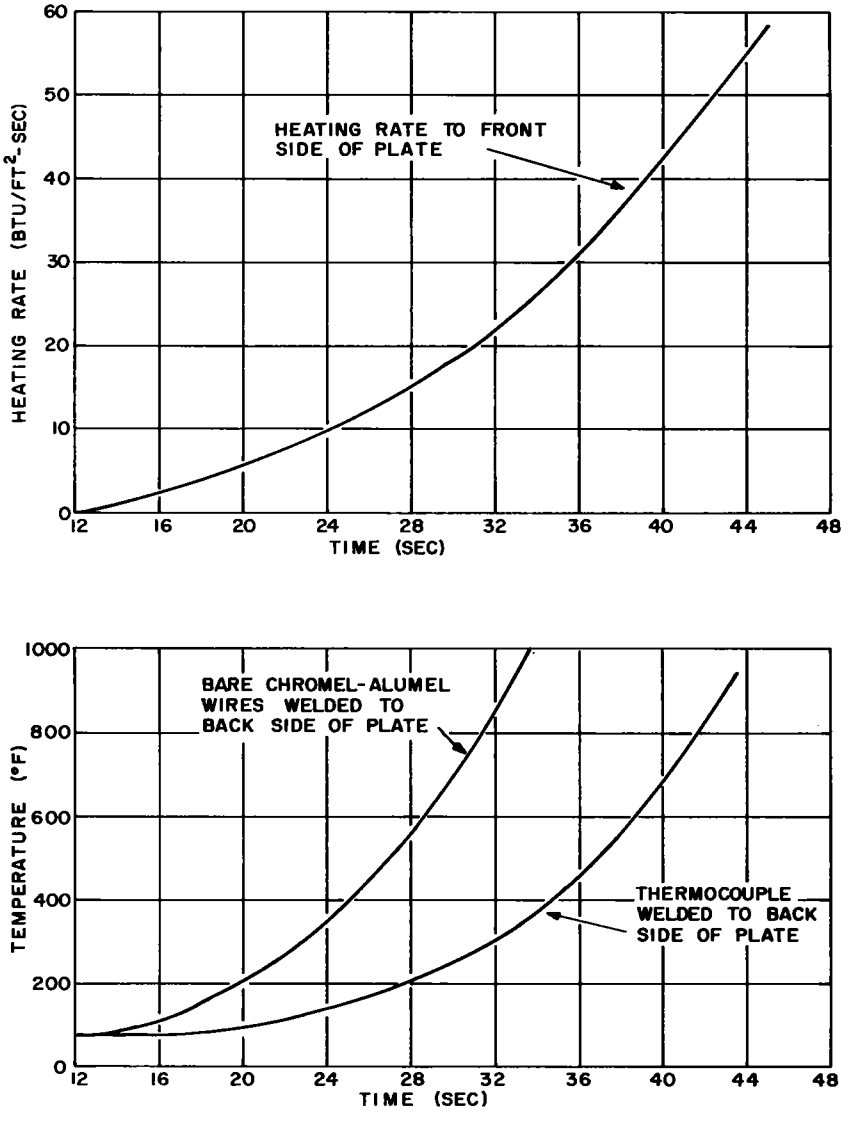

Figure 62. Results of tests to determine reasons for thermocouple lag

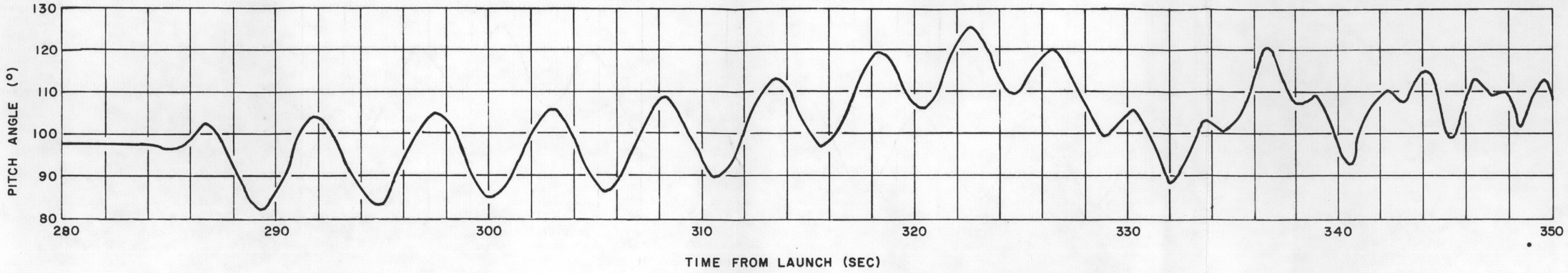

Figure 63. RFD-1 pitch angles, 280 to 350 seconds

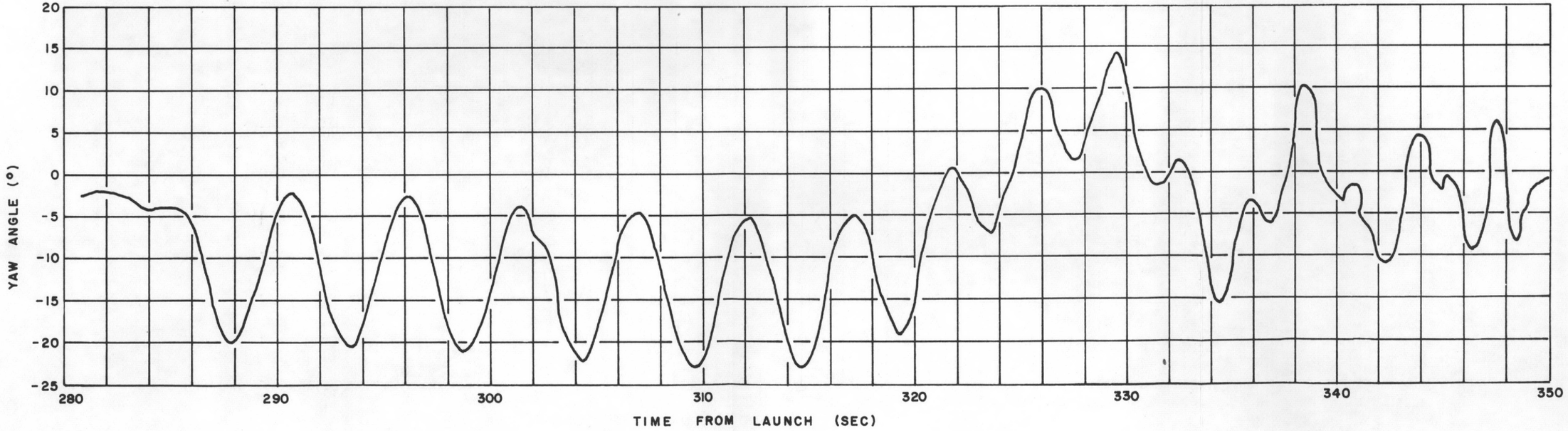

Figure 64. RFD-1 yaw angles, 280 to 350 seconds

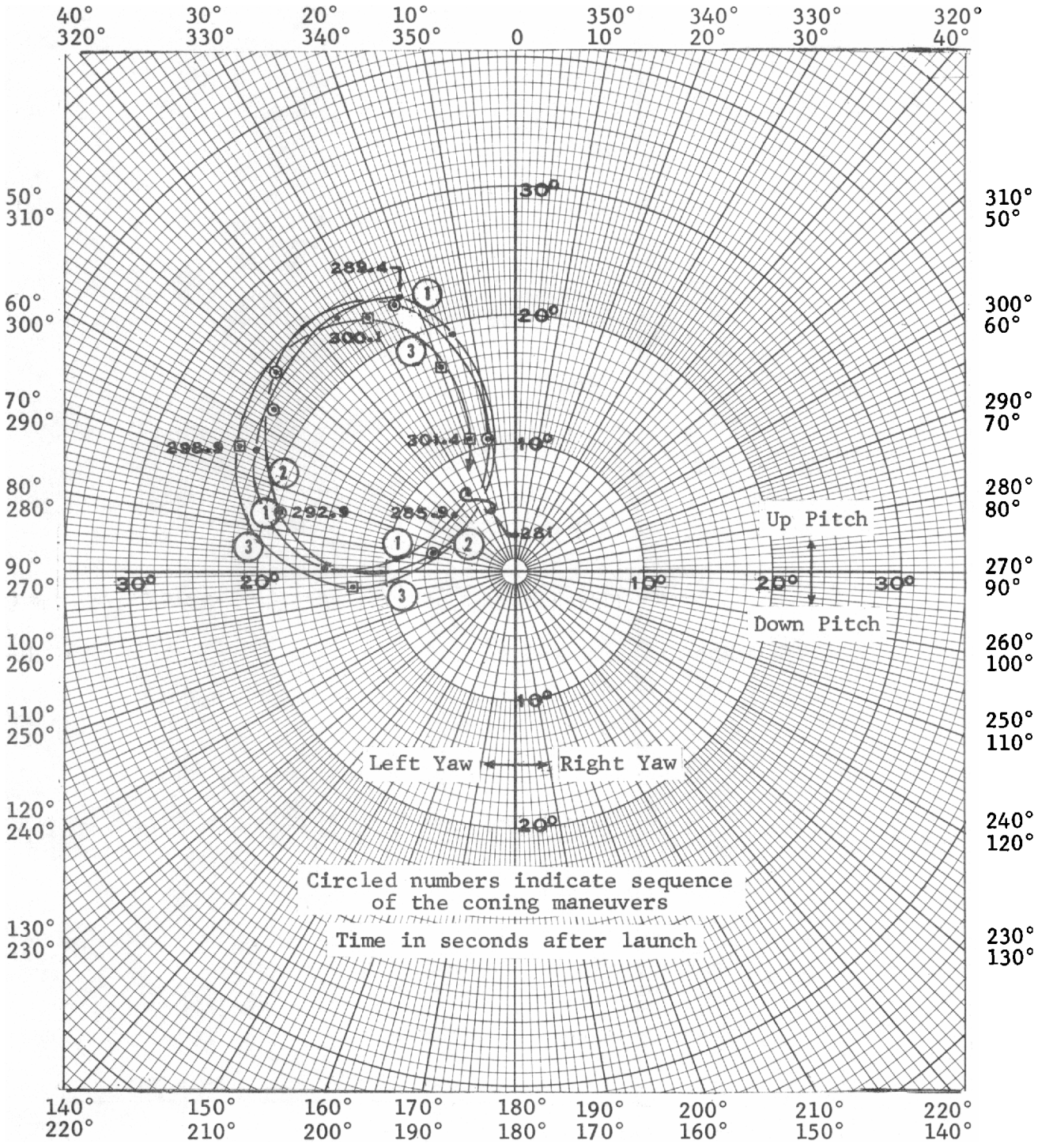

Figure 65. RFD-1 coning angle relative to the flight path, 281 to 301.4 seconds

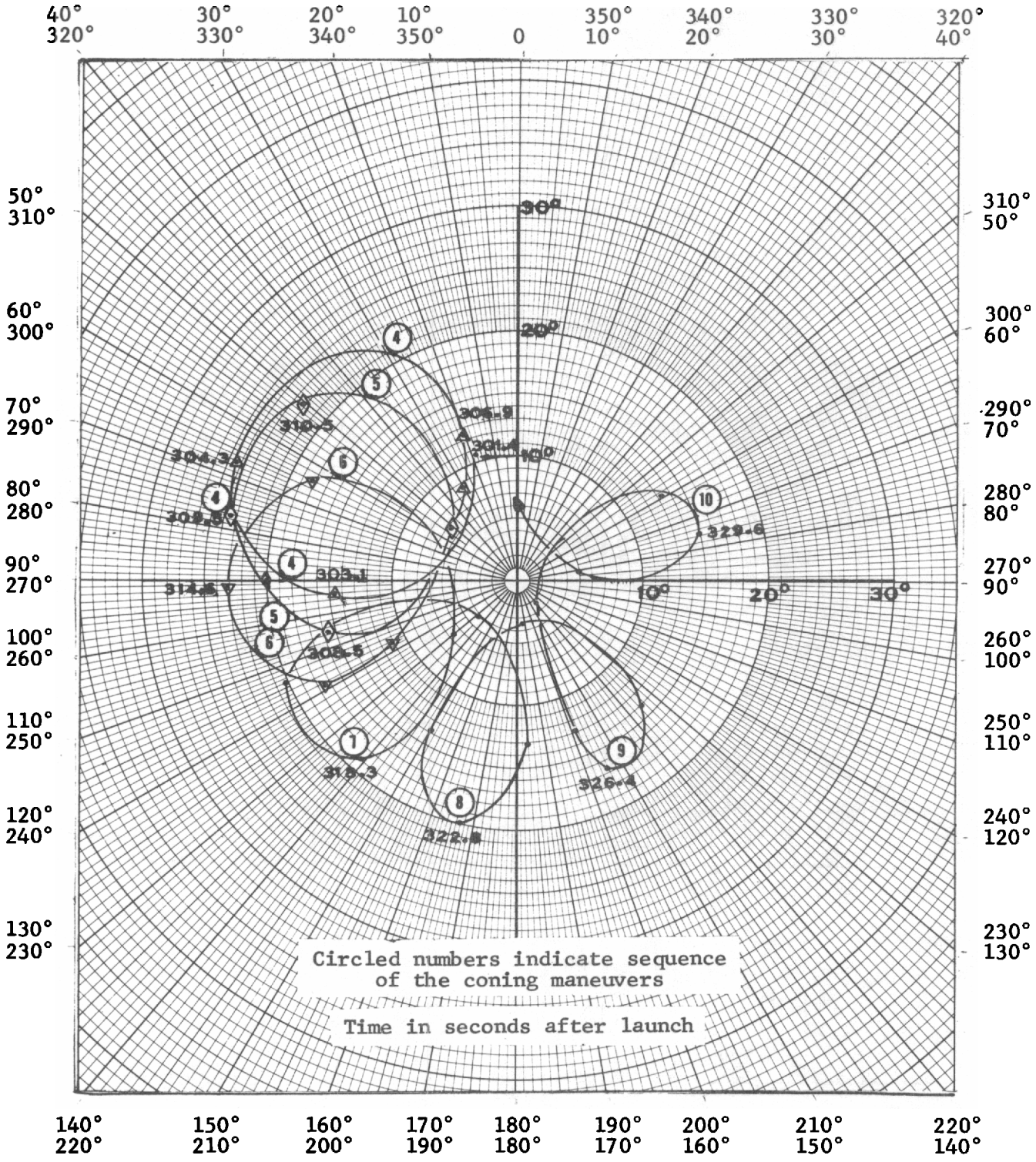

Figure 66. RFD-1 coning angle relative to the flight path, 301.4 to 329.6 seconds

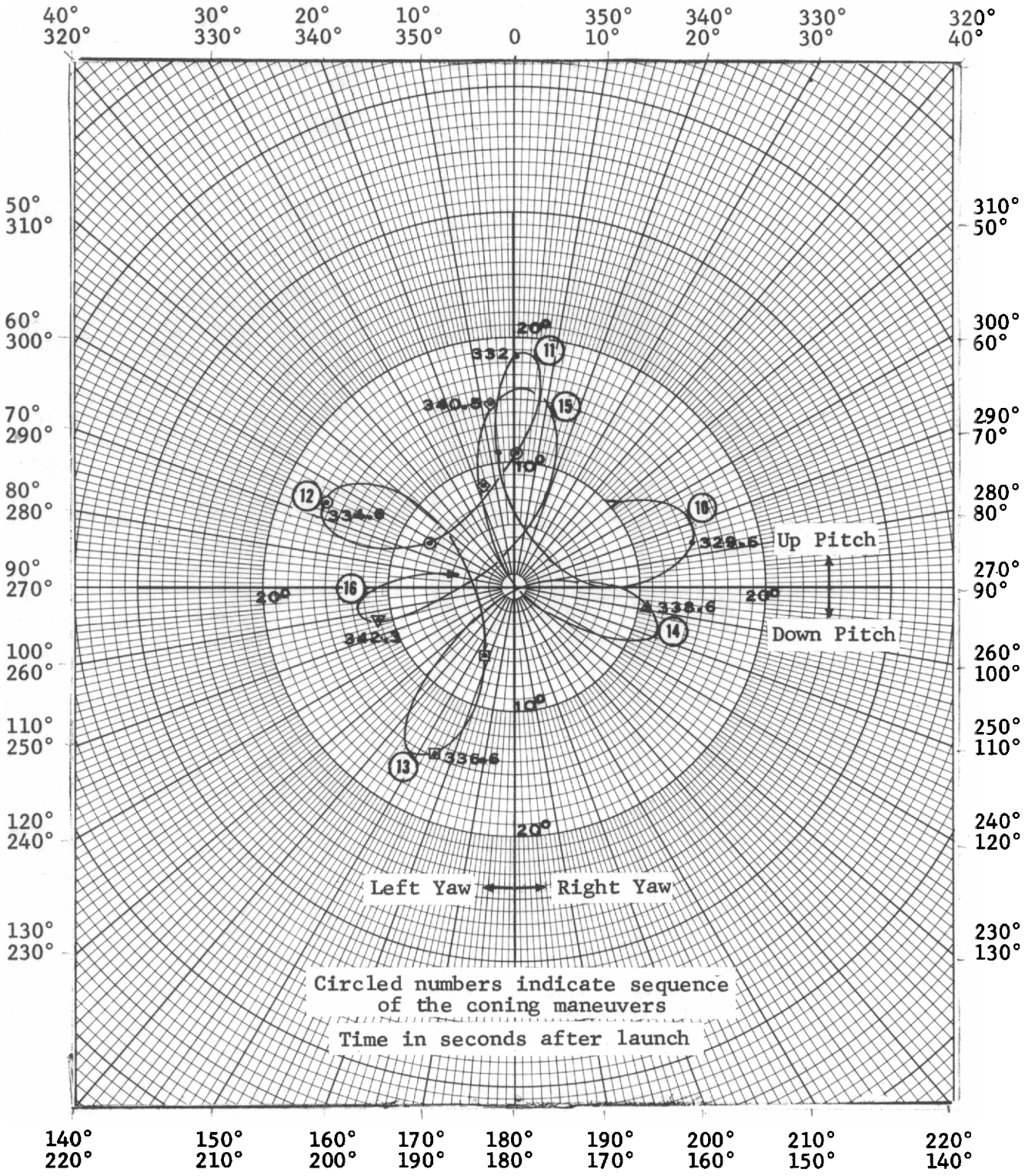

Figure 67. RFD-1 coning angle relative to the flight path, 329.6 to 342.3 seconds

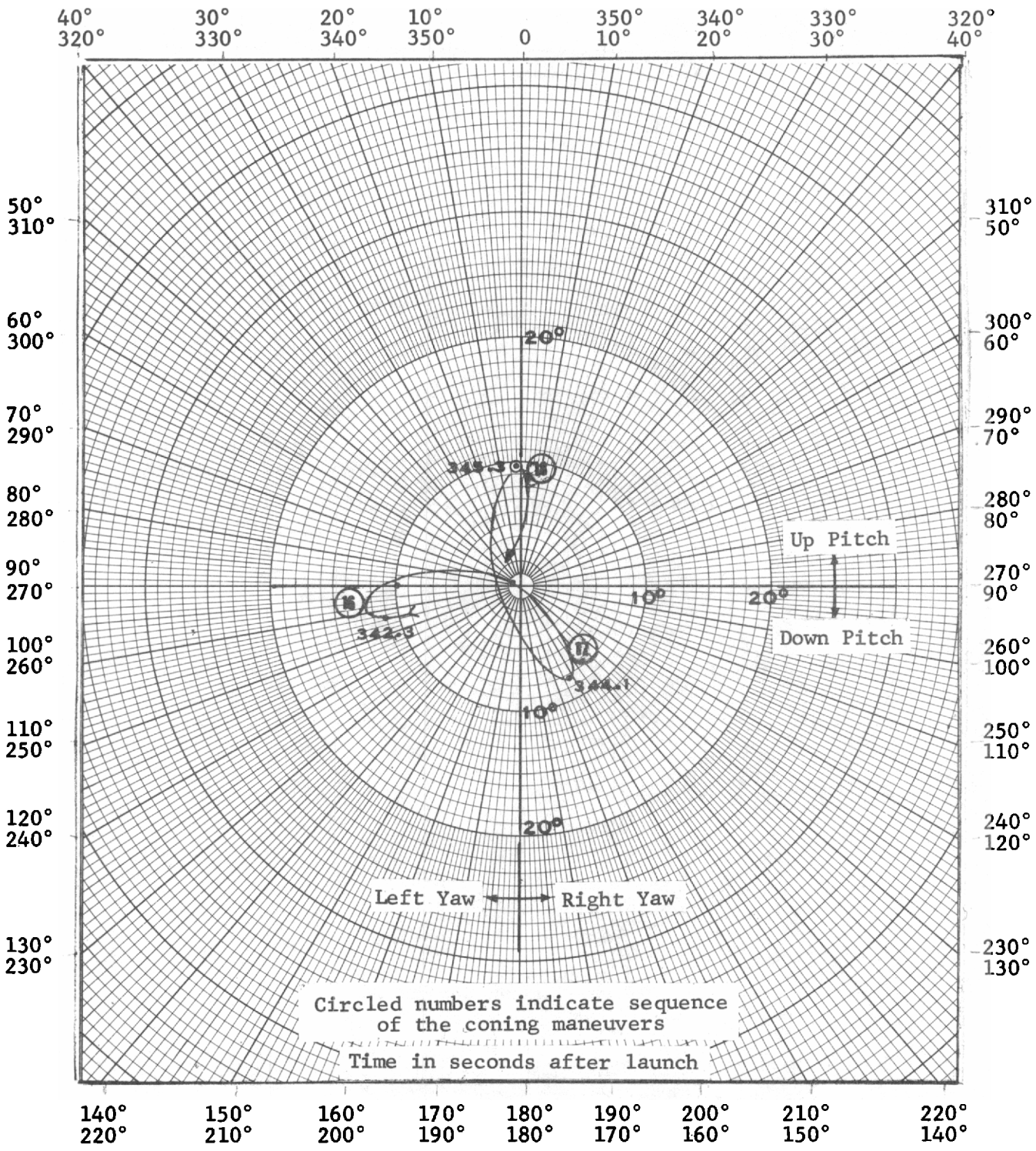

Figure 68. RFD-1 coning angle relative to the flight path, 342.3 to 345.3 seconds

Spectral Data

Spectral data for RFD-1 and the instrumentation used in acquiring these data are discussed in SC-RR-64-516. The reader is referred to that report for details. Some of the spectral data were informative as to the possible sequence of events that concern the SNAP-10A reactor mockup, and these will be summarized here.

No direct information could be extracted from the spectral data as to when or where any particular disassembly of the reactor or reactor parts took place. However, the spectral data do show when and where free atoms or molecules of different substances were radiating their characteristic radiation. One can then theorize as to the source of these atoms or molecules and make some statement about certain conditions of their source. For instance, most of the spectral information pertinent to the reactor concerns detection of chromium or chromium-oxide radiation. The only known source of chromium associated with the RV for which a trajectory has been identified was the stainless steel which made up the reactor. One can therefore say that when chromium radiation was detected, the stainless steel had melted, the heat input at that time was sufficient to cause vaporization at the surface of the material, and spectral excitation of some of the atoms or molecules of the material occurred. The vaporization may have occurred from partial melting of an intact body, or from a body which had melted entirely. At times, only chromium atomic lines are intense. At other times, very strong chromium-oxide bands and atomic lines are present, indicating high rates of chromium oxidation. The intense radiation occurring in flares during peak heating had intense chromium oxide band and atomic chromium line radiation. Iron radiation was also detected during this time. This would be consistent with stainless-steel vaporization. The high radiation level during these big flares indicates that significant amounts of stainless steel were molten and perhaps breaking up into smaller globules, exposing more area to surface oxidation. No statement can be made from the spectral data as to whether or not these parts were attached to the RV during these flares. The zero-order traces show no evidence of diverging, but the reactor could have been disassembled and following the same trajectory as the RV.

The zero orders are the traces which are recorded as though the grating were not in front of the camera lens, except that the intensity of the transmitted radiation is reduced. Hence, the zero-order traces correspond to an open-camera trajectory recording. Most of the radiation striking the grating-lens assembly was recorded in the first-order spectrum because of the grating blaze angle (shape of the grating grooves). In the first-order, the spectrum is dispersed, with the longer wavelengths being farther away from the zero order. The amount of dispersion is determined by the number of grooves per millimeter on the grating and the focal length of the lens employed. Second-, third-, and higher-order spectra are recorded only if the incident radiation is very intense. When higher-order spectra are recorded, they have higher dispersion or separation of wavelengths on the plate than in the first order.

Sodium radiation was associated with the RV and believed to originate as an impurity in the fiberglass-filled ablative covering on the RV. The sodium doublet at 5890 and 5896 Å serves as a convenient wavelength reference point.

TM data indicated that the aluminum fins on the front of the reactor were at melting temperature from 336 to 342 seconds. Aluminum was detected spectrally, indicating vaporization temperature, from about 343.5 to 347.5 seconds. However, since the zero-order traces were multiple at this time, the aluminum spectra cannot definitely be associated with the fins. Other aluminum objects (fuel-rod brackets and reflectors) should also have been burning up at this time.

Chromium and iron lines were detected from about 343 seconds until about 384 seconds, but with fluctuations in intensity. Chromium was also present as a constituent in the fuel-rod cladding, so the source of the early chromium was ambiguous. This was particularly true since the streak spectrographs were the instruments which detected the early chromium. On the open-camera plate spectrographs, the zero-order and spectra could often be correlated through their common intensity fluctuations. Later in the re-entry, it became easier to associate the proper spectra with the RV-reactor complex.

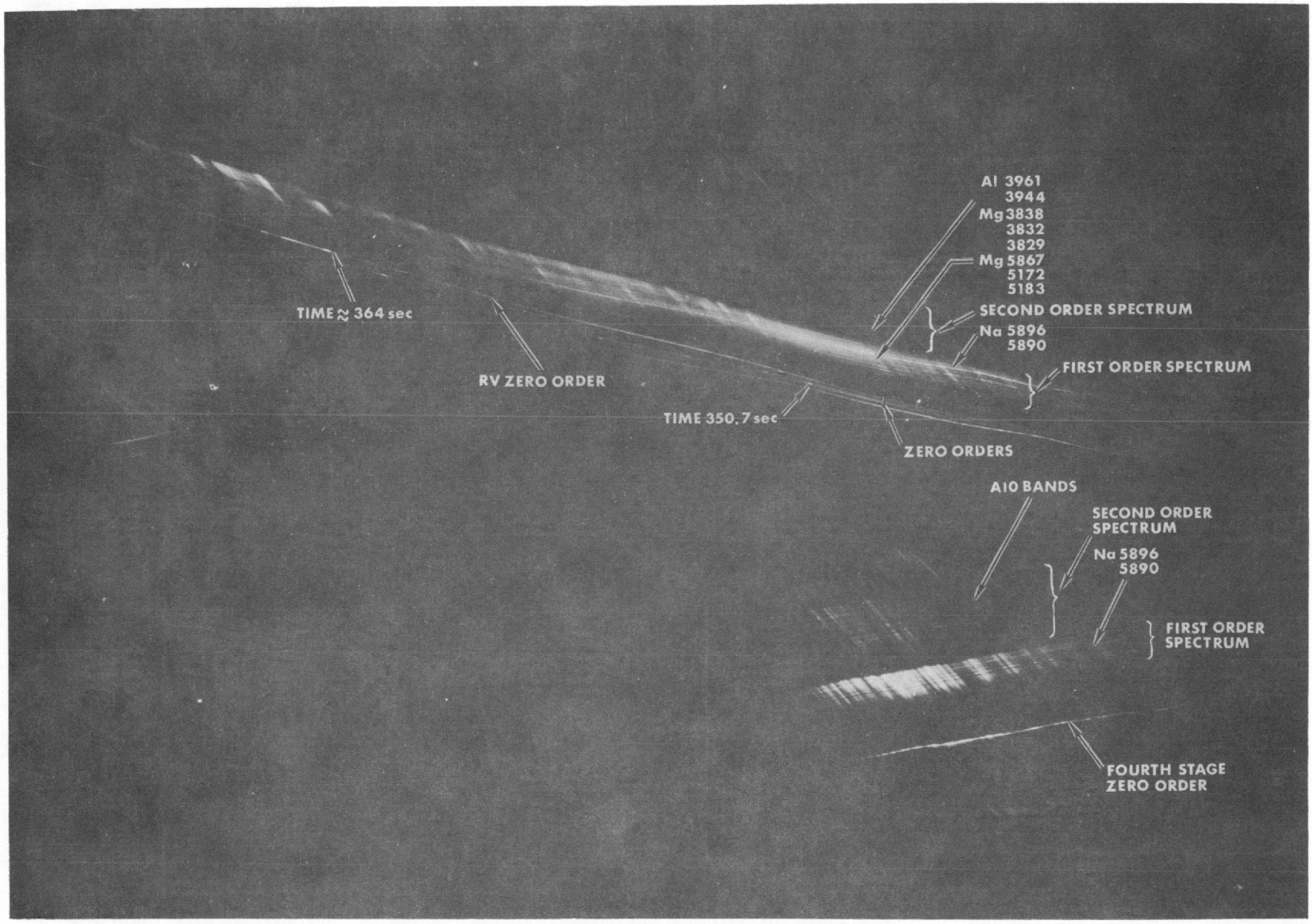

Figure 69. Low-dispersion spectrogram taken early in the re-entry sequence

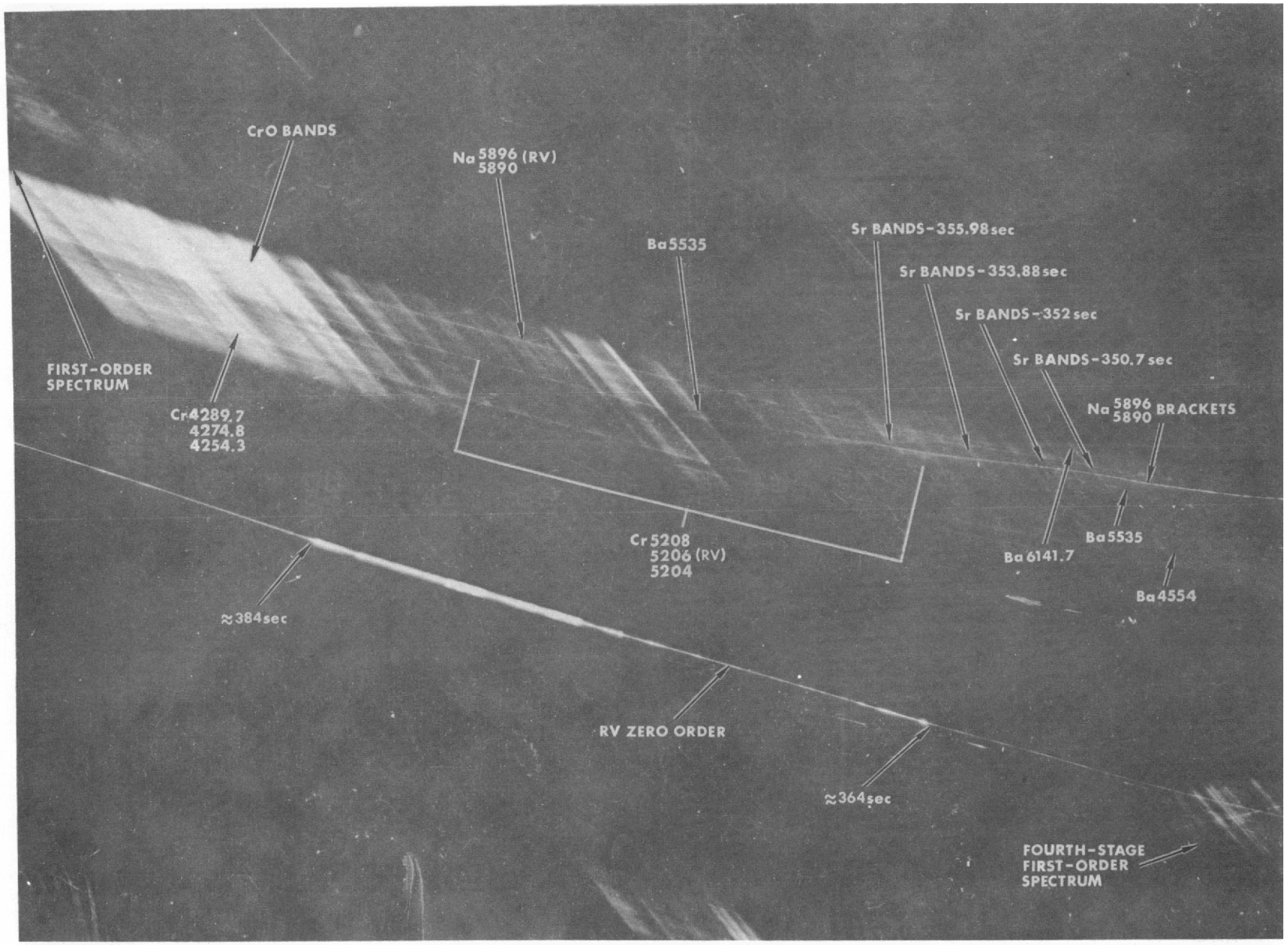

Figure 70. Higher-dispersion spectrogram, taken later in the re-entry sequence

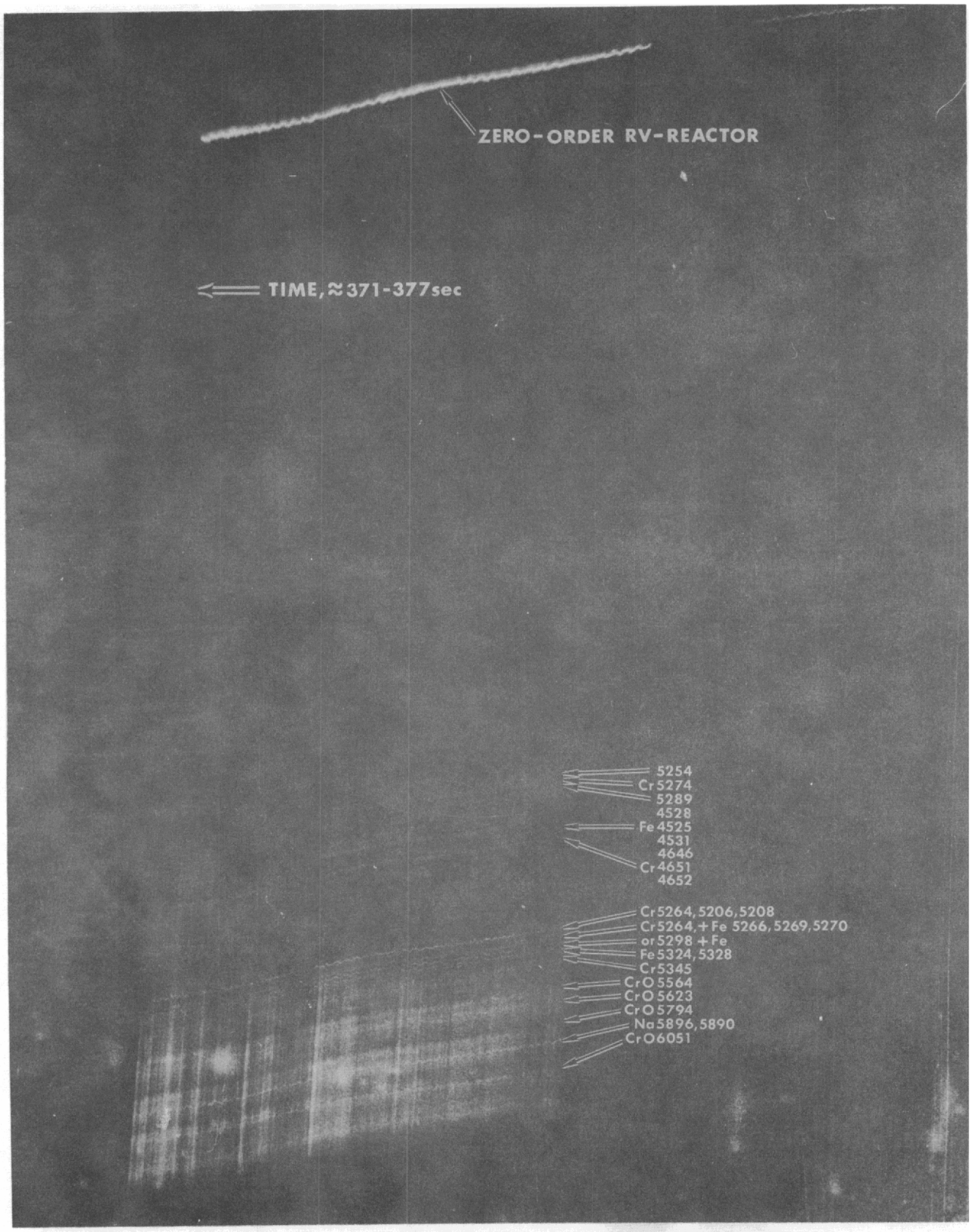

Figure 71. Spectrogram covering the period from 371.3 to 377 seconds

Figures 69 and 70 are spectrograms of the re-entry recorded by instruments aboard the NASA aircraft. The NASA aircraft was positioned near the splash point, so its cameras recorded more of the final part of the trajectory. Figure 69 is a low-dispersion spectrogram from early in the re-entry sequence, where the fuel rods flared. Note the fourth stage at the lower right and its strong aluminum oxide band radiation. The upper streak in the zero-order has been identified as originating from the RV-reactor assembly. This spectrogram is included because it shows the zero-order and spectra relationship over a large part of the trajectory.

Figure 70 is a higher-dispersion spectrogram, and the zero-order covers the time later along the flight path than Figure 69. However, due to the tilt of the grating, the spectra cover about the same region. Spectral lines and bands are identifiable here and have been labeled on the spectrogram. Chromium that can be associated with the RV-reactor assembly was detected here from about 350 seconds through the big flare that ends at about 384 seconds. This flare was more intense at about 354 seconds, then faded, and then became very intense from about 364 seconds until 384 seconds. Chromium-oxide molecular radiation was very intense from about 364 seconds until 367 seconds, when it faded, and then again became very intense from about 372 until 384 seconds. The chromium lines and chromium-oxide bands identified are better seen in Figure 71, a spectrogram taken from AFSWC Aircraft 521. This spectrogram was taken from 371.3 seconds until 377 seconds during the big reactor flare.

SECTION VI -- EVALUATIONS AND CONCLUSIONS

Evaluation of Flight Information

Data obtained from RFD-1 have been reduced, and indicate that the SNAP-10A burned up at an altitude above 153,000 feet. TM data were good until blackout, with all thermocouples reading. Optical data correlated with the thermocouple and other TM data to further verify the sequence of reactor disassembly.

Evaluation of Analytical Studies

One of the objectives of the RFD-1 flight was to permit an evaluation of the accuracy of analytical burnup studies based on laboratory tests. As already noted, there was excellent agreement between flight data and the results of the postflight analytical study.

On regularly shaped bodies which enter at known and repeatable angles of attack, there should be no great problem in calculating burnup, provided material properties and reaction rates are known. However, heat rates to complex shapes such as the SNAP-10A are very dependent on angles of attack. Shock-wave/boundary-layer interactions, which increase heating, move and change magnitude with angles of attack. In addition, protuberances redirect flow as the angle of attack changes. Therefore, in order to analyze complex shapes which are not stable, the attitude must be known accurately and wind-tunnel tests must be run to cover all possible attitudes. This indicates that analytical burnup studies of complex-shaped tumbling bodies may only be able to bracket the range of possible destruct altitudes rather than predict the most probable altitude. However, it should also be noted that nonstabilized flight tests of this type of body would not be repeatable and the results of a single flight test would not accurately determine the range of burnup altitudes. Although stabilized flight tests may not duplicate re-entry of an operational reactor they are a greater aid in evaluating the analytical methods used to calculate the range of burnup altitudes. Also, since the angle of attack is known, additional aero-heating data can be obtained as well as validating similar data from wind tunnel tests.

Conclusions

The preflight and postflight studies of reactor disassembly used the same assumptions and method of analysis, but the preflight study was based on the predicted trajectory and a standard atmosphere, while the postflight study used the observed trajectory and measured atmospheric properties. The postflight analysis showed reasonable agreement with the flight-test data, considering that the analytical study was based on zero-degree angle-of-attack wind-tunnel heating data, while the RFD-1 RS oscillated slightly. However, work is continuing in an effort to get better correlation between the flight data and the analytical analysis. Since the analytical method for the RFD-1 study proved satisfactory, this same method will be used for the orbital-decay analysis of an operational SNAP-10A attached to an Agena.

The Agena/SNAP-10A safety study will follow in another report. However, burnup of the STR has been computed assuming the RFD-1 RS re-entered on an orbital-decay trajectory. Figure 72 compares the stagnation-point heating curves for the actual RFD-1 trajectory and the RFD-1 orbital-decay trajectory. Although this interim analysis shows the difference in reactor disassembly for the RFD-1 trajectory and an orbital-decay trajectory, it definitely does not give the altitudes at which the Agena/SNAP-10A will disassemble because of the assumed zero-degree angle of attack and the higher ballistic coefficients of the RFD-1 RS.

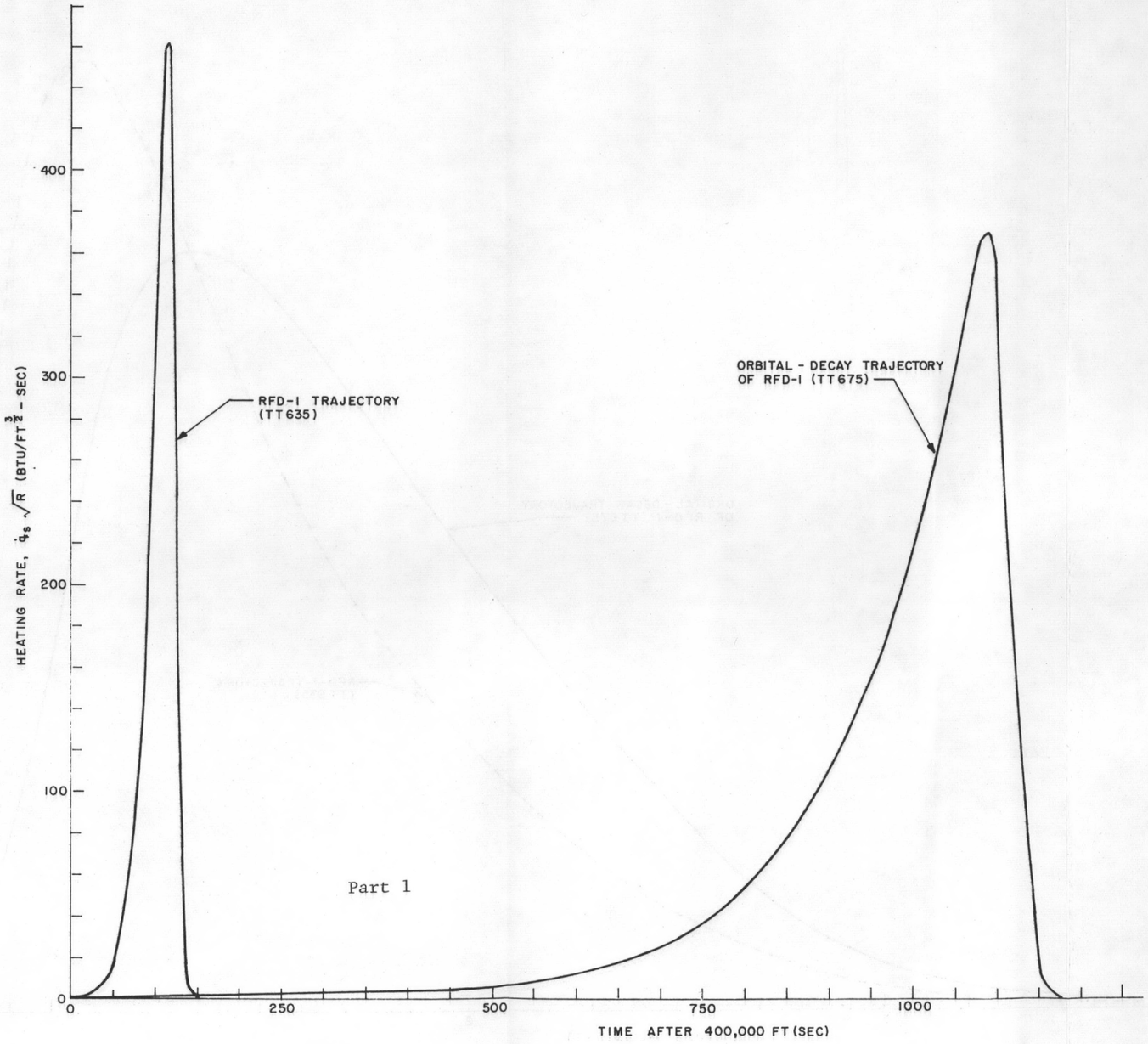

Figure 72. Stagnation-point heating on a 1-foot-radius hemisphere: a comparison of the RFD-1 orbital-decay trajectory and the actual RFD-1 trajectory

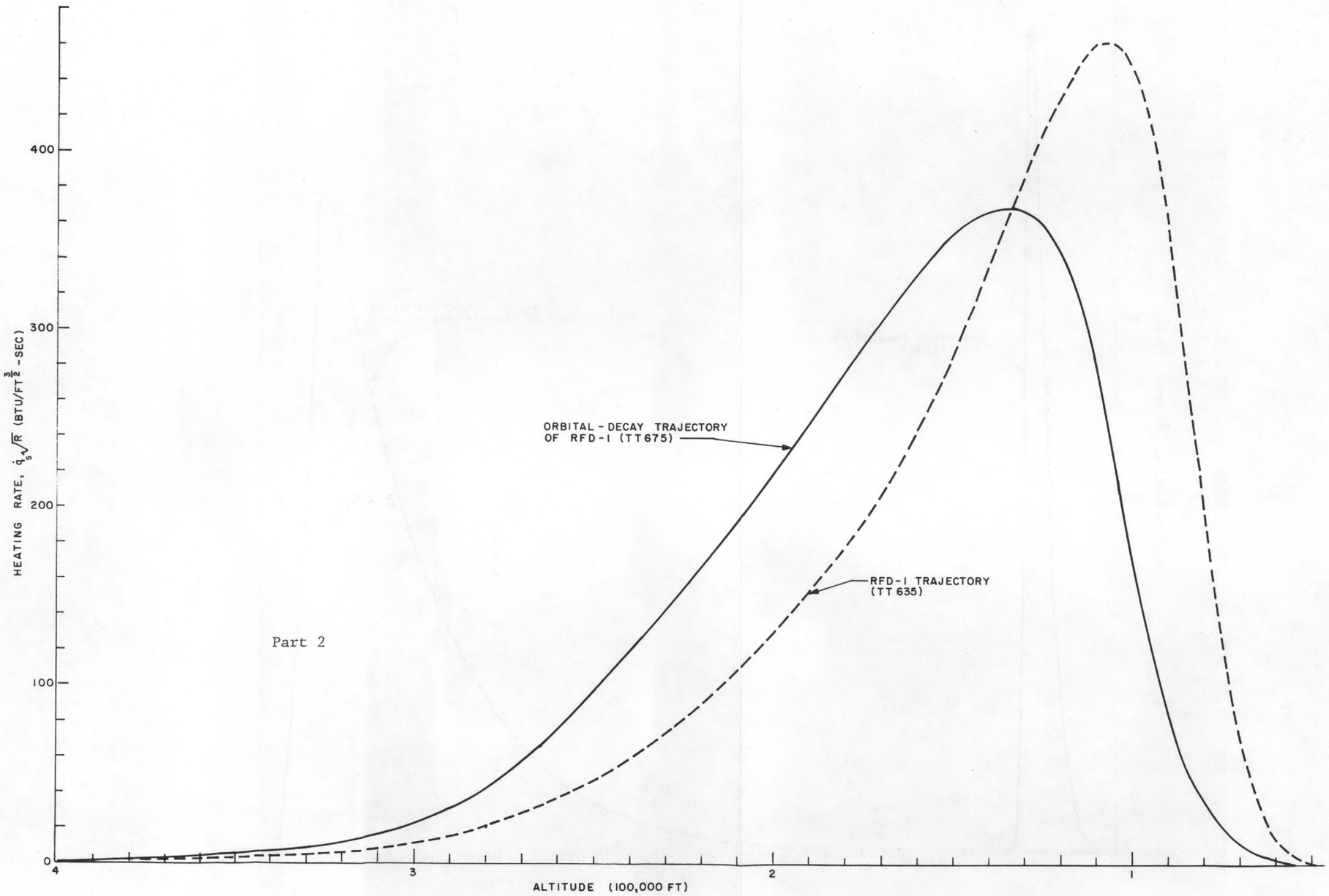

Figure 72 (cont). Stagnation-point heating on a 1-foot-radius hemisphere: a comparison of the RFD-1 orbital-decay trajectory and the actual RFD-1 trajectory

The assumptions used for the RFD-1 orbital-decay study were:

1. Re-entry velocity = 25,600 ft/sec
2. Re-entry angle -0.05°
3. Angle of attack = 0°
4. W/C_DA versus altitude = the same as for the RFD-1 flight (see Figure 51 and Table VI)
5. Transition from free-molecular to continuum flow takes place at 310,000 feet
6. The fusible-link band was the same as on the STR, i.e., 0.032-inch thick by 0.5-inch wide, with brazed joints that melt at 1220°F
7. Oppenheim's method[1] was used to compute free-molecular heating to the reflector band joints
8. Continuum-heating ratios (F_q) were:

   Band front = 12.1
   Band sides = 0.268
   Core-vessel sides = 0.17

9. Thermal emissivity of 316 stainless steel was 0.3 up to 1650°R, then increased linearly to 0.7 at 2200°R and remained 0.7 to the melting temperature (2960°R)
10. The core-vessel walls received no aeroheating until the reflectors ejected.

Figure 73 shows the altitude and stagnation-heating rate to a 1-foot-radius sphere versus time for the resulting trajectory. Also shown are the points in the trajectory where the reflectors eject and the core-vessel walls melt. Reflector ejection was found to take place at 310,300 feet altitude, and the core-vessel wall failure at 226,100 feet.

To show the large effect of emissivity on the destruct altitude of materials with high melting temperatures, the RFD-1 orbital-decay study was repeated assuming a constant emissivity of 0.4 for 316 stainless steel. The following table gives the comparative times, altitudes, and total stagnation aeroheating required to melt the core-vessel walls.

Emissivity	Time from 400,000 feet (sec)	Altitude (ft)	$\dot{Q}_s\sqrt{R}$ (BTU/ft$^{3/2}$-sec)
Constant 0.4	775	252,921	12,705
Variable 0.3 to 0.7	855	226,089	22,298

Currently, there is very little data on high-temperature emissivity, and that which is available shows considerable scatter. Therefore, an extensive study has been initiated to accurately determine the emissivity and surface conditions of nuclear power supply materials under simulated re-entry environments.

Another point brought out by this comparison study is that, whenever feasible, low-emissivity materials, finishes, or coatings should be used on future nuclear power supplies which are designed to burn up during re-entry. This is particularly important when materials with high melting temperatures are used.

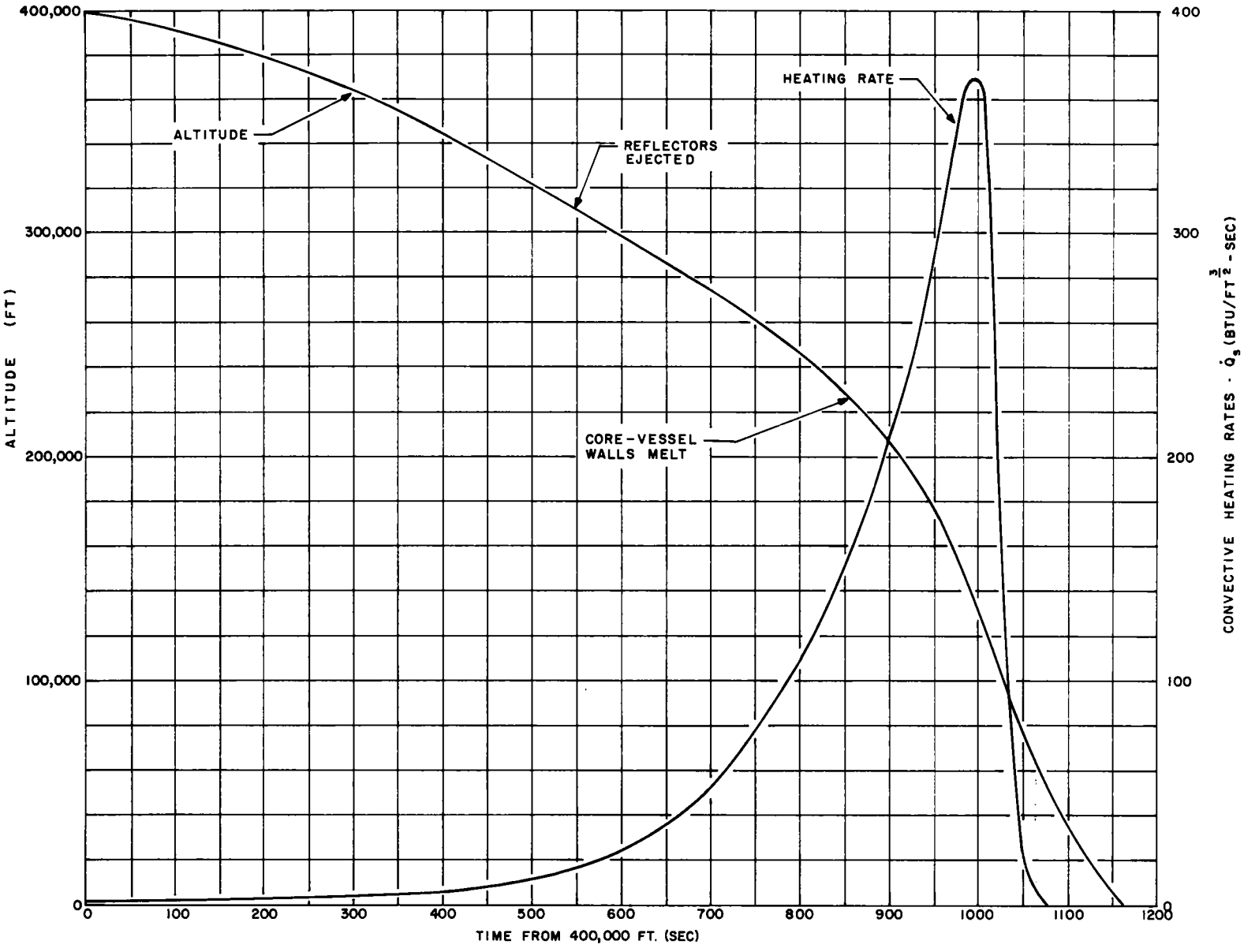

Figure 73. Orbital-decay trajectory of RFD-1

APPENDIX A

AEDC Aeroheating Wind-Tunnel Tests

Notation:

α = angle of attack (degrees)

N_{ReL} = Reynolds number based on scaled RS length

P_o = stagnation pressure (psia)

ρ_o = stagnation density (atmospheres)

T_o = stagnation temperature (°R)

$\dot{q}_o$ = stagnation heating rate on a hemisphere-cylinder with a 1-inch diameter (BTU/ft²-sec)

M_∞ = free-stream Mach number

V_∞ = free-stream velocity (ft/sec)

P_∞ = free-stream pressure (psia)

ρ_∞ = free-stream density (atmospheres)

T_∞ = free-stream temperature (°R)

$\dot{q}_L$ = local heating rate on the flight vehicle (BTU/ft²-sec)

$\dot{q}_s\sqrt{R}$ = stagnation heating rate on a sphere with a 1-foot radius (BTU/ft$^{3/2}$-sec)

$\dot{q}_m$ = local heating rates on models (BTU/ft²-sec)

P_m = local pressure on models (psia)

H_o = stagnation enthalpy ft²/sec² or ft-lb/slug

$F_q = \dot{q}_L/\dot{q}_s\sqrt{R}$ (ft$^{-1/2}$)

L = length (ft)

R = nose radius (ft)

t = time (sec)

APPENDIX A

AEDC Aeroheating Wind-Tunnel Tests

Information on local heating rates on the RFD-1 RS was needed to predict failure modes and disassembly times of the simulated SNAP-10A reactor and to design the thermal protection for the RV to be used for the RFD-1 flight. The data on the simulated reactor will also be useful in the burnup and disassembly analysis of an operational SNAP-10A during re-entry from a decaying orbit. A preliminary analysis of the RFD-1 RS showed that flow over the complex shape of the reactor, which was further complicated by many shock-wave/boundary-layer and shock-wave/shock-wave interactions, made a purely analytical study of aerodynamic heating impractical. A series of wind-tunnel tests was therefore initiated to determine the ratios of local-to-stagnation pressure and heating for the surface of the RS. The heating ratios, when used in conjunction with calculated stagnation heating rates, define local heating rates on the re-entering vehicle. Pressure ratios were needed to more accurately predict separated-flow regions and to study heating rates and transition from laminar to turbulent flow.

These tests, which were requested for Sandia by AFSWC, were performed in the 100-inch Hypervelocity Tunnel F of the von Kármán Gas Dynamics Facility, AEDC, from December 3, 1962 to January 11, 1963. This "hot-shot" tunnel, shown in Figure A-1, operates with nitrogen gas which is heated and pressurized by an electric arc and expanded through a nozzle to velocities of about Mach 19, with fully developed flow lasting approximately 30 milliseconds.

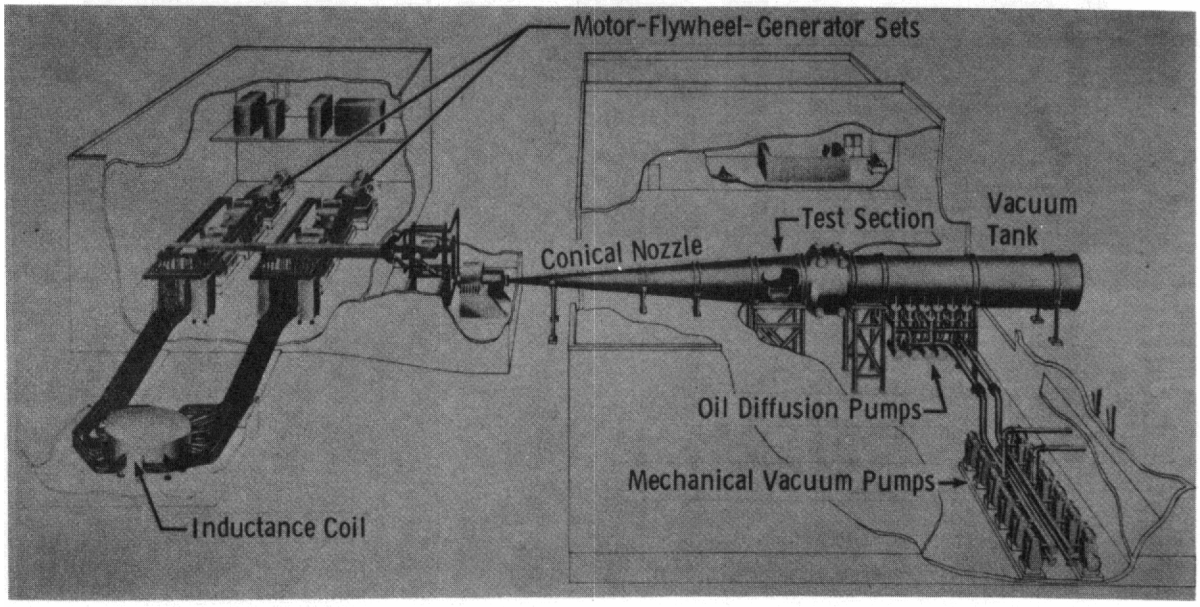

Figure A-1. AEDC 100-inch hypervelocity wind tunnel

Three model configurations were used for these tests. Configuration 1, shown in Figure A-2, was a full-scale model of the forward half of the RV cone section and the reactor, less reflectors. Configuration 2, shown in Figure A-3, was identical to Configuration 1, except that the NaK pump and tubes were removed to simulate a later stage of disassembly. Configuration 3 (Figure A-4) was a quarter-scale model of the entire RS. Each model was run at zero-degree and four-degree angles of attack, which covered the range expected during the greater part of the heating pulse in the flight of RFD-1. Model heating rates were measured with thermocouple-type gages, and pressures were measured with variable-reluctance transducers. Locations of instruments are shown in Figures A-5 and A-6 and in Table A-I. Each run was calibrated with pitot tubes to measure stagnation pressures, and with heat gages mounted at the stagnation point and at the shoulder of 1-inch-diameter hemisphere-cylinders to measure stagnation heating rates. These calibration transducers were mounted on either side of the model, as shown in Figure A-7.

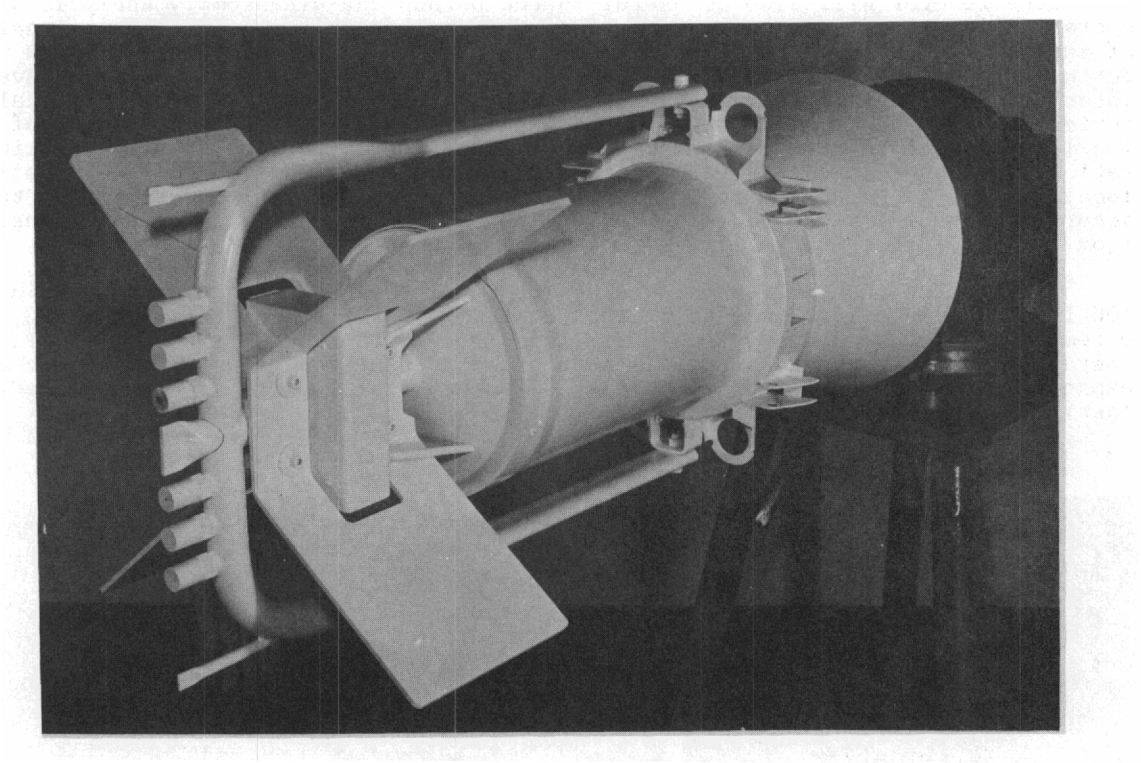

Figure A-2. Wind-tunnel test model, Configuration 1 (full-scale model of the cone section of the RV and the reactor, less reflectors)

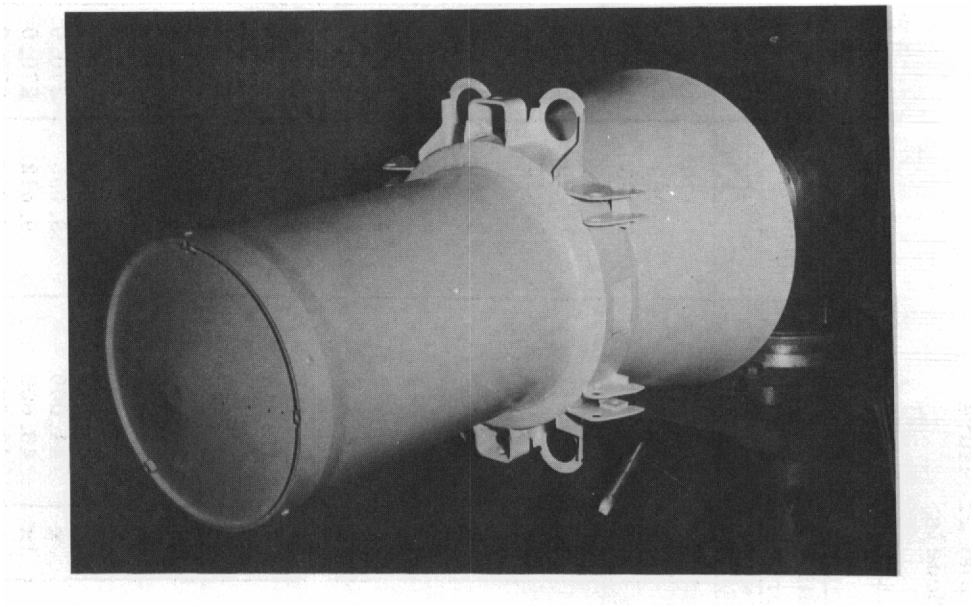

Figure A-3. Wind-tunnel test model, Configuration 2 (full-scale model of the cone section of the RV and reactor, less reflectors, NaK pump, and NaK tubes)

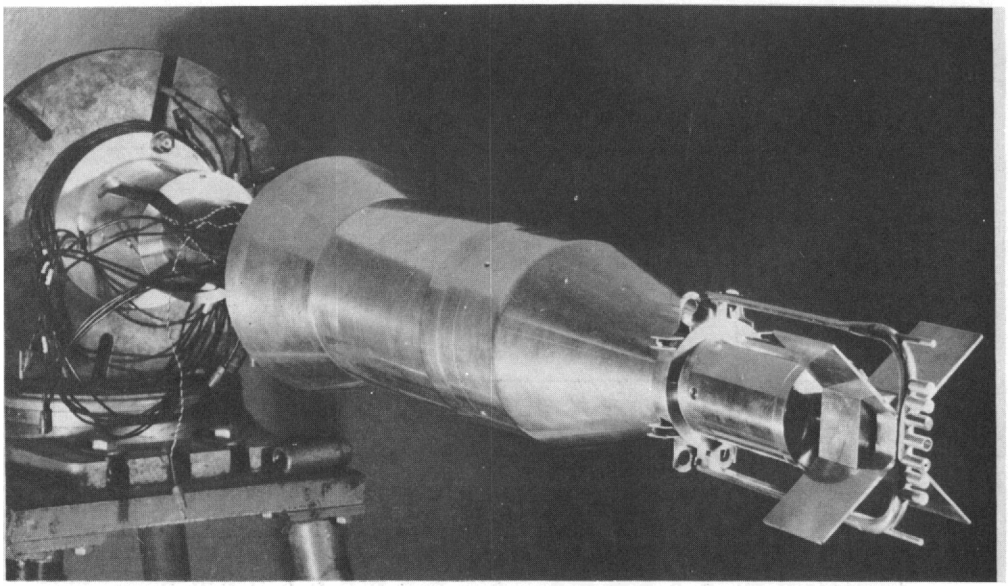

Figure A-4. Wind-tunnel test model, Configuration 3 (quarter-scale model of the complete RS)

TABLE A-I

Locations of Heat-Transfer Gages and Pressure Gages on Wind-Tunnel Test Models

Gage No.	Heat-Gage Location						Pressure-Gage Locations					
	Configuration Number			Station, x, in. (full scale)	Radius, r, in.	ϕ, deg	Configuration Number			Station, x, in. (full scale)	Radius, r, in.	ϕ, deg
	1	2	3				1	2	3			
1	x		x	0	1.450	0	x		x	0	1.470	180.0
2	x			2.200	5.590	180.0	x			2.450	6.089	180.0
3	x			2.437	7.592	222.5	x			4.937	1.515	288.9
4	x			5.877	7.806	313.8		x		8.464	1.300	90.0
5	x			4.937	1.508	250.7		x		8.590	1.770	270.0
6	x			8.590	1.770	90.0		x		8.708	2.210	90.0
6		x		8.590	1.770	180.0						
7	x			9.062	3.530	90.0		x		8.826	2.650	270.0
7		x		9.062	3.530	180.0						
8	x	x		9.312	4.430	0		x		8.944	3.090	90.0
9	x	x		9.312	4.430	270.0		x		9.003	3.310	270.0
10	x	x		9.312	4.430	139.5		x		9.062	3.530	90.0
11	x	x		12.457	4.463	180.0		x		9.121	3.750	270.0
12	x	x		21.717	4.463	180.0		x		9.188	4.000	90.0
13	x	x		24.248	5.041	270.0		x		8.216	0	0
14	x	x		24.600	5.500	255.0	x	x		12.457	4.463	270.0
15	x	x		27.436	4.220	180.0	x	x		21.717	4.463	270.0
16	x	x	x	30.600	5.419	180.0	x	x		24.684	4.800	210.0
17	x	x		35.000	6.613	180.0	x	x	x	30.600	5.419	270.0
17			x	44.000	9.055	180.0						
18			x	48.000	9.612	180.0	x	x		35.000	6.613	270.0
18									x	44.000	9.055	270.0
19			x	57.580	9.832	180.0			x	48.000	9.612	270.0
20			x	80.820	9.958	180.0			x	60.600	9.958	270.0
21				85.752	10.609	180.0			x	80.820	9.958	270.0
22				96.000	12.886	180.0			x	85.752	10.609	270.0
23	x	x		25.180	5.500	285.0			x	96.000	12.886	270.0

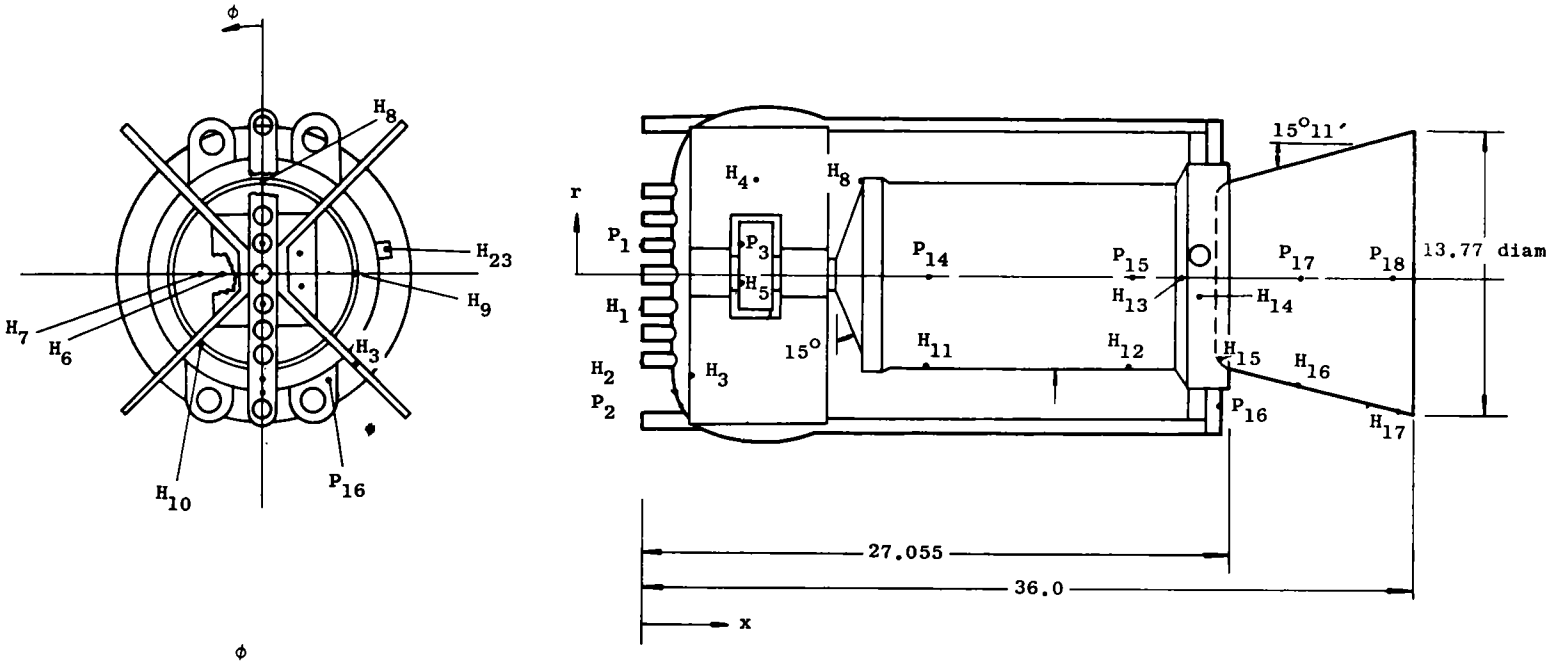

Configuration 1

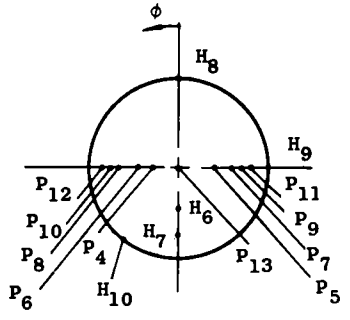

Configuration 2
Face Plate

Notes:
1. Heat Transducer Locations Designated H
2. Pressure Transducer Locations Designated P
3. Configuration 2 Obtained by Removal of Radiative Heat Fins, Tubing, and Pump from Configuration 1
4. All dimensions are in inches.

Figure A-5. Instrument locations on wind-tunnel test models, Configurations 1 and 2

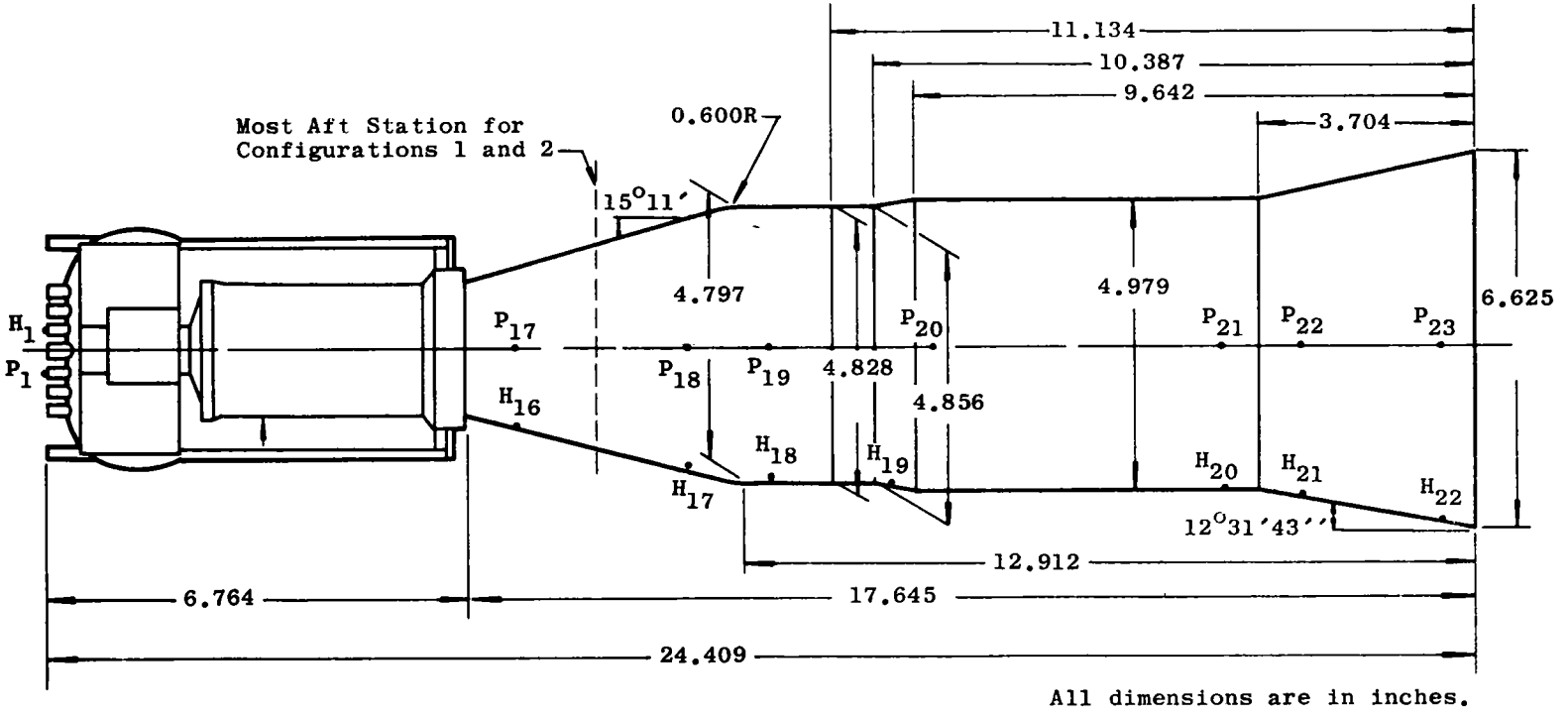

Figure A-6. Instrument locations on wind-tunnel test model, Configuration 3

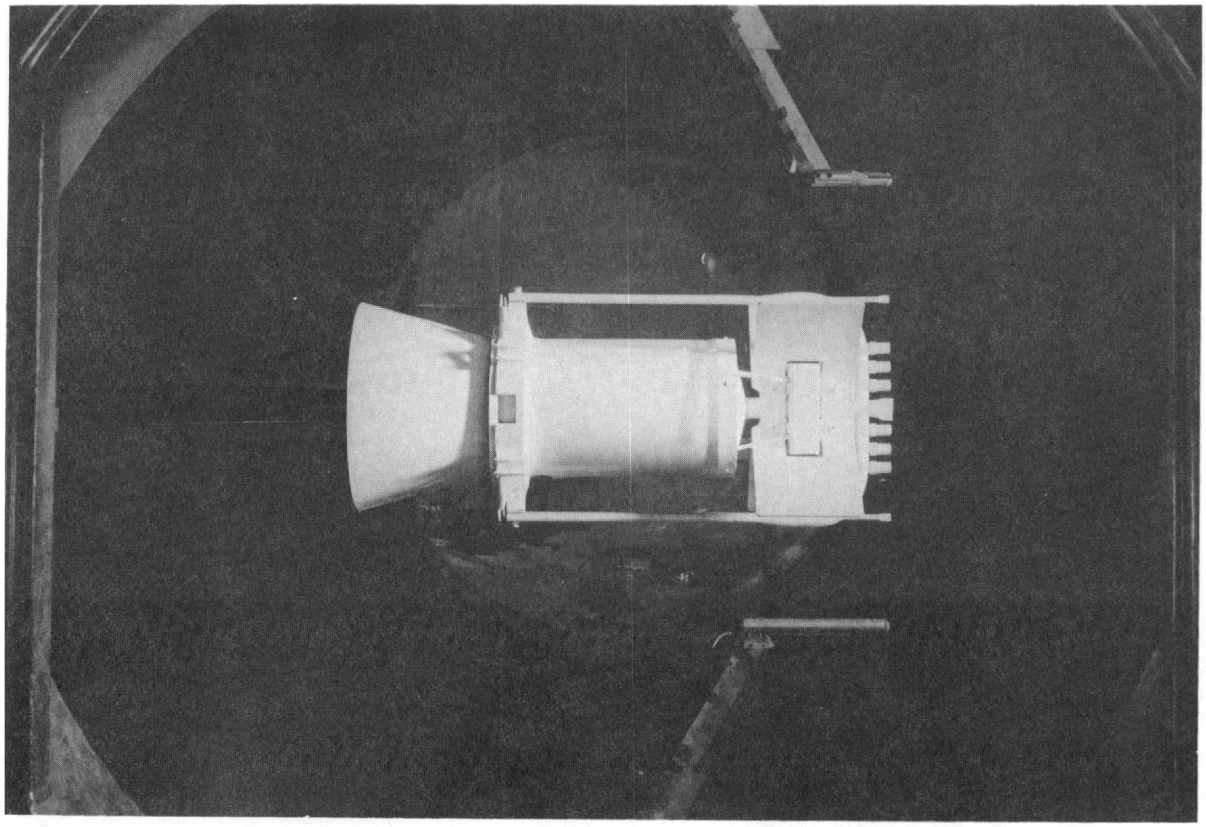

Figure A-7. Location of calibration gages for wind-tunnel tests

Tunnel conditions for each of the 21 successful runs are tabulated in Table A-II. As closely as facility limitations would permit, these tunnel conditions match flight parameters before, during, and after transition from laminar to turbulent flow. Mach numbers remained essentially constant during the test range and were matched satisfactorily in the tunnel tests. The range of Reynolds numbers encompassed the desired range to define heating ratios for both laminar and turbulent flow, as will be seen in the test results. Comparing the stagnation enthalpies given in Table A-II with the flight stagnation enthalpies from Figure A-8 over the test N_{ReL} range of 1.53×10^5 to 4.19×10^5 reveals that test enthalpies were low by a factor of about 5.

It is desirable to put wind-tunnel heating data in the form $F_q = \dot{q}_L / \dot{q}_S \sqrt{R}$. This permitted the local heating rates on the flight vehicle to be obtained simply by multiplying, by the factor F_q, the heating rates on a hemisphere with a 1-foot radius, as obtained analytically by the method described in Appendix C. For a given set of flight conditions, the ratios of local vehicle heating to stagnation heating on a 1-foot-radius sphere can be found by the equation

$$F_q \quad \frac{\dot{q}_m \sqrt{\text{model scale}}}{\dot{q}_o \sqrt{\text{radius of calibration sphere (feet)}}}$$

which results in

$$F_q \quad 4.902 \, \frac{q_m}{\dot{q}_o} \text{ for the full-scale models}$$

and

$$F_q = 2.451 \frac{\dot{q}_m}{\dot{q}_o} \text{ for the quarter-scale model.}$$

The F_q ratios and $\dot{q}_m$ are tabulated for each run in Table A-III, with local pressures given in Table A-IV.

Configurations 1, 2, and 3 during tunnel operation are shown in Figures A-9, A-10, and A-11, respectively. These pictures show some of the shock waves and flow patterns over the vehicle. Since these are standard pictures, which show only light intensity, distinct density gradients do not show up as in schlieren photographs. The brighter areas surrounding leading edges indicate hotter boundary layers and, hence, high heating rates.

The ratio $\dot{q}_L/\dot{q}_s\sqrt{R}$ was found to be a function of Reynolds number in all areas except stagnation regions. In separated-flow regions, the ratio decreased with increasing Reynolds number over the entire test range, which is in agreement with theory and other experimental data[2]. Separated flow exists in recessed and concave areas and on surfaces parallel to flow but directly behind adjoining flow-impinging surfaces. An example of the latter condition is flow over the cylindrical surface just behind the face of a flat-faced cylinder. Figure A-12 shows the Reynolds-number effect on heating ratios on the side of the fins, which is a separated-flow area. This effect can also be seen for Configuration 2 in Figure A-13, which shows the heating ratios on the forward part of the core-vessel walls. However, for Configuration 1, when the pump is in front of the can, the flow is not separated and the heating ratios increase with Reynolds number.

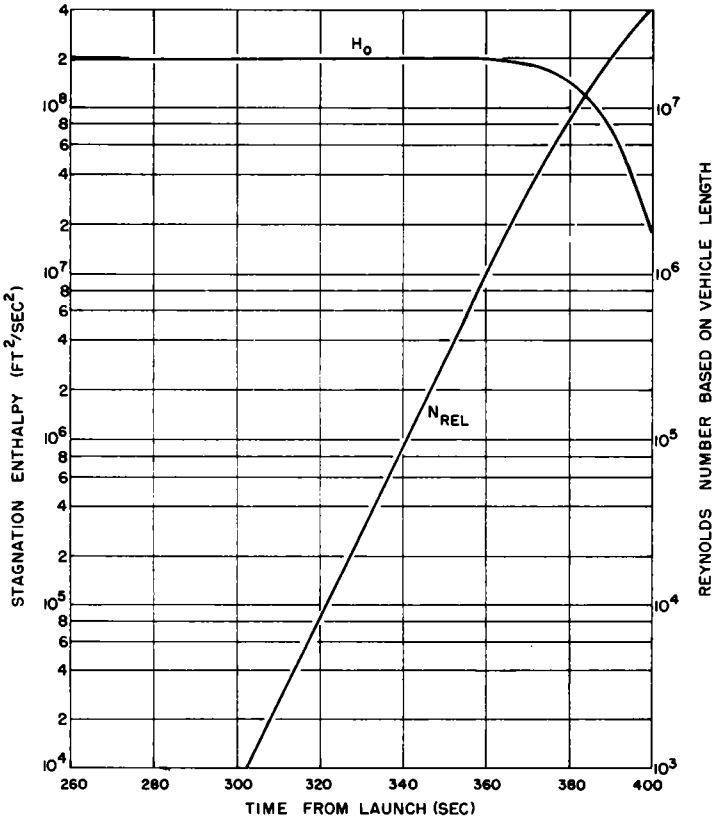

Figure A-8. RFD-1 flight stagnation enthalpy and Reynolds number, based on Trajectory 635

TABLE A-II

Tunnel Conditions

Tunnel Condition	Run No. 96	97	98	100	101	102	103	104	106	107	108	109	110	111	112	113	114	115	116	117	119
Configuration	1	1	1	1	1	3	3	3	2	2	2	2	2	2	2	1	1	1	3	3	3
α(°)	0	0	+4	0	+4	0	0	+4	0	+4	0	0	0	0	0	0	0	0	0	0	0
$N_{ReL} \times 10^{-6}$	1.148	1.293	0.837	0.710	0.598	0.288	0.153	0.302	0.648	1.013	0.953	0.692	1.825	3.580	2.245	4.190	2.942	2.765	0.774	0.725	1.016
Po (psia)	0.525	0.529	0.519	0.425	0.446	0.477	0.456	0.525	0.422	0.543	0.536	0.490	1.594	1.272	1.359	1.414	1.282	1.450	1.382	1.342	1.288
$\dot{q}_o$ (BTU/ft^{2}sec)	59.89	55.59	73.65	65.20	76.61	55.35	77.85	57.75	68.71	68.07	68.95	77.10	140.43	71.83	93.98	65.59	80.00	93.66	83.52	84.19	61.82
$\rho_o \times 10^3$ (atmos)	3.15	3.36	2.68	2.23	2.14	2.93	2.18	3.23	2.13	3.01	2.93	2.41	7.75	10.58	8.82	11.95	9.31	9.02	9.38	8.53	10.77
T_o (°R)	5,580	5,275	6,490	6,380	6,990	5,450	7,005	5,430	6,630	6,040	6,130	6,815	6,890	4,460	5,410	4,120	4,610	5,385	5,080	5,320	4,220
$H_o \times 10^{-8}$ (ft^2/sec^2)	0.405	0.380	0.482	0.473	0.530	0.395	0.532	0.393	0.495	0.443	0.450	0.512	0.515	0.315	0.392	0.289	0.328	0.389	0.365	0.384	0.296
M_∞	19.96	20.13	19.55	19.60	19.13	20.59	19.21	20.05	19.48	19.76	19.61	19.17	17.29	18.41	17.63	18.72	18.65	18.05	18.29	18.15	18.35
V_∞ (ft/sec)	8,943	8,664	9.753	9.659	10,227	8,831	10,250	8,812	9.885	9.358	9.431	10,056	10,065	7,888	8,782	7,551	8.038	8,748	8,478	8,695	7,643
$P_\infty \times 10^4$ (psia)	10.10	10.01	10.39	8.46	9.32	8.62	9.46	10.01	8.50	10.64	10.67	10.21	40.69	32.01	35.24	32.36	28.39	34.13	32.70	31.56	31.00
$\rho_\infty \times 10^4$ (atmos)	4.18	4.49	3.47	2.90	2.71	3.90	2.76	4.31	2.75	3.95	3.84	3.08	9.99	14.49	11.80	16.53	12.71	12.09	12.66	14.85	11.44
T_∞ (°R)	80.7	74.5	100.1	97.7	114.9	74.2	114.7	77.9	103.8	90.4	93.1	111.0	136.2	74.0	100.0	65.4	74.9	94.7	86.6	92.4	69.9

TABLE A-III

Local Model Heating Rates $\dot{q}_m$ (BTU/ft²-sec) and Heating Ratios F_q

Gage No.	96		97		98		100		101		102		103		104		106		107		108	
	$\dot{q}_m$	F_q	$\dot{q}_m$	F_q	$\dot{q}_m$	F_q	$\dot{q}_m$	F_q	$\dot{q}_m$	F_q	$\dot{q}_m$	F_q	$\dot{q}_m$	F_q	$\dot{q}_m$	F_q	$\dot{q}_m$	F_q	$\dot{q}_m$	F_q	$\dot{q}_m$	F_q
1	36.82	3.02	37.54	3.28	46.44	3.08	46.14	3.47	49.22	3.15	62.9	2.78	98.61	3.11	70.2	2.97	-		-		-	
2	Out		41.55	3.63	43.56	2.90	53.84	4.05	44.80	2.86	-		-		-		-		-		-	
3	55.00	4.51	57.17	5.00	73.69	4.90	68.66	5.16	77.86	4.97	-		-		-		-		-		-	
4	1.36	0.111	1.27	0.111	2.079	0.138	1.50	0.113	2.362	0.151	-		-		-		-		-		-	
5	18.25	1.50	22.4	1.96	16.49	1.096	23.70	1.78	14.93	0.955	-		-		-		-		-		-	
6	3.83	0.314	3.55	0.310	3.38	0.225	5.18	0.389	4.038	0.258	-		-		-		15.48	1.106	23.60	1.698	15.00	1.067
7	Out		30.80	2.69	23.07	1.58	32.06	2.41	21.71	1.39	0		-		-		13.07	0.934	19.61	1.412	14.49	1.030
8	2.40	0.197	2.26	0.197	3.120	0.208	2.10	0.158	2.835	0.1805	-		-		-		23.55	1.680	26.15	1.880	25.56	1.817
9	Out		Out		48.78	3.24	41.74	3.14	52.24	3.34	-		-		-		26.14	1.798	29.94	2.154	25.33	1.800
10	Out		5.55	0.485	11.84	0.788	5.61	0.422	11.22	0.718	-		-		-		25.41	1.744	28.89	2.080	23.40	1.662
11	1.14	0.0935	1.10	0.0960	1.763	0.117	1.20	0.0903	1.742	0.1113	-		-		-		0.572	0.0408	1.66	0.1194	1.95	0.1388
12	0.521	0.0428	0.467	0.0418	1.26	0.084	0.459	0.0345	1.128	0.0720	-		-		-		2.18	0.156	Out		0.307	0.0218
13	10.70	0.878	11.89	1.04	5.94	0.395	8.26	0.621	4.010	0.256	-		-		-		4.39	0.314	6.71	0.484	1.50	0.1068
14	1.74	0.143	2.67	0.233	1.34	0.089	1.81	0.136	1.021	0.0653	-		-		-		1.15	0.0822	1.32	0.095	1.24	0.0883
15	Out		0.23	0.0201	0.25	0.0166	Out		Out		-		-		-		0.121	0.00864	Out		Out	
16	1.28	0.105	1.29	0.113	1.78	0.118	1.319	0.0991	1.798	0.115	0.68	0.0301	0.883	0.0278	1.29	0.0546	0.796	0.0568	2.33	0.1680	0.978	0.0695
17	1.06	0.087	1.02	0.0890	2.10	0.140	1.197	0.0900	2.098	0.134	1.55	0.0685	2.142	0.0675	3.15	0.133	0.980	0.0700	2.26	0.1642	1.02	0.0725
18	-		-		-		-		-		0.74	0.0327	0.882	0.0278	1.11	0.0470	-		-		-	
19	-		-		-		-		-		0.46	0.0204	0.753	0.0237	0.871	0.0369	-		-		-	
20	-		-		-		-		-		0.42	0.0186	0.602	0.0190	0.654	0.0277	-		-		-	
21	-		-		-		-		-		1.09	0.0393	1.224	0.0386	1.79	0.0759	-		-		-	
22	-		-		-		-		-		1.09	0.0483	1.431	0.0451	Out		-		-		-	
23	Out		46.10	4.03	45.75	3.04	40.87	3.07	42.21	2.70	-		-		-		30.52	2.18	34.52	2.48	32.27	2.295

TABLE A-III (cont)

Local Model Heating Rates $\dot{q}_m$ (BTU/ft^2-sec) and Heating Ratios F_q

	109		110		111		112		113		114		115		116		117		119	
Gage No.	$\dot{q}_m$	F_q	$\dot{q}_m$	F_q	$\dot{q}_m$	F_q	$\dot{q}_m$	F_q	$\dot{q}_m$	F_q	$\dot{q}_m$	F_q	$\dot{q}_m$	F_q	$\dot{q}_m$	F_q	$\dot{q}_m$	F_q	$\dot{q}_m$	F_q
1	-		-		-		-		38.93	2.90	59.83	3.71	92.27	4.82	123.47	3.62	127.33	3.73	89.49	3.54
2	-		-		-		-		29.05	2.17	38.16	2.37	51.00	2.67	-		-		-	
3	-		-		-		-		65.75	4.90	83.40	5.18	128.18	6.68	-		-		-	
4	-		-		-		-		1.22	0.091	1.31	0.0814	1.92	0.1005	-		-		-	
5	-		-		-		-		26.57	1.98	36.80	2.29	53.03	2.78	-		-		-	
6	16.45	1.100	54.69	1.91	Out		Out		5.19	0.387	5.08	0.316	6.95	0.364	-		-		-	
7	14.00	0.936	40.95	1.73	Out		29.17	1.52	40.56	3.03	48.52	3.01	75.18	3.94	-		-		-	
8	25.28	1.690	59.94	2.10	33.22	2.270	46.33	2.40	5.42	0.404	4.74	0.294	5.92	0.310	-		-		-	
9	28.89	1.931	67.94	2.375	35.82	2.445	46.93	2.44	43.25	3.23	Out		Out		-		-		-	
10	24.01	1.610	60.16	2.105	30.64	2.092	44.42	2.37	9.27	0.692	10.14	0.630	11.10	0.581	-		-		-	
11	1.38	0.0924	2.53	0.0885	1.10	0.075	2.02	0.1053	2.16	0.161	2.20	0.137	2.87	0.150	-		-		-	
12	0.255	0.0171	2.54	0.0889	0.88	0.060	1.56	0.0814	1.27	0.095	1.19	0.074	2.33	0.122	-		-		-	
13	1.96	0.131	Out		4.27	0.291	8.20	0.427	16.76	1.25	18.77	1.17	30.80	1.61	-		-		-	
14	1.18	0.0789	4.05	0.1416	1.36	0.0929	2.54	0.1324	2.46	0.184	2.67	0.166	3.46	0.181	-		-		-	
15	Out		Out		Out		Out		0.16	0.0119	0.164	0.0102	0.26	0.0136	-		-		-	
16	0.968	0.0647	5.09	0.1780	2.40	0.164	2.85	0.1484	2.19	0.163	2.21	0.137	2.85	0.149	3.30	0.0966	3.26	0.0950	2.60	0.103
17	1.13	0.0755	3.30	0.1152	1.98	0.134	2.40	0.1250	1.50	0.112	1.79	0.11	2.18	0.114	Out		Out		Out	
18	-		-		-		-		-		-		-		1.62	0.0474	1.62	0.0472	1.47	0.0583
19	-		-		-		-		-		-		-		1.24	0.0363	1.33	0.0388	1.07	0.0424
20	-		-		-		-		-		-		-		0.61	0.0179	0.67	0.0195	0.55	0.0218
21	-		-		-		-		-		-		-		1.46	0.0427	2.09	0.0609	1.75	0.0694
22	-		-		-		-		-		-		-		2.08	0.0609	2.24	0.0652	1.97	0.0781
23	33.28	2.225	53.60	1.874	35.42	2.42	40.74	2.12	Out		Out		Out		-		-		-	

TABLE A-IV

Local Model Pressures P_m (psia)

Gage No.	Run No. 96	97	98	100	101	102	103	104	106	107	108	109	110	111	112	113	114	115	116	117	119
1	0.573	0.567	0.560	0.478	0.477	0.510	0.492	0.682	-	-	-	-	-	-	-	1.496	1.337	1.468	1.383	1.352	1.490
2	0.419	0.444	0.500	0.313	0.401	-	-	-	-	-	-	-	-	-	-	Out	Out	1.181	-	-	-
3	0.126	0.155	0.154	0.126	0.142	-	-	-	-	-	-	-	-	-	-	0.621	0.460	0.531	-	-	-
4	-	-	-	-	-	-	-	-	Out	0.581	0.572	0.494	1.545	1.233	1.317	-	-	-	-	-	-
5	-	-	-	-	-	-	-	-	0.433	0.581	0.569	0.498	1.602	1.244	1.340	-	-	-	-	-	-
6	-	-	-	-	-	-	-	-	0.436	0.567	0.565	0.497	1.548	1.150	1.256	-	-	-	-	-	-
7	-	-	-	-	-	-	-	-	0.450	0.574	0.581	0.501	1.602	1.238	1.350	-	-	-	-	-	-
8	-	-	-	-	-	-	-	-	0.434	0.568	0.558	0.480	1.617	1.192	1.330	-	-	-	-	-	-
9	-	-	-	-	-	-	-	-	0.427	0.547	0.554	0.483	1.553	1.186	1.273	-	-	-	-	-	-
10	-	-	-	-	-	-	-	-	0.427	0.581	0.552	0.477	1.560	1.193	1.323	-	-	-	-	-	-
11	-	-	-	-	-	-	-	-	Out	0.547	0.563	0.499	1.674	1.223	1.379	-	-	-	-	-	-
12	-	-	-	-	-	-	-	-	0.436	0.554	0.566	0.475	1.509	1.189	1.299	-	-	-	-	-	-
13	-	-	-	-	-	-	-	-	0.450	0.559	0.572	0.498	1.540	1.208	1.333	-	-	-	-	-	-
14	0.0193	0.0207	0.0190	0.0180	0.058	-	-	-	0.0117	0.0027	Out	0.00158	0.0416	0.0318	0.0373	0.0610	0.0560	0.0596	-	-	-
15	0.0543	0.0355	0.0344	0.0302	0.0373	-	-	-	0.0471	0.0296	0.0606	0.0522	Out	0.156	0.122	Out	0.0561	0.0818	-	-	-
16	0.0535	0.0634	0.0619	0.0314	0.0450	-	-	-	0.0589	0.105	0.0548	0.0471	0.262	0.212	0.675	0.107	0.1110	0.1460	-	-	-
17	0.0186	0.0137	0.0195	0.0158	0.0154	0.0130	0.0129	0.0152	0.0213	0.0318	0.0276	0.0234	0.0792	0.0614	0.0666	0.0549	0.0525	0.0554	0.0371	0.0340	0.0313
18	0.0177	0.0153	0.0196	0.0147	0.0166	0.0165	0.0126	0.0124	0.0181	0.0215	0.0223	0.0208	0.0710	0.0550	0.0524	0.0515	0.0496	0.0547	0.0772	0.0793	0.0705
19	-	-	-	-	-	0.0213	0.0216	0.0258	-	-	-	-	-	-	-	-	-	-	0.0310	0.0294	0.0276
20	-	-	-	-	-	0.0041	0.00415	0.00521	-	-	-	-	-	-	-	-	-	-	0.0132	0.0121	0.0109
21	-	-	-	-	-	0.0029	0.00235	0.00345	-	-	-	-	-	-	-	-	-	-	0.0100	0.0074	0.00901
22	-	-	-	-	-	0.0061	0.00532	0.00882	-	-	-	-	-	-	-	-	-	-	0.0198	0.0170	0.0173
23	-	-	-	-	-	0.0109	0.00918	0.0122	-	-	-	-	-	-	-	-	-	-	0.0411	0.0369	0.0370

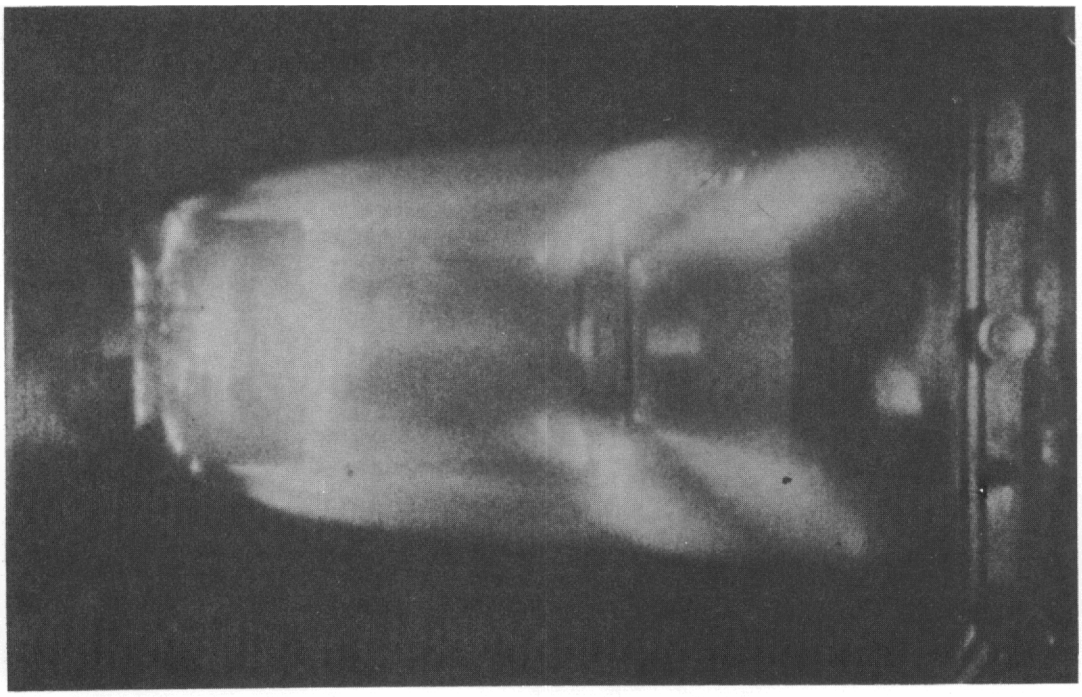

Figure A-9. Configuration 1 during wind-tunnel test

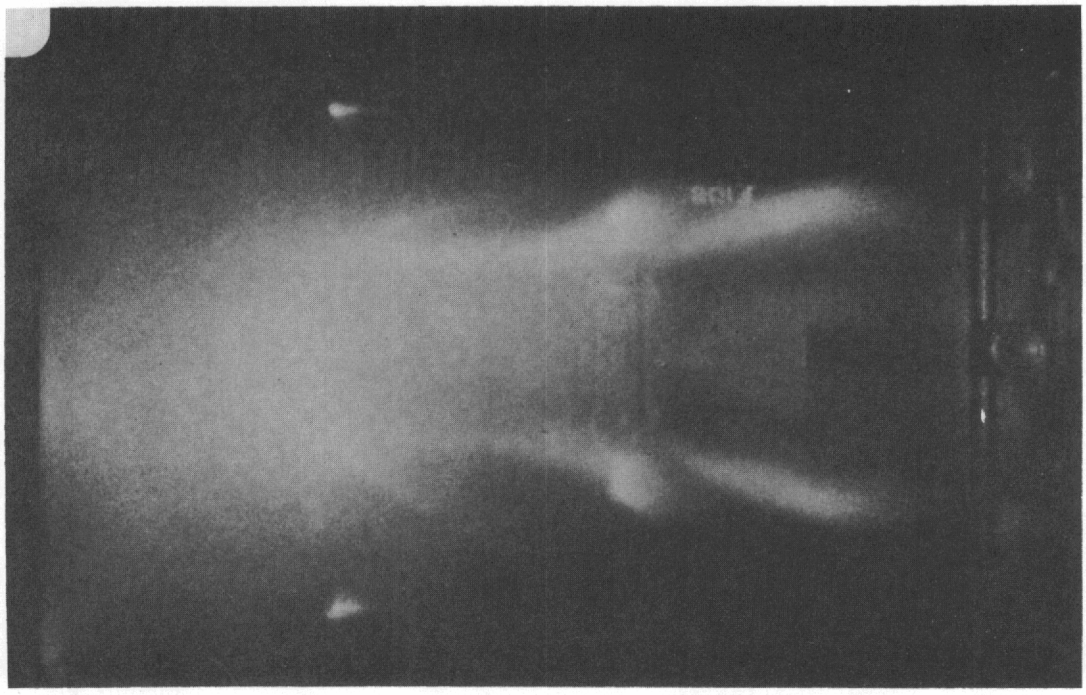

Figure A-10. Configuration 2 during wind-tunnel test

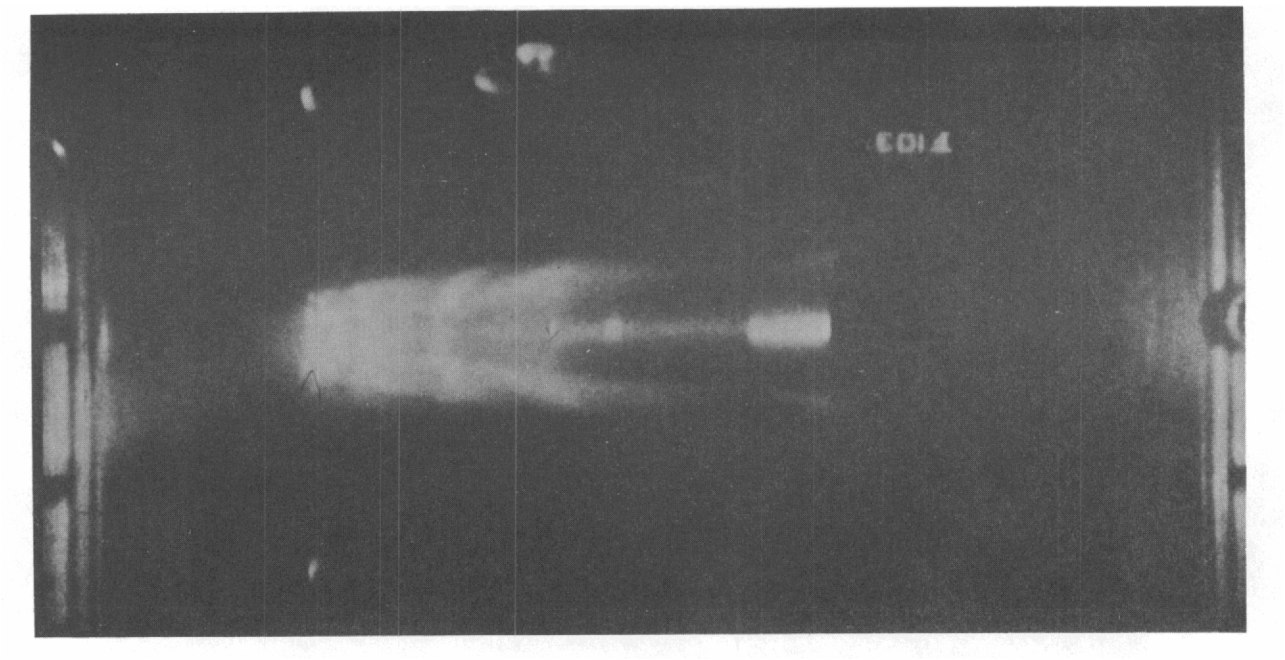

Figure A-11. Configuration 3 during wind-tunnel test

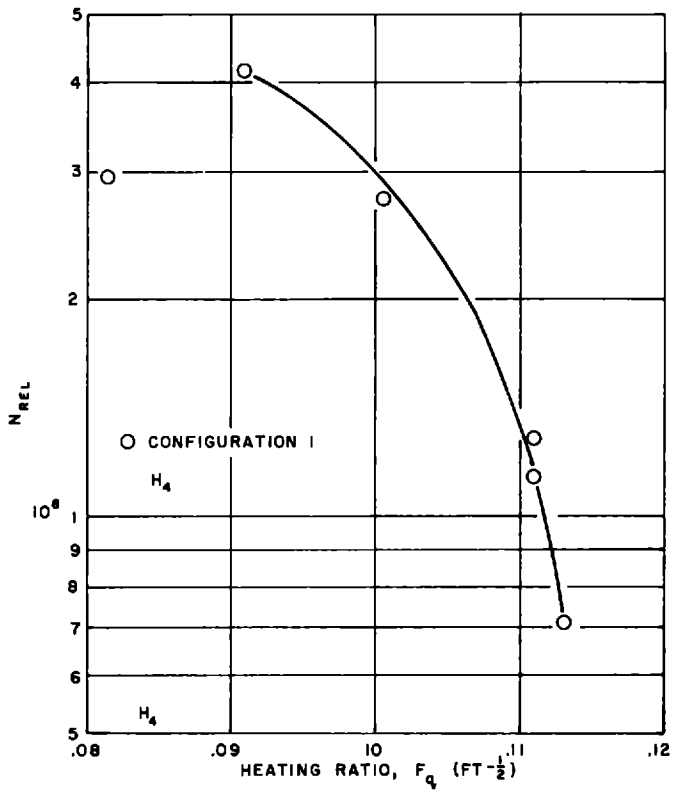

Figure A-12. Effect of Reynolds number on heating ratios in a separated-flow area (the side of the fins)

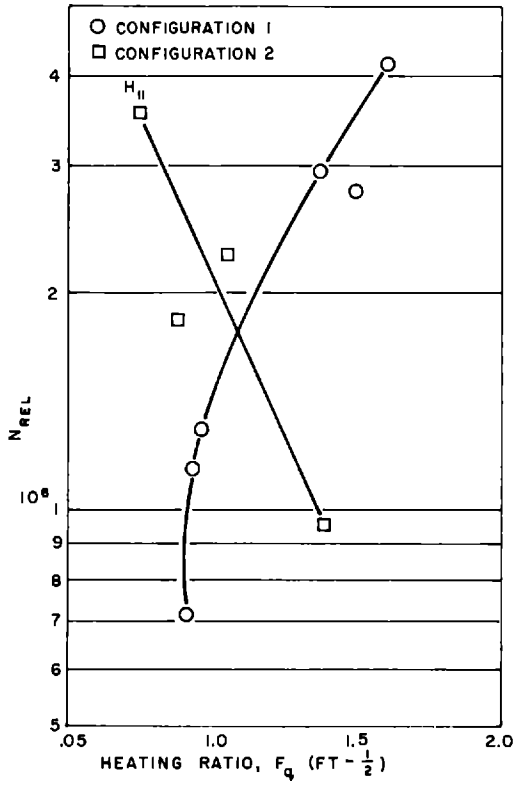

Figure A-13. Effects of Reynolds number and configuration on heating ratios (forward part of the core-vessel walls)

In unrestricted, attached-flow regions with no shock-wave/boundary-layer interactions, the heating ratios were found to increase by as much as a factor of 5 from Reynolds numbers of 5×10^3 to 3×10^5 based on scaled vehicle length. This increase was found on all three configurations and was due to transition from laminar to turbulent flow. While transition does not usually take place at this low a Reynolds number, the irregular shape of the reactor breaks up the laminar boundary layer. With this boundary-layer trip at the front of the vehicle, transition takes place over the entire vehicle at the same time. Heating ratios on the RV cone, shown in Figure A-14, are typical of those found in attached-flow areas.

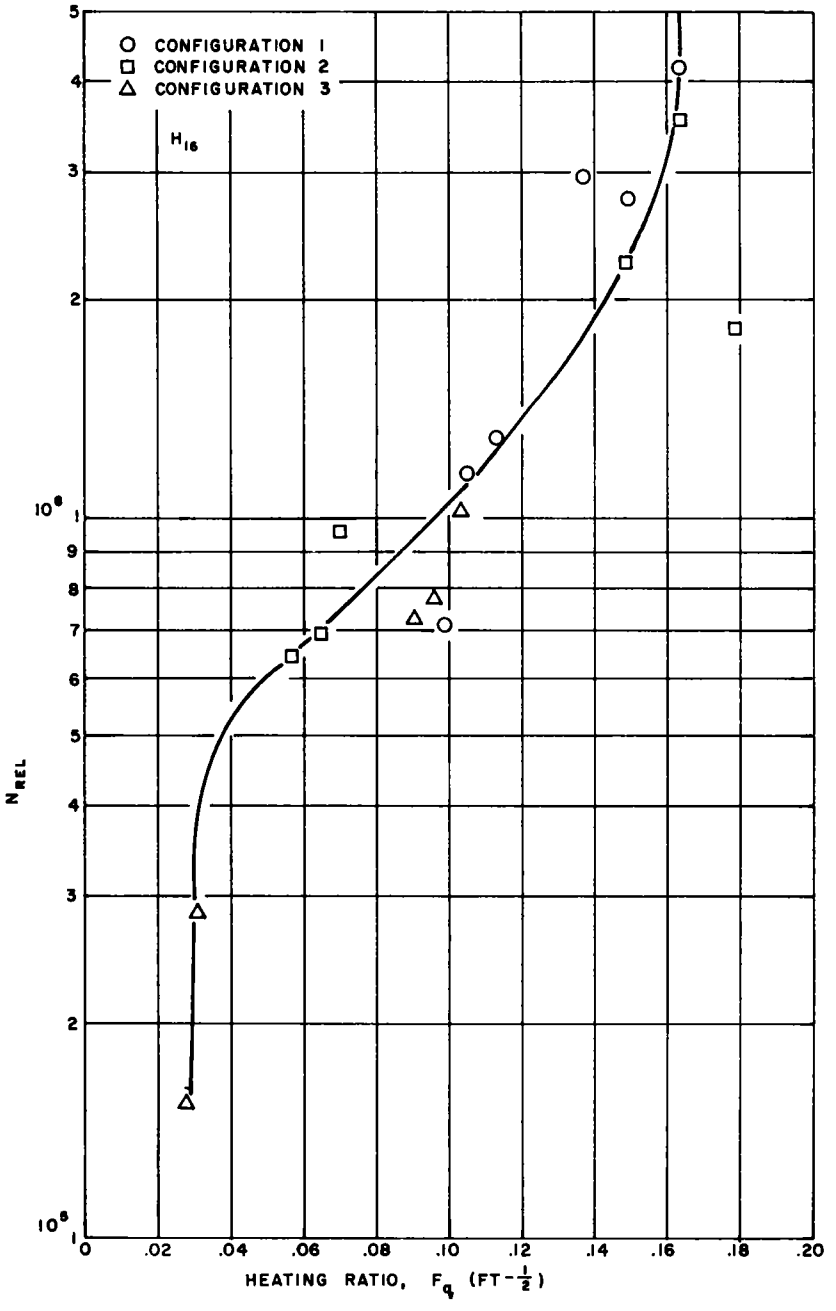

Figure A-14. Heating ratios on the RV cone

The increased heating effects of shock-wave/boundary-layer interactions can be seen in Figures A-15 and A-16. In both cases, shock waves from the pump and fins on Configuration 1 caused higher heating rates than were experienced in the same areas of the core-vessel cover when the pump was removed (Configuration 2). There were severe heating-rate gradients in the area of H_6 shown in Figure A-16; these were caused by multiple shock-wave interactions, which accounts for the unusual amount of data scatter. These hot spots and gradients could not be located with a limited number of discrete heat meters, as used in the AEDC tests, but were found in the postflight test series at Rhodes and Bloxsom, where heat rates were found with a heat-sensitive paint. This test series is described in Appendix B.

In Configuration 1, several areas of the core vessel were protected by the NaK pump, the NaK tubes, and the fins. The heating ratios increased greatly in these areas when the pump was removed, as shown in Figures A-17, A-18, and A-19. Data plotted in Figures A-12 through A-19 are for zero-angle-of-attack runs only.

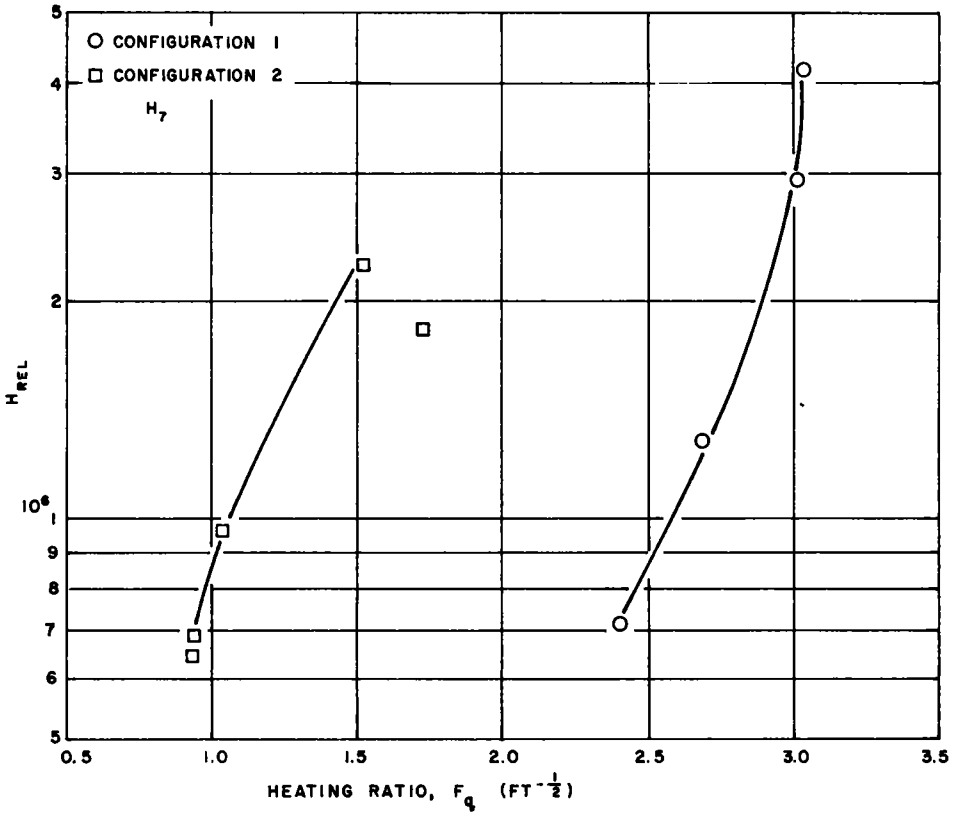

Figure A-15. Increased heating effects of shock-wave/boundary-layer interactions

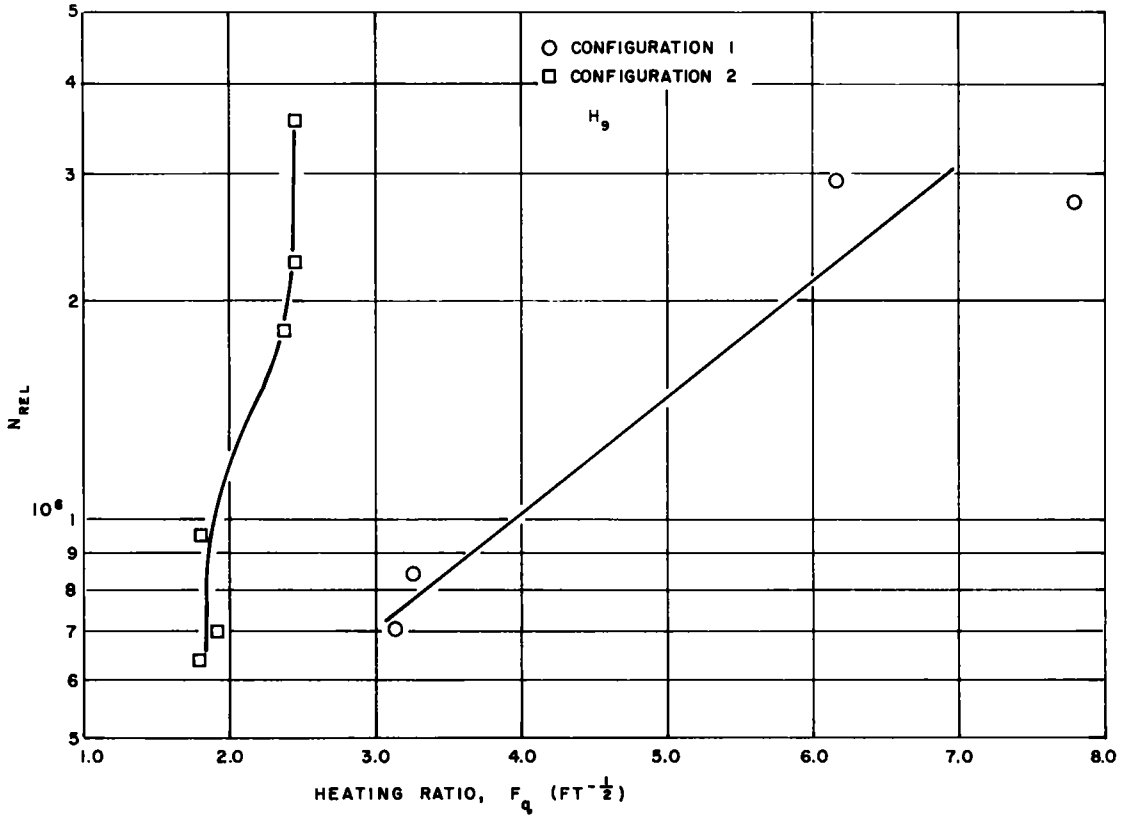

Figure A-16. Increased heating effects of shock-wave/boundary-layer interactions, showing severe heating-rate gradients caused by multiple shock-wave interactions

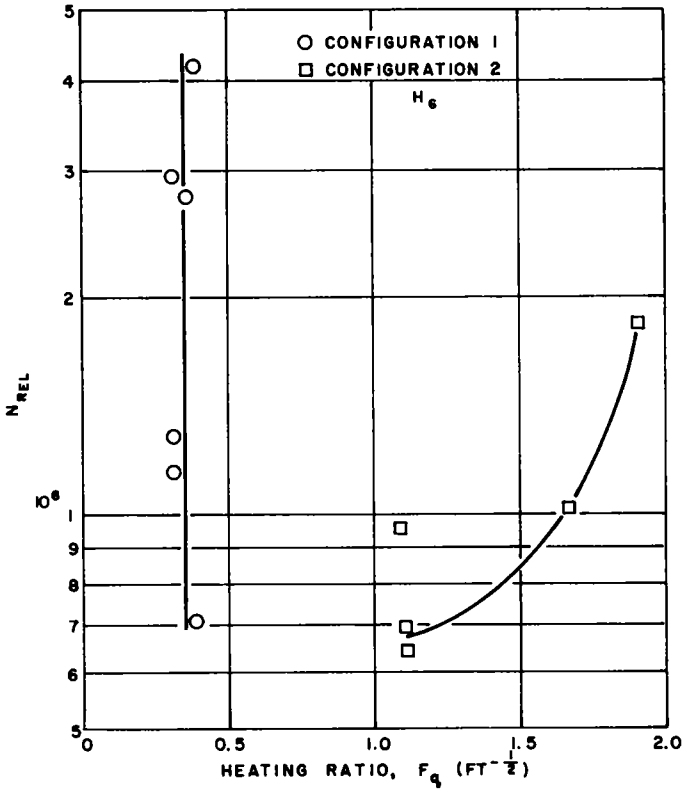

Figure A-17.

Increase in heating ratios on the core vessel caused by removal of the NaK pump

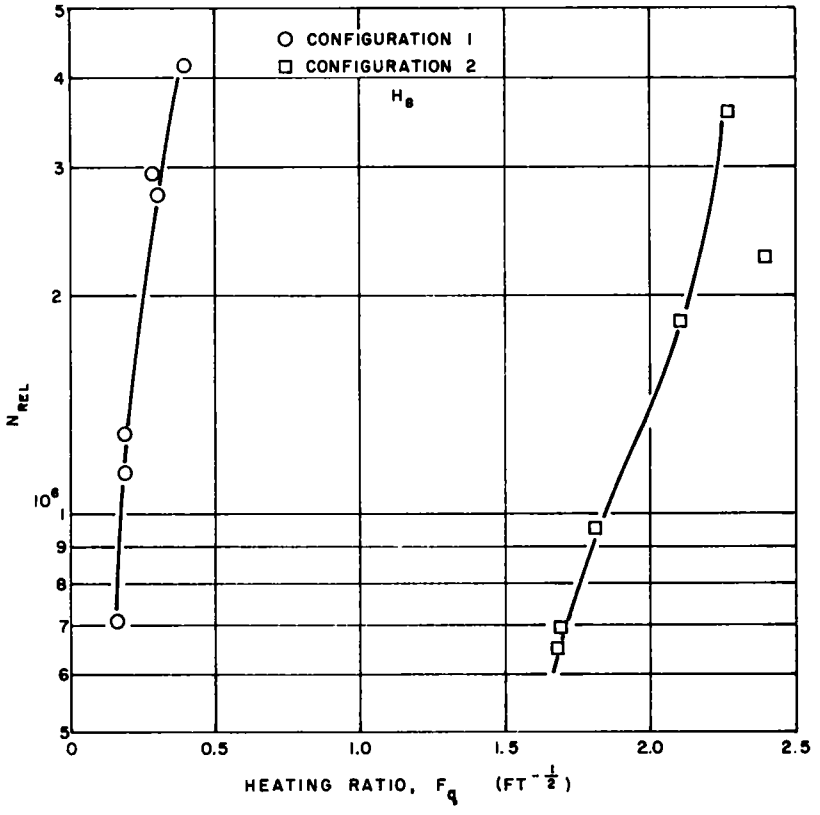

Figure A-18.

Increase in heating ratios on the core vessel caused by removal of the NaK tube

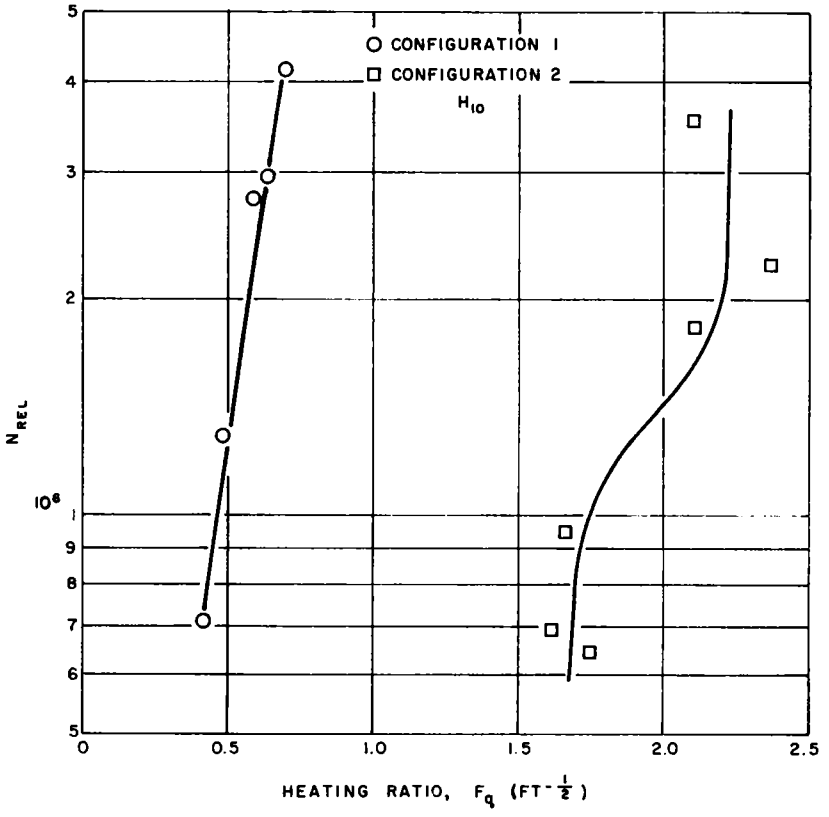

Figure A-19.

Increase in heating ratios on the core vessel caused by removal of the NaK-pump fins

APPENDIX B

Postflight Aeroheating Wind-Tunnel Tests

Notation:

Y = film thickness (Å)

μ = film index of refraction

λ = light wavelength (Å)

C_L = local color number on model

C_{ss} stagnation color number on the tunnel calibration sphere

$F_q = \dot{q}_L/\dot{q}_S \sqrt{R}$ ($ft^{-1/2}$)

$\dot{q}_L$ = local heating on the flight vehicle (BTU/ft^2-sec)

$\dot{q}_S\sqrt{R}$ stagnation heating on 1-foot radius sphere ($BTU/ft^{3/2}$-sec)

α = angle of attack (°)

H_S = stagnation enthalpy (ft^2/sec^2 or ft-lb/slug)

M = Mach number

N_{ReL} = Reynolds number based on scaled vehicle length

x = distance along vehicle surface (ft)

δ = boundary layer thickness (ft)

APPENDIX B

Postflight Aeroheating Wind-Tunnel Tests

After the RFD-1 flight, a series of seven aeroheating tests were conducted in the 60-inch Rhodes and Bloxsom hot-shot tunnel. The primary purposes of these tests were:

1. To investigate heating rates in the RV at the angles of attack experienced during the flight, which were higher than those investigated in the preflight AEDC tests.

2. To determine to what extent hot spots on the RV caused by the flow over the reactor increased the overall heating to the rotating RV.

In addition, a limited amount of data were obtained on reactor heating rates.

The 60-inch hot-shot tunnel operates by discharging a 100,000-joule capacitor bank into a pressurized air chamber; the chamber pressure then ruptures a Mylar diaphram, allowing the high-temperature, high-pressure air to expand through a nozzle into an evacuated test chamber. Mach number, Reynolds number, and stagnation enthalpy are controlled by varying throat and nozzle diameters, initial chamber pressure, and electrical power input. Run time varies from 0.1 to 10 milliseconds, depending on chamber conditions.

Heating rates are determined by apparent discoloration of a black lacquer applied to a calibration sphere and the model. During the test, a clear film is formed at the outer surface of the paint. The reaction depth and hence the film thickness is proportional to the heat input. When a light beam from a normal angle of incidence is shown on this film, selective interference and reinforcement of various wavelengths of light result in the surface appearing to be any of the colors of the visible spectrum, from violet to red, depending on the film thickness. This is in accordance with interference theory of thin films.[3] Considering the phase change at the outer film surface, the series of reinforcement colors is obtained by film thicknesses $Y = n\lambda/4\mu$ for all odd integers of n except 1. For $n = 1$, no light is reflected due to the lack of interference of colors not reinforced. Film thicknesses through the ranges of $n = 3$ and 5 are readable. Heating rates which would cause thicker films ablate the surface of the paint. Colors from the $N = 5$ series can be distinguished from the $n = 3$ series by their deeper colors, as shown in Figure B-1. The color numbers can be normalized by considering silver, which is the color corresponding to the lowest readable heating rate, equal to 1 by the following equation:

$$\text{Color No.} = \frac{\dot{q}}{\dot{q}_{\text{silver}}} = 1.30 \times 10^{-3} \frac{n\lambda}{4\mu} - 3.0.$$

Film thicknesses of less than 3000 Å may be read by using oblique reading angles. When this is done, the transition from black to a light silver corresponds to a color number of 0.5. This method of determining heating rates by measuring integrated local heating during a run is valid only because of the small amount of heating during startup and shutdown of this tunnel.

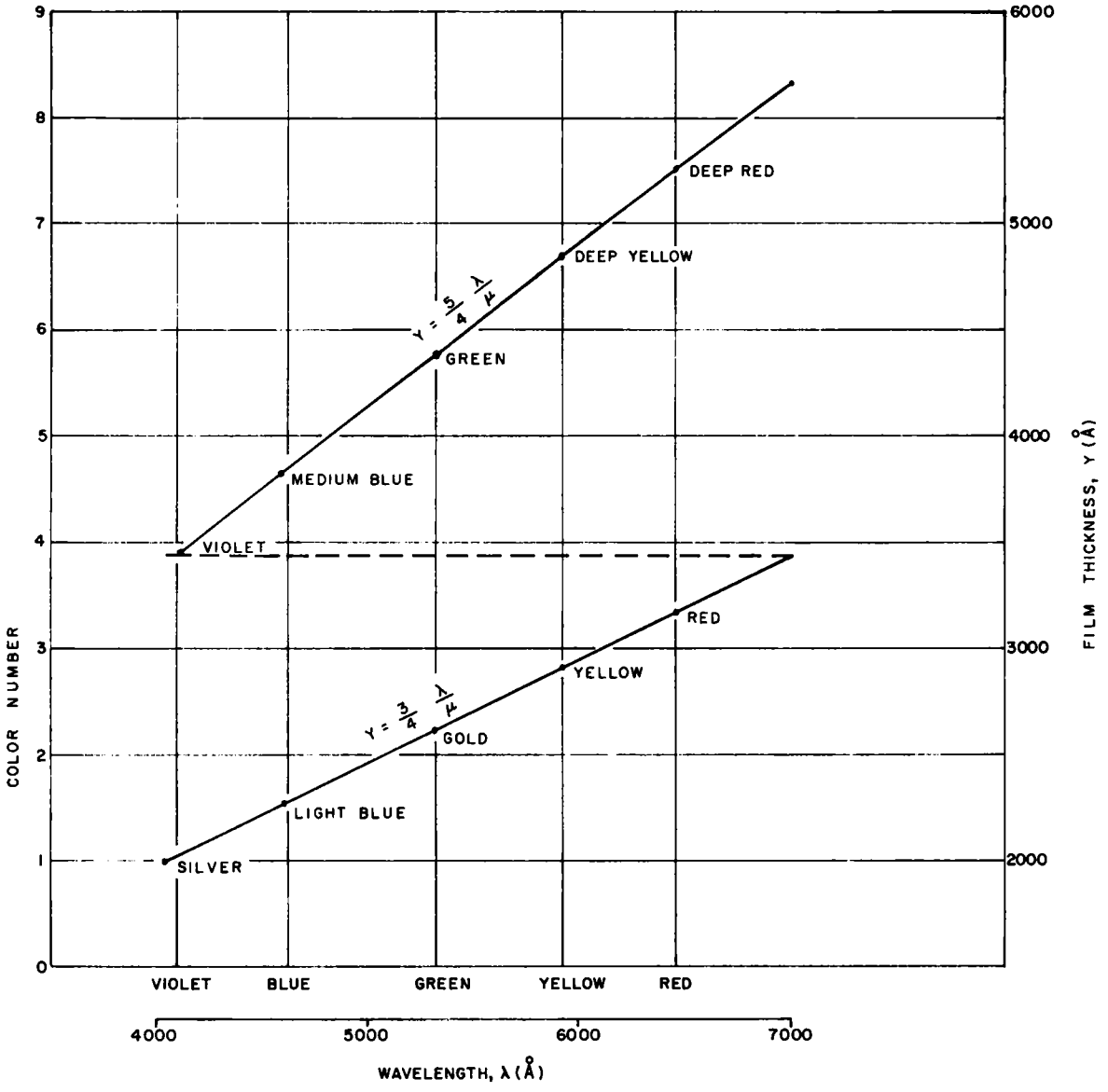

Figure B-1. Apparent color of test lacquer as a function of film thickness

With the color numbers normalized, the ratio of local heating on the flight vehicle to stagnation heating on a 1-foot-radius sphere can be found by:

$$F_q = \frac{C_L \sqrt{\text{Model scaling factor}}}{C_{ss} \sqrt{\text{Radius of calibration sphere (ft)}}}$$

The tests were conducted with the same quarter-scale model described in Appendix A. Test conditions are defined in Table B-1. Times for corresponding flight conditions are based on Trajectory 635.

TABLE B-I

Conditions for Tests in the Rhodes and Bloxsom 60-Inch Hot-Shot Tunnel

Test No.	Configuration	α (deg)	H_s (ft^2/sec^2)	M	N_{ReL}	Time from Launch (sec)
1	RS	0	0.684×10^8	11.7	4.15×10^5	-
2	RS	30	2.04×10^8	19.0	1.24×10^5	344
3	RS	15	2.04×10^8	19.0	1.24×10^5	344
4	RS	0	2.04×10^8	19.0	1.24×10^5	344
5	RS less pump and hinge brackets	15	1.96×10^8	18.2	1.00×10^6	364
6	RS less pump and hinge brackets	0	1.96×10^8	18.2	1.00×10^6	364
7	RV with reactor base	0	1.64×10^8	9.4	4.00×10^6	378

Run No. 1 -- This run was made at reduced enthalpy to match a set of test conditions during one of the preflight AEDC tests. Mach number was not matched exactly, but since it was still in the hypersonic range, this should not have affected the results significantly. The purpose of this test was to correlate the results of the two tunnels. With the exception of a few locations where heating rates varied by as much as a factor of 2.4 across the AEDC heat meters, correlation was well within experimental error.

Other than Run No. 7, where Mach number was slightly low, the remainder of the tests matched all the prescribed flight conditions. All of the complex heating contours cannot be presented in this report, but significant findings for each test are summarized. Details of local heating rates are given in the final Rhodes and Bloxsom report.[4] For Runs No. 2 through 6, the boundary-layer growth over the cylindrical portion of the RV, δ/x was proportional to $N_{Re}^{1/2}$, indicating laminar flow. For Run No. 7, δ/x was proportional to $N_{Re}^{1/5}$, indicating transition to turbulent flow. This transition was also substantiated by increased heating rates.

Run No. 2 -- At a 30-degree angle of the attack, the only hot spots on the RV other than those caused by the high heating rates on the leading surfaces were behind the hinge hardware, causing local heating rates to increase by a factor of 3.3. Areas on the core-vessel sides behind the fins received 3.1 times the heat of the surrounding area. These areas of high heating were caused by flow disturbances and vortices from reactor protuberances. Heating ratios on the side of the fins varied by a factor of 2.8 over the surface. Other local increases in heating, up to a factor of 6, were caused by shock-wave/boundary-layer interactions, and were found between the switches on the transverse NaK tube, and on the leading edges of the fins, pump, and core-vessel cover.

Run No. 3 -- At a 15-degree angle of attack, heating rates on the RV cone and cylinder were higher than on Run No. 2 due to more disturbances from the fins and hinge hardware impinging on the RV. Hot spots on the reactor were similar to those on Run No. 2, but were in different locations.

Run No. 4 -- At a zero-degree angle of attack, heat was substantially reduced on the RV cylinder because no disturbances from the reactor contacted this area. However, hot spots 5.6 times hotter than the surrounding area appeared behind the fins on the flare. Average heating on the conical section increased slightly because the boundary layer was disturbed all the way around and not only on the leading spots. Hot spots on the reactor covered smaller areas but were more intense than on the angle-of-attack runs. No hot spots appeared on surfaces parallel to the flow. Figures B-2 and B-3 show some of the heat distributions. Although no colors are shown, the limits of the readable range on surfaces nearly perpendicular

to the camera appear as the light areas in the photos. The small, dark, dull areas are where the paint has ablated, corresponding to color numbers greater than 8. Unreacted paint appears medium dark and is less dull. This corresponds to color numbers less than 1.

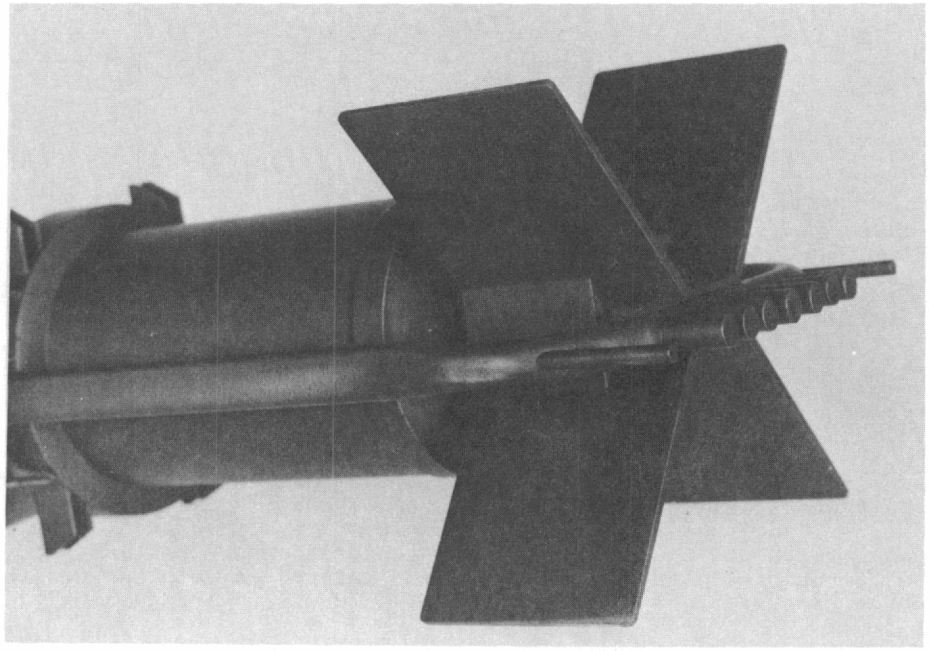

Figure B-2. Heat distribution on sides of reactor, Run No. 4

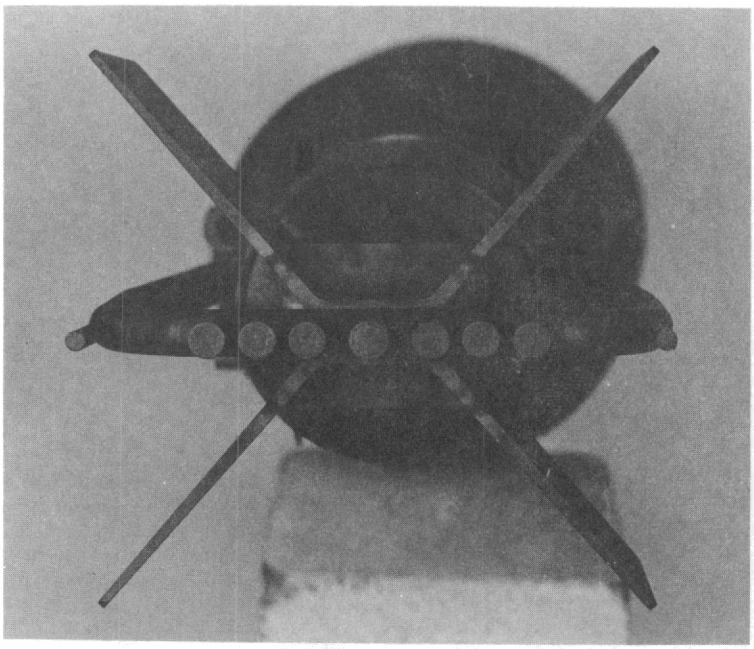

Figure B-3. Heat distribution on front of reactor, Run No. 4

Run No. 5 -- With the pump and hinge brackets removed, the only flow disturbances from the reactor core vessel at a 15-degree angle of attack appear on the aft part of the RV cone.

Runs No. 6 and 7 -- At a zero-degree angle of attack, flow was symmetrical, with no hot spots, either with or without the core vessel on the RV.

The hot spots observed on the RV which were caused primarily by the NaK pump and the hinge hardware were present for only a small fraction of the RFD-1 re-entry, and their relative position on the RV changed with angle of attack and rotation angle. Although these hot spots increased the overall heating to the RV slightly, they should not have caused local failures. The small hot spots on the reactor caused some errors in the reactor-burnup analysis, since not enough tunnel data were available to define their locations at each angle of attack and rotation angle.

When the Rhodes and Bloxsom tunnel was operated at flight enthalpy, the ratios of local to stagnation heat rates on the RV were found to be higher than those from the AEDC tests by approximately the square root of the enthalpy ratios. Due to the large gradients in the heating ratio on the reactor, it was difficult to correlate all the data from the two tunnels, but in almost all cases higher ratios were obtained in the Rhodes and Bloxsom tunnel.

APPENDIX C

Trajectory and Aeroheating Computer Program

APPENDIX C

Trajectory and Aeroheating Computer Program

The TTA computer program used to calculate the RFD-1 trajectory and stagnation-point heating is discussed below. A detailed description of the program is presented in Reference 5, and a more complete summary of the trajectory part of the program is given in Appendix C of SC-RR-64-510.

Trajectories are calculated relative to an oblate spheroidal model of the earth. An oblate spherical gravitational field is used, and the effect of the earth's rotation is included. Trajectories may be calculated for either a point mass or a 6-degree-of-freedom rigid body. In either case, drag, thrust, and weight may vary throughout re-entry.

Inputs to the program are:

1. Initial vehicle position: geodetic latitude, longitude, and altitude.
2. Initial heading: re-entry angle and angle of the velocity vector relative to east.
3. Initial velocity.
4. Ballistic coefficient (W/C_DA) as a function of any other program parameter.
5. Initial time and time increments.
6. Which of the approximately 350 computed quantities are to be printed out.

The quantities most generally selected for printout on the RFD-1 program were:

1. Relative velocity
2. Mach number
3. Position
4. Acceleration
5. Heading
6. Range
7. Dynamic pressure
8. Drag
9. Observed and actual azimuth, elevation, and slant range between any fixed or moving observation point and the re-entry vehicle
10. Stagnation-point convective and radiative aerodynamic heating rates to a 1-foot-radius sphere in continuum flow
11. Integrated stagnation aerodynamic heating to a 1-foot-radius sphere.

The subprogram used to calculate aeroheating employs the following equations, based on methods described in References 6 and 7. These equations assume continuum flow and take into account the effects of ionization and dissociation. At velocities below 25,000 ft/sec, only the convective part of the subprogram is used.

The convective heating rate $\left(\dot{q}_c\right)$ is defined by:

$$\dot{q}_c = \frac{17,600}{\sqrt{R}} \left(\frac{\rho_\infty}{\rho_s}\right)^{0.5} \left(\frac{V_\infty}{V_c}\right)^{3.25}, \frac{BTU}{Ft^2\text{-sec}}$$

where,

R nose radius, ft

ρ_∞/ρ_s the ratio of local free-stream density to density at sea level

V_∞ vehicle velocity, ft/sec

V_c $\sqrt{gr}$, the circular orbital velocity, ft/sec.

The convective heat input $\left(\dot{Q}_c\right)$ is defined by:

$$\dot{Q}_c = \int \dot{q}_c \, dt + \dot{Q}_{co}.$$

The radiator-heat heating rate $\left(\dot{q}_r\right)$ is defined by:

$$\dot{q}_r = AR\left(\frac{\rho_\infty}{\rho_s}\right)^{1.22} \left(\frac{V_\infty}{10^4}\right)^B, \frac{BTU}{Ft^2\text{-sec}}$$

where,

A = 0	B = 0	when		$V_\infty < 25,000$
A = 6.8	B = 12.5	when	$25,000 \leq$	$V_\infty < 30,000$
A = 0.003	B = 19.5	when	$30,000 \leq$	$V_\infty < 35,000$
A = 20.4	B = 12.5	when	$35,000 \leq$	V_∞

The radiative heat input $\left(\dot{Q}_r\right)$ is defined by:

$$\dot{Q}_r = \int \dot{q}_r \, dt + \dot{Q}_{ro}.$$

APPENDIX D

Thermalog Program

Notation:

X = length

T = temperature

t = time

ρ = density of the material

K = thermal conductivity of the material

C_p = specific heat of the material

V = voltage

R = resistance per unit length

R_T = thermal resistance

C = capacitance per unit length

C_T = thermal capacitance

A = area normal to heat flow

h_C = convective heat-transfer coefficient

R_c = resistance to convective heat transfer at surface

R_R = resistance to radiation heat transfer at the surface

σ = Stefan-Boltzmann constant

F_{12} = geometric form factor between Surface 1 and 2

APPENDIX D

Thermalog Program

Melting and ablation studies were conducted with the aid of the Sandia Thermalog, which utilizes a one-dimensional, passive, electric-analog representation of heat conduction. The phase-change processes are represented electrically by biased Zener diodes with current integrators. Resultant mass removal is accomplished in discretized steps or nodes. Radiation losses at the surface are included in the analog. The one-dimensional conduction network is constructed by using the procedures outlined in Reference 2.

The thermal-diffusion equation has the form

$$\Delta^2 T = \frac{\rho C_p}{K} \frac{\delta_T}{\delta_t} .$$

This equation is analogous to the electrical-diffusion equation

$$\Delta^2 V = RC \frac{\delta_V}{\delta_t} .$$

It is now reasonable to assume that an electrical network can be set up such that $RC = \rho C_p/K$. If boundary conditions can also be matched, it becomes obvious that the solution of the electrical-diffusion equation is also the solution to the thermal-diffusion equation.

For one-dimensional heat transfer, the equation becomes

$$\frac{\delta^2 T}{\delta X^2} = \frac{C_p \rho}{K} \frac{\delta_T}{\delta_t} .$$

The following circuit represents the one-dimensional electrical-diffusion equation for an incremental length of ΔX.

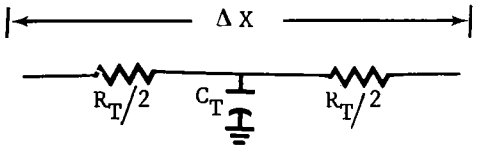

Therefore

$$RC = \frac{R_T C_T}{(\Delta X)^2} = \frac{\rho C_p}{K}$$

$$R_T C_T = \left(\rho C_p A \Delta X\right)\left(\frac{\Delta X}{A K}\right)$$

$$R_T = \frac{\Delta X}{A K}, \quad C_T = \rho C_p A \Delta X.$$

Now, a network can be constructed of resistors and capacitors which have values equal to the thermal resistance and capacitance of each ΔX increment in the heat-conducting material.

At the surface of the heat-conducting material, the heat-flow resistance due to the convection process is

$$\frac{1}{A h_c} = R_c \ .$$

For radiation heat-transfer between two surfaces at T_1 and T_2, the resistance can be expressed as

$$R_R = \frac{1}{\sigma A_1 F_{12} (T_1 + T_2)(T_1^2 + T_2^2)} \ .$$

This expression is subject to the usual gray-body assumptions.

APPENDIX E

The "Herman" Heat-Transfer Program

APPENDIX E

The "Herman" Heat-Transfer Program

This program for the CDC 1604 digital computer is used for transient thermal analysis of composite structures with radiation from the surface and heat input from convection or internal generation. The thermal-diffusion equation is solved by dividing the conducting material into a finite number of segments or nodes in such a manner that the behavior of the thermal parameters can be described by average values. The thermal behavior of the node can then be described by the following system of ordinary differential equations:

$$C_{po}\rho_o V_o \frac{dT_o}{dt} = \sum \frac{K_i S_i}{\Delta X_i}\left(T_i - T_o\right) + \sum f_i \sigma \epsilon_i A_i \left(T_i^4 - T_o^4\right) + Q_o$$

where

C_{po} = specific heat of node o

ρ_o = density of node o

V_o = volume of node o

T_o = temperature of node o

T_i = temperature of node i

K_i = thermal conductivity between nodes o and i

S_i = area between nodes o and i

X_i = a distance such that $(T_i - T_o)/\Delta X_i$ is an approximation to $\delta T/\delta X$ in the direction normal to the surface between nodes o and i

A_i = area of a surface which is receiving radiation of effective temperature T_i

ϵ_i = emissivity of A_i

f_i = form factor of A_i

σ = Stefan-Boltzmann constant

Q_o = heat input to node o

The term on the left represents the heat stored on node o. On the right, the first term represents the heat received by conduction, the second term represents the heat received by radiation, and the third term represents the heat received by internal generation or convection.

LIST OF REFERENCES

1. Oppenheim, A. K., "Generalized Theory of Convective Heat Transfer in a Free-Molecule Flow," J. Aeronaut, Sci., 20:1 (1953).

2. Larson, H. T., Heat Transfer in Separated Flows, IAS-59-37 (1959).

3. Hausmann & Slack, Physics, D. Van Nostrand Co., New York, 3rd ed. (1948).

4. Bloxsom, D., Heat Transfer Testing on Sandia Model RFD-1, SNAP-10A System, August 23, 1963.

5. Allensworth, J. A. F., The TTA Generalized Rigid Body Theoretical Trajectory Program for Digital Computer, SC-TM-64-526.

6. Chapman, D. R., An Approximate Analytical Method for Studying Entry into Planatary Atmospheres, NASA TR R-11 (1959).

7. Lovelace, U. M., Charts Depicting Kinematic and Heating Parameters for a Ballistic Re-entry at Speeds of 26,000 to 45,000 Feet per Second, NASA TN D-968 (1961).

8. Class, P. L., Thermolog, A Passive Network Analog Computer for the Solution of Transient Heating Problems, SCTM 264-62(71) (1963).

9. Wolney, W., Heat Transfer and Pressure Measurements on the Full-Scale SNAP 2-10A at M = 19, AEDC-TDR-63-84 (1963).

10. Memo, Klett, R. D., to Clark, A. J., Jr., "Ablation and Burnup Analysis of the RFD-1 Re-entry System," April 16, 1963.

11. Memo, Pousma, J. G. to Clark, A. J., Jr., "Temperature Test of Retainer Band on SNAP-10A Reactor," May 23, 1963.

DISTRIBUTION:
TID-4500 (32nd Ed.), UC-36 (476)
J. A. Lieberman, Assistant Director for Nuclear Safety, Division of Reactor Development, USAEC, Washington 25, D. C.
F. K. Pittman, Director, Division of Reactor Development, USAEC, Washington 25, D.C.
H. G. Hembree, Safety Engineering & Test Branch, Division of Reactor Development, USAEC, Washington 25, D. C.
Lt. Col. W. K. Kern, Aerospace Safety Section, Engineering & Test Branch, Division of Reactor Development, USAEC, Washington 25, D. C. (6)
R. L. Kirk, SNAP Program Director, Division of Reactor Development, USAEC, Washington 25, D. C.
Robert Lowenstein, Director, Division of Licensing & Regulation, USAEC, Washington 25, D. C.
Brig. Gen. D. L. Crowson, USAEC, Division of Military Applications, Washington 25, D. C.
L. Otowski, Area Manager, AEC Albuquerque Operations Office, P. O. Box 5400 Albuquerque, New Mexico (2)
S. A. Upson, Director, Reactor Operations Division, AEC Albuquerque Operations Office, P. O. Box 5400, Albuquerque, New Mexico (3)
J. V. Levy, Area Manager, USAEC, Canoga Park Area Office, P. O. Box 591, Canoga Park, California, Attn: C. A. Malmstrom (2)
I. A. Peltier, Idaho Operations Office, Idaho Falls, Idaho
C. A. Keller, USAEC, Oak Ridge Operations Office, P. O. Box E, Oak Ridge, Tennessee
T. R. Wilson, Phillips Petroleum Company, Idaho Falls, Idaho
Col. I. J. Russell, AFWL (WLRB)
Col. R. A. Gilbert, AFWL (WLG)
Lt. Col. J. W. Talley, AFWL (WLDN)
Col. D. C. Jameson, AFINS-R, KAFB
R. L. Detterman, Atomics International, P. O. Box 309, Canoga Park, California (4)
NASA Langley Research Center, Langley Station, Hampton, Virginia, Attn: E. D. Schult (5)
T. B. Kerr, RNS, NASA Headquarters, Washington 25, D. C.
R. D. Ginter, NASA Headquarters, Washington 25, D. C.
W. A. Guild, NASA Headquarters, Washington 25, D. C.
J. Whitfield, Assistant Branch Manager Hypervelocity Branch, VonKarman Gas Dynamics Facility, Arnold Engineering Division Center, Arnold AFB, Tennessee
S. P. Schwartz, 1
R. W. Henderson, 100
E. H. Draper, 1000
C. F. Bild, 1100, Attn: E. R. Frye, 1112
W. M. O'Neill, 1120
M. M. Robertson, 1122 (2)
L. D. Hopkins, 1300, Attn: J. P. Cody, 1320
G. I. Hildebrandt, 1330
J. H. Findlay, 1400, Attn: J. P. Shoup, 1430
G. W. Rodgers, 1420
J. M. Wiesen, 1440
W. A. Gardner, 1500, Attn: D. M. Olson, 1530
S. A. Moore, 1540
L. D. Smith, 1600
R. A. Bice, 2000
L. J. Heilman, 2100
H. E. Lenander, 2500
R. B. Powell, 3000
K. A. Smith, 3100
D. S. Tarbox, 3200
S. P. Bliss, 3300
M. K. Linn, 3400
C. W. Campbell, 4000
R. J. Hansen, 4200
K. S. Spoon, 4300
T. T. Robertson, 4400, Attn: F. F. Eichert, 4410
R. E. Hopper, 4500
R. C. Fletcher, 5000
R. S. Claassen, 5100
J. W. Easley, 5300
T. B. Cook, 5400, Attn: B. F. Murphey, 5410

DISTRIBUTION (cont)
J. D. Shreve, 5414
F. C. Cheston, 6000
G. A. Fowler, 7000
L. E. Hollingsworth, 7200, Attn: H. E. Viney, 7210
W. T. Moffat, 7220, Attn: R. N. Browne, 7224
D. Beatson, 7223-5
G. E. Hansche, 7240
J. C. Eckhart, 7250
L. E. Lamkin, 7300
R. H. Schultz, 7320
J. W. Pearce, 7330
D. B. Shuster, 7400
V. E. Blake, 7410
H. E. Hansen, 7411 (6)
I. B. White, 7411
A. J. Clark, Jr., 7412 (6)
J. Jacobs, 7412-2
H. K. Togami, 7412-2
R. D. Klett, 7412-3
H. R. Spahr, 7412-3
A. E. Bentz, 7413 (6)
C. E. Erickson, 7413-1
A. Y. Pope, 7420 (3)
M. L. Kramm, 7430
W. C. Scrivner, 7600, Attn: J. L. Tischhauser, 7620
B. S. Biggs, 8000
L. Gutierrez, 8100
D. R. Cotter, 9100
E. A. Paxton, 8232-1
B. R. Allen, 3421
M. G. Randle, 3428-1, Bldg. 836
M. G. Randle, 3428-1, Bldg. 880
Jim Fife, 3412 (2)
L. D. Patterson, 3411-1 (2)
R. C. Smelich, 3427-3 (50)